(2)

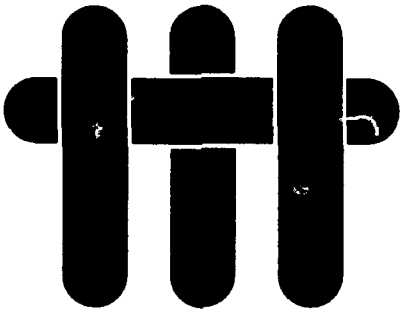

FINAL REPORT to ONR

Agency Award Number N00014-91-J-4024

Sensor and Actuator Materials For High Performance Composites

Principal Investigators:

A. G. Evans and D. R. Clarke
Materials Department
University of California
Santa Barbara, CA 91306

UCSB

Narrative:

This award has been used to purchase specialized equipment to enable us to initiate a new research activity at UC Santa Barbara on Sensors and Actuators for High Performance Composites. The overall, long-term goal of the research that we have begun using the equipment for is to develop improved acuator and sensor materials for use in integrated Smart Materials and Structures.

The major items of equipment obtained included an Optical Microprobe for the measurement of the fluorescence shifts that occur when ceramics are stressed, a mechanical testing apparatus that enables us to make simultaneous measurements of stress, strain and polarization, and the electrical property characterization equipment necessary to measure the dielectric and polarization properties of candidate actuator materials.

In the first year since the equipment was installed we have pursued two objectives: a) the in-situ measurement of stresses inside sapphire reinforcing fibers in high performance composites, and b) measurement of the constitutive stress-electric field-strain behavior of multilayer actuator materials. The research is on-going but has already facilitated the research described in the publications listed in the Appendix.

Relation to Other ONR/DARPA Programs:

The work on the sapphire stress sensors has been supported by ONR through the grant "Experimental Studies of Stress Measurement by Optical Fluorescence" under award number N00014-J-1875.

APPENDIX

List of Publications Facilitated By Award N00014-91-J-4024

1. *Stress Measurement In Single and Polycrystalline Ceramics using Their Optical Fluorescence*, Q. Ma and D. R. Clarke, *Journal of the American Ceramic Society*, submitted.

2. *Direct Measurement of Stresses in Sapphire Fibers In Composites*, Q. Ma and D. R. Clarke, *Acta Metallurgica et Materialia*, to be submitted.

3. *Optical Fluorescence From Chromium Solutes In Sapphire: A Probe of the Image Stress*, Q. Ma and D. R. Clarke, *Acta Metallurgica et Materialia*, to be submitted.

4. *Acoustic Emission During Polarization Switching in Ferroelectric Ceramics*, W. Pan and H. C. Cao, *Ferroelectrics*, Vol. 129, pp. 119-126 (1992).

5. *The Structure and Properties of a Ferroelectric Electrode Interface*, H. C. Cao, M. De Graef and A. G. Evans, submitted to *Journal of the American Ceramic Society*.

6. *Electric Field-Induced Fatigue Crack Extension in Ferroelectric Ceramics*, H. C. Cao and A. G. Evans, to be completed.

7. *Singular Behavior Near a Crack Tip in an Elastic Electrostrictive Material*, by H. C. Cao and R. M. McMeeking, to be published.

8. *Non-Linear Constitutive Properties of Piezoelectric Ceramics*, H. C. Cao and A. G. Evans, submitted to the *Proceedings of the MRS Spring Meeting* .

9. *Non-Linear Deformation of Ferroelectric Ceramics*, H. C. Cao and A. G. Evans, submitted to *Journal of the American Ceramic Society*

MATERIALS

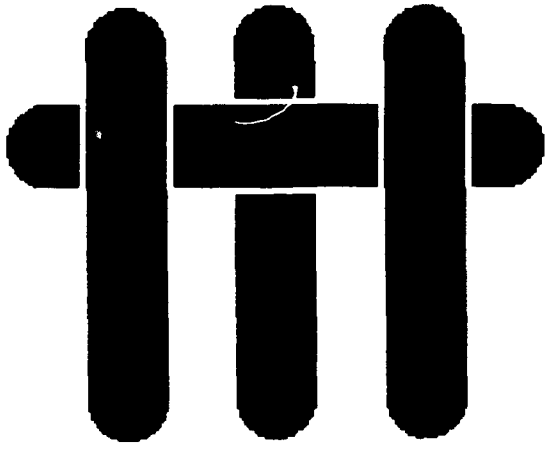

DIRECT MEASUREMENT OF STRESSES IN SAPPHIRE FIBERS IN COMPOSITES

Qing Ma and David R. Clarke
Materials Department
University of California
Santa Barbara, California 93106

Abstract

The residual stresses in sapphire fibers embedded in a number of ceramic and intermetallic matrices are measured non-destructively and in-situ using the stress-induced frequency shift in fluorescence from chromium dopants in the fibers. The stresses as a function of depth into the fibers from the free surface are measured and from the depth profile we have determined the interfacial shear stresses between the fibers and the matrices. The stress distributions provide a validation of the shear lag mechanics models of Hutchinson and Jensen, as well as a test of finite element computations.

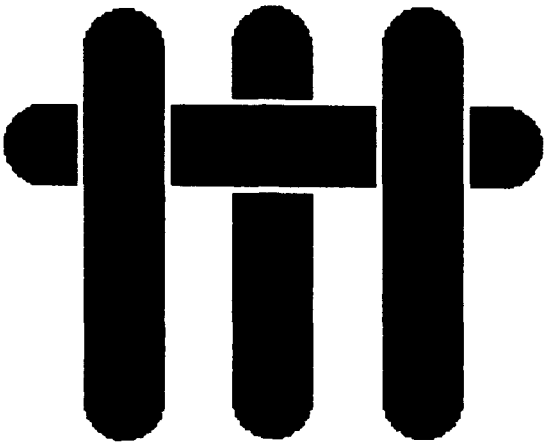

STRESS MEASUREMENT IN SINGLE AND POLYCRYSTALLINE CERAMICS USING THEIR OPTICAL FLUORESCENCE

Qing Ma and David R. Clarke
Materials Department
University of California
Santa Barbara, California 93106

A general methodology is developed for determining the state of stress and the numerical value of the stresses from observed shifts and broadening of optical fluorescence lines. The method is based on the piezo-spectroscopic properties of single crystals. We present general relationships between the measured fluorescence shifts and the stress state for a number of illustrative cases, pertinent to both polycrystalline and single crystal ceramics under stress. These include measuring the stresses applied to poycrystalline ceramics, the residual stress distribution due to crystallographically anisotropic thermal expansion, and the stresses applied to single crystals. Using the recently implemented technique of performing the fluorescence measurements in an optical microprobe, we also provide experimental tests of the relationships derived.

Submitted to the Journal of the American Ceramic Society

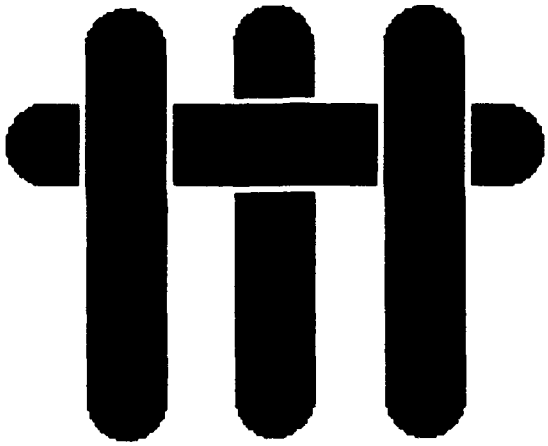

Optical Fluorescence From Chromium Ions In Sapphire: A Probe Of The Image Stress.

Qing Ma and David R. Clarke

Materials Department,
University of California,
Santa Barbara, CA 93106

Abstract.

The frequency of fluorescence from chromium substitutional solute in sapphire is shown to be a direct probe of the image stress. This provides a confirmation of the existence of the image stress, a component of the total internal stress due to inclusions, twins and precipitates, first introduced by Eshelby. The image stress contribution can be exploited in using chromium fluorescence as a sensor of stresses in solids.

To be submitted to Acta Metallurgica et Materialia

MATERIALS

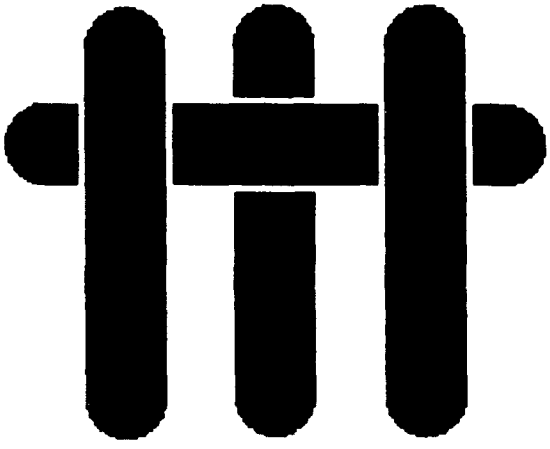

STRESS MEASUREMENT IN SINGLE AND POLYCRYSTALLINE CERAMICS USING THEIR OPTICAL FLUORESCENCE

Qing Ma and David R. Clarke

Materials Department
University of California
Santa Barbara, California 93106

Abstract

A general methodology is developed for determining the state of stress and the numerical value of the stresses from observed shifts and broadening of optical fluorescence lines. The method is based on the piezo-spectroscopic properties of single crystals. We present general relationships between the measured fluorescence shifts and the stress state for a number of illustrative cases, pertinent to both polycrystalline and single crystal ceramics under stress. These include measuring the stresses applied to poycrystalline ceramics, the residual stress distribution due to crystallographically anisotropic thermal expansion, and the stresses applied to single crystals. Using the recently implemented technique of performing the fluorescence measurements in an optical microprobe, we also provide experimental tests of the relationships derived.

1 INTRODUCTION

Despite the importance of measuring the stress state in a material or structure there are few quantitative methods available. Those that have been developed and widely used, such as photoelastic methods and X-ray methods, whilst accurate are generally limited to examining flat surfaces and ones where the area interrogated is not obscured or shadowed by features such as steps. In addition they are difficult to apply to the measurement of stresses from small areas, a few microns across, and are not generally microscope-based thus precluding making measurements from features identifiable during examination of a microstructure.

For these, and related, reasons a number of optical techniques based on piezo-spectroscopic phenomena have been proposed. One gaining increased support, especially in VLSI silicon based technologies, is that of Raman spectroscopy using an optical microprobe [1]. The Raman lines of silicon at 520 cm^{-1} are shifted by the application of a stress, and so regions on a silicon wafer around fine metal lines and dielectric features can be probed, with approximately a micron resolution, and their stress evaluated. Another piezo-spectroscopic technique proposed in the late 1970's for the measurement of stress, is that of fluorescence spectroscopy [2]. The suggestion, made by Grabner, followed the demonstration at the Bureau of Standards that the pressure in high-pressure experimental cells could be calibrated by the shift of the chromium fluorescence lines from fine particles of ruby embedded in the high-pressure cell [3]. In turn, this work built on the luminescence studies of chromium doped sapphire by Schawlow [4] and, independently by Sugano and Tanabe [5], as part of their investigation of possible laser materials. They found that the luminescence lines in chromium-doped sapphire were shifted by an applied stress. We have recently demonstrated that by implementing the fluorescence spectroscopy using an optical microprobe it is pos-

sible to measure stresses in chromium-doped alumina from regions identified in the optical microscope and with a spatial resolution of a few microns [6].

In this paper we present a method of analyzing an observed frequency shift in terms of the piezo-spectroscopic coefficients and the stress (and hence strain) on the crystal structure containing a fluorescing atom. This provides a correction to the equation derived by Grabner for the case of chromium fluorescence in alumina [2]. We then extend the analysis to the measurement of stresses in inhomogeneously stressed materials, presenting a number of illustrative examples of the application of the fluorescence technique to the measurement of commonly occurring types of stresses in ceramics. These provide the basis for future work in the widespread application of the technique to measure stresses in ceramic composites and at ceramic-interfaces.

2 PRINCIPLES OF PIEZO-SPECTROSCOPIC ANALYSIS

The basis of all piezo-spectroscopic methods for the measurement of stress in crystalline materials is that an applied stress strains the lattice and alters the energy of transitions between electronic or vibrational states. In this way, the energy of any radiative transitions, such as those that give rise to luminescence, also varies and produces systematic shifts in the frequency of luminescence lines such as fluorescence lines. In common with other spectroscopies, the sharpness of the fluorescence line depends on temperature and variations in the site position of the fluorescing atomic species. When the fluorescing ion is located on a lattice site in a tightly bound, high elastic modulus material, as is the case for chromium substitution for an aluminum ion in the sapphire lattice, the lines can be exceptionally sharp, broadened only by phonon scattering. Interstitial dopants, where there is greater variability in the dopant site or in a random network structure, such as chromium in glasses, give rise

to much broader, and usually weaker, luminescence lines.

The principle of relating an observed line shift in a fluorescence or absorption spectrum to the state of stress have been described previously by Grabner [2] in reference to the measurement of stresses in sintered, polycrystalline alumina containing a trace of Cr^{3+}. The more general case is presented here.

When a crystal is subject to a homogeneous stress σ^*_{ij} (in crystallographic frame of reference), the change in frequency, $\Delta\nu$, of a luminescence line is given by the tensorial relationship:

$$\Delta\nu = \Pi_{ij}\,\sigma^*_{ij} \tag{1}$$

where Π_{ij}'s are the piezo-spectroscopic coefficients relating frequency to stress. They form symmetrical second rank tensors, which have symmetry properties governed by the point symmetry group of the fluorescing ion. They may also have different numerical values for different fluorescence line energies. No appreciable stress induced broadening has been reported at room temperature so the lines merely shift with stress without changing shape. (Stress induced splitting is detectable at liquid helium temperatures but is unobservable at room temperature being masked by thermal broadening). In general, any applied stress will not be imposed on the crystal along its crystallographic axes, as represented in equation 1, but rather in some other coordinate frame. The stress on the crystal structure will then be given by the applied stress components resolved onto the crystallographic axes, i.e. through an orthogonal coordinate transformation:

$$\sigma^*_{ij} = a_{ik}a_{jl}\,\sigma_{kl} \tag{2}$$

where a_{ij} is the transformation matrix relating the frame of reference in which the applied

stresses are defined with respect to the crystallographic axes of the lattice.

Thus, the frequency shift of a fluorescence line in a luminescing crystal oriented at an arbitrary angle to a superimposed stress and strain field is given by the following tensorial relation:

$$\Delta\nu = \Pi_{ij}\, a_{ik} a_{jl}\, \sigma_{kl} = \Pi_{ij}\, c_{ijkl}\, a_{km} a_{ln}\, \epsilon_{mn} \tag{3}$$

One of the major limitations of piezo-spectroscopy is evident from this equation. Unless the fluorescing species emits at several different frequencies, so that a set of simultaneous equations (one for each transition) can be generated, there may be an insufficient number of distinct transitions to solve for each of the maximum of six independent stress components needed to completely describe the stress state. In some materials, the point symmetry of the fluorescing ion may also preclude the determination of all the independent stress components. This will be seen to be the case for both MgO and Al_2O_3.

Of the many fluorescence spectra reported, that of chromium fluorescence in sapphire has probably been the most thoroughly studied. The chromium ions replace aluminum ions substitutionally in the sapphire lattice and maintain their trivalent state, Cr^{3+}. Although the chromium ion is surrounded by an octahedron of oxygen ions, the octahedron is distorted along the body diagonal giving a point symmetry of $D_{3d}(\bar{3}m)$ for the chromium ion. The distortion also causes an asymmetry of the electrostatic crystal-field and results in a splitting of the ^2E energy levels by 0.004 eV, in turn giving rise to the two distinct radiative transition lines in ruby, R_1 and R_2 at 1.790 and 1.794 eV respectively. From the point symmetry of the chromium ion, it can be shown that the off-diagonal components of the piezo-spectroscopic tensor are zero and that the diagonal components are symmetrical about the *c*-axis, namely $\Pi_{11} = \Pi_{22} \neq \Pi_{33}$. For simplicity, we will use $\Pi_{11} = \Pi_{22} = \Pi_a$ and $\Pi_{33} = \Pi_c$ for R_1 and R_2

lines. Substituting these components into equation 3, the frequency shift for a chromium fluorescence line can be expressed in terms of the applied stress components as:

$$\begin{aligned}\Delta\nu &= \Pi_a(\sigma_{11}+\sigma_{11}+\sigma_{11}) + (\Pi_c-\Pi_a)(a_{31}^2\,\sigma_{11}+a_{32}^2\,\sigma_{22}+a_{33}^2\,\sigma_{33}) \\ &+ 2(\Pi_c-\Pi_a)(a_{31}a_{32}\,\sigma_{12}+a_{32}a_{33}\,\sigma_{23}+a_{31}a_{33}\,\sigma_{31}) \qquad (4)\end{aligned}$$

This differs from the expression derived by Grabner (equation 4 reference 2) in having an additional term (the second) proportional to the trace of the applied stress tensor. For the particular case in which the applied stress is purely hydrostatic, this equation simplifies to that used in the high-pressure physics and materials literature, namely

$$\Delta\nu = -(2\Pi_a+\Pi_c)P \qquad (5)$$

where P is the pressure. Also, unlike Grabner's equation, equation 4 reduces to equation 1 when the stress field is applied along the crystal axes. The point symmetry of the chromium ion simplifies equation 3 but nevertheless the stress components cannot be determined completely from the shifts of the R_1 and R_2 lines unless the misorientation between the applied stress and the crystal axes is known from some other, independent measurement.

The chromium fluorescence spectrum from magnesia has also been investigated in some detail [7], and can similarly be used to monitor strains. As in sapphire, the chromium ion occupies substitutionally a lattice site in magnesia and is surrounded by an octahedron of oxygen ions. However, the oxygen octahedra remain undistorted so the chromium point symmetry is raised to m3m. As a consequence, the ^2E level is not split and only one line, at 14319 cm^{-1}, occurs. The m3m point symmetry imposes the additional requirement that the diagonal piezo-spectroscopic coefficients are all equal ($\Pi_{11} = \Pi_{22} = \Pi_{33}$). Thus, for

chromium luminescence in magnesium oxide, the line shift is sensitive only to the trace of the stress tensor:

$$\Delta\nu = \Pi_{11}(\sigma_{11} + \sigma_{11} + \sigma_{11}) \tag{6}$$

This insensitivity to the deviatoric stresses, nevertheless, has the advantage that the shift is independent of the orientation of the crystal structure with respect to the applied stress.

Rare earth ions, such as Sm^{3+} and Nd^{3+}, can substitute for the yttrium ion in the yttrium aluminum oxide, garnet structure and give rise to sharp characteristic fluorescence spectra. The three possible substitutional sites, although equivalent under the cubic point group symmetry of YAG, have orthorhombic site symmetry. Since ions at all three sites will fluoresce when the crystal is excited, applying a stress should in general break the degeneracy associated with the equivalence of the three sites and cause line splitting. However, in practice, the stress splitting is masked by thermal broadening at room temperature, and so the fluorescence appears to come from a crystal having cubic symmetry [8] with equal piezo-spectroscopic coefficients.

3 INHOMOGENEOUS STRAIN FIELDS

The above analysis pertains to the case of a single crystal subject to a homogeneous strain field over the volume of material exposed to the excitation probe. When the probed volume contains more than one crystallite or the strains vary within it, the observed spectral shifts are more complex. They can, however, be understood from simple superposition arguments provided inelastic scattering of the luminescence is not appreciable and the strains do not vary over distances comparable to the lattice spacing. (For the case of the N- and F- fluorescence lines, the latter requirement is a little more stringent. In that case, the strains should not

vary over distances associated with the separation of the ions making up the chromium pairs from which these characteristic lines originate).

Subject to these restrictions, strain inhomogeneities and the presence of multiple grains within the probed volume can cause both broadening and shifting of the luminescence lines as analyzed in Appendix A. In essence, each element of material over which there is a constant crystallographic orientation and homogeneous strain contributes a signal intensity proportional to its volume and concentration of fluorescence ions. The spectral shift is given by equation 3 with the appropriate values for each of the parameters. The superposition of the lines, shifted according to the strain of each volume element, causes the observed line to appear to be broadened and shifted. The broadening is not a measure of the deviatoric strains per-se as has been stated in the literature previously [2] but rather of the statistical variation in strains and crystallographic orientations in the region examined. As a result the broadening need not be symmetrical. Indeed the broadened lines can have a fine structure resulting from there being one or two regions whose contributions are disproportionately large. This is probably the cause of the fine structure in the spectra reported by Grabner [2].

Although analytical relationships between line shifts, broadening and inhomogeneous stress state in polycrystalline materials can not, in general, be presented, a number of simple cases of practical importance can be considered. Equations for a number of these are derived as described in the following sub-sections.

3.1 Polycrystalline Material

The first example for which an analytical function can be derived corresponds to a polycrystalline material, with no crystallographic texture or internal residual stress, under a

homogeneous applied stress and probed with an excitation beam large compared to the grain size. In this case, the contributions from the individual crystallites are averaged over many, randomly oriented grains.

The frequency shift in the fluorescence line is given by the first moment of the distribution of fluorescence frequencies. Using equations 3, and A6 and B3 in the appendices, this can be simply expressed as:

$$\overline{\Delta\nu} = \iiint P(\theta,\phi,\psi)\Delta\nu d\theta d\phi d\psi$$

which reduces to

$$\overline{\Delta\nu} = \frac{1}{3}(\Pi_{11}+\Pi_{22}+\Pi_{33})(\sigma_{11}+\sigma_{11}+\sigma_{11}) \tag{7}$$

This equation shows that, irrespective of the crystal structure, the frequency shift of the fluorescence from a large number of grains in a polycrystalline material is dependent only on the trace of the applied stress tensor.

The polycrystalline ensemble of grains also leads to an intrinsic, stress dependent broadening of the fluorescence line. The peak broadening is given by the second moment of the distribution, which using equation A8, may be written as:

$$\begin{aligned} <\Delta\nu^2> &= \frac{4}{15}\left[(\Pi_{22}-\Pi_{11})^2+(\Pi_{33}-\Pi_{11})^2-((\Pi_{22}-\Pi_{11})(\Pi_{33}-\Pi_{11})\right] \\ &\times \left[\frac{1}{3}(\sigma_{11}^2+\sigma_{22}^2+\sigma_{33}^2-\sigma_{11}\sigma_{22}-\sigma_{22}\sigma_{33}-\sigma_{33}\sigma_{11})+(\sigma_{12}^2+\sigma_{23}^2+\sigma_{31}^2)\right] \end{aligned} \tag{8}$$

Such broadening is due to the differences in the diagonal piezo-spectroscopic coefficients. Consequently, for materials with fluorescing ions having cubic point symmetry, such as Cr^{3+} in MgO, (for which the piezo-spectroscopic coefficients are equal) the application of an external stress does not cause any broadening.

3.2 Inhomogeneously Stressed Single Crystal

The second case corresponds to a single crystal containing inhomogeneously stressed regions. A special case, but nevertheless an important one, is one in which the stress varies with depth below the surface, such as might pertain to surface stressing produced by ion exchange or when the sample is loaded in bending. For purposes of generality, we may assume that the concentration of the fluorescing ion, c, is a function of depth z. We can, in principle, also incorporate various instrumental functions, such as the collection efficiency as a function of depth of the apparatus used to measure the fluorescence spectrum, into a function $g(z)$. The function $g(z)$ allows the fluorescence signal to be normalized:

$$\int c(z)g(z)dz = 1$$

and a weighting function introduced:

$$W(\Delta\nu)d\nu = c(z)g(z)dz \tag{9}$$

Again, for purposes of generality, the frequency shift can be written so as to include a shift dependent on the concentration, c, of the fluorescing species:

$$\Delta\nu = \Pi_{ij}\, a_{ik}a_{jl}\, \sigma_{kl} + \beta(c - c_0) \tag{10}$$

where c_0 is the concentration of the reference sample which the shift is compared.

The average peak shift, expressed by the first moment of the fluorescence peak then becomes

$$\overline{\Delta\nu} = \int [\Pi_{ij}\, a_{ik}a_{jl}\, \sigma_{kl} + \beta(c - c_0)]\, c(z)g(z)dz \tag{11}$$

The broadening is a mixture of the inhomogeneous broadening due to the depth dependence of shift and the intrinsic homogeneous broadening due to change of concentration. For simplicity, we give the result for the case of constant concentration c_0:

$$< \Delta\nu^2 >= \int (\Pi_{ij}\, a_{ik} a_{jl}\, \sigma_{kl})^2 c(z) g(z) dz - \overline{\Delta\nu}^2 \tag{12}$$

in which $\overline{\Delta\nu}^2$ is also evaluated at $c = c_0$.

3.3 Anisotropic Thermal Expansion Residual Stresses

The third case considered here is of a polycrystalline material for which the thermal expansion coefficient is crystallographically anisotropic. As a result of such thermal expansion anisotropy, residual stresses can be created on cooling from the fabrication temperature, with the magnitude of the stresses being dependent on the geometrical constraint imposed by the neighboring grains, the elastic properties of the grains and the extent to which accommodation mechanisms, such as creep and plastic deformation, which can relax the stresses. In the special cases in which the grains do not constrain one another on cooling or the accommodation mechanisms are complete, no internal stresses develop and neither a line shift nor broadening would arise. However, there is in general some mutual constraint imposed by the contracting grains that causes stresses to develop within the material. The average stress over the material must be zero but variations in stress from one grain to another can cause both a broadening of the line and a line shift. Although the specific values will vary from place to place in the sample, since the stresses will also vary from grain to grain, it is possible to calculate the average values as will now be shown. Two assumptions are made. First, that the probed volume encompasses a sufficiently large number of grains that an ensemble average can be considered, and secondly that the distribution of stresses can be described

by an appropriate distribution function.

Consider a material, such as alumina, which has a thermal expansion coefficient that is larger along its c-axis than along its a-axis, and has an axis of rotational symmetry along the c-axis. On cooling from its fabrication temperature, tensile stresses will, on average, develop along the c-axis of the grains and compressional stresses will develop in the basal plane. Therefore,

$$\overline{\sigma_a} < 0 \,, \qquad \overline{\sigma_c} > 0 \tag{13}$$

Now, consider a grain intersected by an arbitrarily placed plane that divides the polycrystalline sample into two. The orientation of the grain can be specified by the angular coordinates (θ, ϕ) of its c-axis (figure 1). Provided the dividing plane intersects a large number of grains, with all possible stress states, we need only consider the average stresses along the a- and c- axes. Therefore the stress in the basal plane is equi-biaxial, and rotation of the grain around the c-axis does not alter its stress state. The force acting per unit area in any grain perpendicular to the dividing plane can be expressed by resolving the stresses in that grain:

$$f = \overline{\sigma_a} \sin\theta + \overline{\sigma_c} \cos\theta \tag{14}$$

Since, across the dividing plane, the orientation of the grains is random, the average force can be written as:

$$\overline{f} = \frac{1}{2\pi} \int_0^{2\pi} d\phi \int_0^{\pi/2} f \sin\theta d\theta \tag{15}$$

Since the force must on average be zero, $\overline{f} = 0$, the mean stresses in the c- and a- crystallographic directions are related by:

$$\overline{\sigma_c} = -\frac{\pi}{2} \overline{\sigma_a} \tag{16}$$

Recognize that the average stresses described above are equivalent to volume average, the mean shift of the fluorescence line is therefore,

$$\overline{\Delta\nu} = \left(\Pi_c - \frac{4}{\pi}\Pi_a\right)\overline{\sigma_c} \tag{17}$$

The peak broadening can be calculated using equation A8 on the assumption that the distribution in stresses in the a- and c- crystallographic directions are independent of one another:

$$P(\sigma_a, \sigma_c) = p(\sigma_a)p(\sigma_c) \tag{18}$$

and are also Gaussian with the same width, σ_w

$$p(\sigma_a) = \frac{1}{\sqrt{2\pi}\sigma_w}\exp\left[-\frac{(\sigma_a - \overline{\sigma_a})^2}{2\sigma_w^2}\right] \tag{19}$$

The assumption of independence of the stress distributions in the different directions enables the weighting function in equation A8 to be written as:

$$W(\Delta\nu)d\nu = P(\sigma_a, \sigma_c)d\sigma_a d\sigma_c = p(\sigma_a)p(\sigma_c)d\sigma_a d\sigma_c$$

So, the peak broadening becomes:

$$< \Delta\nu^2 >= 4\Pi_a^2\,\sigma_w^2 + \Pi_c^2\,\sigma_w^2 + 4\Pi_a\Pi_c\,\overline{\sigma_a}\;\overline{\sigma_c} \tag{20}$$

Thus, using measurements of the mean peak shift, which from equation 17 gives the mean stresses along the a- and c- axes, and a measurement of the peak width, the stress distribution within the material can be determined.

These equations shows that the crystallographic anisotropy in thermal expansion leads to both an average shift and broadening of the fluorescence line. They are related to the average values of the stresses and the stress distribution. The spatially varying stresses can be significantly larger than the average, especially those acting over smaller distances than the grain size, related to the presence of the grain edges and corners. These are primarily responsible, for instance, for micro-crack extension. Although detailed information of such stresses does not appear to be amenable to the analysis of the shape of the fluorescence lines, their magnitude and the occurring frequency are reflected by the stress distribution.

3.4 Matrix Stresses Due to Presence of Fibrous Inclusions

The final case considered is that of a polycrystalline matrix surrounding an embedded fiber. The radial and tangential stresses in a matrix around a misfitting fiber of radius, r_0, are given by standard elastic solutions, varying with the inverse square of distance, r, from the fiber axis. For observations made in a cross-section perpendicular to the fiber axis (axis 3), the matrix stresses may be written as

$$\sigma_{11} = -\sigma_{22} = \frac{\sigma_0 r_0^2}{r^2} \; ; \quad \sigma_{33} = 0 \tag{21}$$

Thus, from equation 3, the frequency shifts are given by

$$\Delta\nu = (\Pi_{22} - \Pi_{11})(a_{21}^2 - a_{22}^2)\,\sigma_{11} + (\Pi_{33} - \Pi_{11})(a_{31}^2 - a_{32}^2)\,\sigma_{22} \tag{22}$$

which would be detectable with a probe having high optical resolution ($\ll r_0$). If the probe is large, such that either many grains in a polycrystalline matrix or regions within a circle encompassing the fiber in a single crystal matrix are excited simultaneously, then the average

peak shift is $\overline{\Delta\nu} = 0$. The peak broadening, for such a large probe, would also average out for single crystal and polycrystalline material to a value of

$$< \Delta\nu^2 >= \frac{4}{45}\,\overline{\sigma_{11}^2}\,[(\Pi_{22} - \Pi_{11})^2 + (\Pi_{33} - \Pi_{11})^2 - (\Pi_{22} - \Pi_{11})(\Pi_{33} - \Pi_{11})] \qquad (23)$$

where $\overline{\sigma_{11}^2}$ is averaged over the volume probed.

4 OBSERVATIONAL TESTS

In this section a series of measurements are described that provide experimental tests and validations of the equations presented in the preceding sections. The tests were made with aluminum oxide because of its ready availability. The experiments were performed using an unmodified optical microprobe[1] to both excite the luminescence and to collect and analyze the resulting fluorescence spectrum using an attached spectrometer. (The optics of the Microprobe have been described in an earlier publication [9]). A number of laser frequencies have been used to excite the luminescence but the results reported here were all obtained using an argon ion laser with a wavelength of 514 nm. The experimental procedure was to select a region of interest on the sample with the attached optical microscope, focus the laser beam to a spot on the selected feature and analyze the fluorescence produced. The intensity of the R_1 and R_2 fluorescence lines were typically scanned by integrating over 0.5 second intervals at a spacing of 0.2 wavenumbers, with the intensities being recorded under computer control. The collected data was subsequently analyzed with curve fitting algorithms, included in the LabCalc software package[2], to identify the position of the fluorescence peak. By using objective lenses of 50× and 100× magnifying powers minimum spot sizes of $\sim 5\mu$m and

[1] Instruments SA, Raman Microprobe Model T64000.
[2] Galictic Industries Corp.

$\sim 1 - 2\mu$m can be produced. Larger probe sizes were formed by partial defocusing. Also, by appropriate choice of the collection aperture size, the attainable axial resolution could be varied by the collection optics from $\sim 10\mu$m to $\sim 200\mu$m [10].

All the measurements were made with the sample at room temperature. Although a change in temperature is known to cause a line shift of ~ 0.14 cm^{-1}/°C [11] (to smaller wavenumbers with increasing temperature), no line shift was noted when the spot size was systematically decreased (thereby increasing the power density incident on the sample) indicating that no significant heating of the probed volume occurred. This lack of sensitivity to spot size was attributed to both the low absorption of ruby at the excitation frequencies and the relatively low illumination intensities used. Variations were, however, noted with variations in room temperature and so temperature corrections were made to the peak shifts.

4.1 Polycrystalline Sample Under Stress

In order to test the validity of equations 7 and 8 concerning the stress dependence of the peak shift and broadening in a polycrystalline material, polished bars of polycrystalline alumina (Coors AD96) were subject to an applied stress and the fluorescence spectra recorded. The stress was applied using a four-point bend stage specially designed to fit under the optical microscope of the microprobe. The polycrystalline alumina contained sufficient levels of chromium impurity to provide sufficiently strong fluorescence peaks to be analyzed. In order to average over many grains, a probe diameter of $\sim 50\mu$m was used for the fluorescence measurements. The grain size of the alumina was 2-20μm.

Since alumina is thermally anisotropic, the analysis in section III.1 has to be extended to separate the effect of thermal residual stress existing in the sample from any applied stress.

The shift from a small volume element dv (much smaller than the grain size) is

$$\Delta\nu = 2\Pi_a(\sigma_a^A + \sigma_a^T) + \Pi_c(\sigma_c^A + \sigma_c^T) \tag{24}$$

where the superscripts A and T denote applied and thermal stresses respectively. Since the above equation is linear, the effects of two types of stress can be separated:

$$\Delta\nu = \Delta\nu^A + \Delta\nu^T \tag{25}$$

Therefore, the mean shift:

$$\overline{\Delta\nu} = \frac{1}{V}\int(\Delta\nu^A + \Delta\nu^T)dv = \overline{\Delta\nu^A} + \overline{\Delta\nu^T} \tag{26}$$

Since the shift generated by thermal stress (see section 4.3) can be measured independently, $\overline{\Delta\nu^A}$ can be obtained.

The broadening is calculated by using equation A8:

$$\begin{aligned} <\Delta\nu^2> &= \frac{1}{V}\int(\Delta\nu^A + \Delta\nu^T)^2 dv - \overline{\Delta\nu}^2 \\ &= <(\Delta\nu^A)^2> + <(\Delta\nu^T)^2> + 2\left[\overline{\Delta\nu^A\Delta\nu^T} - \overline{\Delta\nu^A}\ \overline{\Delta\nu^T}\right] \end{aligned} \tag{27}$$

So the broadening can be separated provided that $\Delta\nu^A$ and $\Delta\nu^T$ are uncorrelated.

The measured peak shifts for the R_1 and R_2 fluorescence lines as a function of applied stress are shown in figure 2. The lines through the data, fitted by a least square analysis, shows that the stress dependence of the shift of the R_1 and R_2 fluorescence lines is 2.46 and 2.50 $cm^{-1}GPa^{-1}$ respectively. The fit coefficient R is 0.997 for both lines. For comparison to the theory in section III.1, equation 7 would predict that when a uniform stress is applied

to polycrystalline alumina, the peak shift would be given by:

$$\overline{\Delta\nu} = \frac{1}{3}(2\Pi_a + \Pi_c)\,\sigma^A$$

Using the hydrostatic pressure dependence of peak shifts for the R_1 and R_2 lines given by Munro et. al. [12], the sum of the spectroscopic coefficients, $2\Pi_a + \Pi_c$ have the values of 7.59 and 7.62 cm^{-1} GPa^{-1} for the R_1 and R_2 lines respectively. The peak shifts of the R_1 and R_2 lines would then be 2.53 and 2.54 $cm^{-1}GPa^{-1}$, close to that observed. The uniaxial compression experiment by Feher and Sturge [13] provided values for Π_a and Π_c independently with values of 2.7 and 2.15 cm^{-1} GPa^{-1} for both R_1 and R_2 lines. Using this data, the predicted stress dependence would be 2.52 $cm^{-1}GPa^{-1}$, again close to that observed. We can therefore conclude that our measured shifts fall within the uncertainty of the existing data on the piezo-spectroscopic coefficients.

The measured peak widths for the R_1 and R_2 fluorescence lines as functions of applied stress are shown in figure 3. For this material the systematic broadening due to the applied stress of both lines is small compared to the variability from one point on the sample to another.

4.2 Single Crystal With Surface Stress

A single crystal treated to produce a surface stress represents a special case of the inhomogeneously stressed single crystal considered in section III.2. To provide an experimental test of the effect of inhomogeneous stressing, a residual surface stress was produced in a single crystal of *c*-axis sapphire by in-diffusion of chromium and the fluorescence measured as a function of an applied stress. Since chromium oxide, Cr_2O_3, is isostructural with Al_2O_3 but has a larger lattice parameter, diffusion of chromium into the surface of Al_2O_3 is expected

to produce a compressive surface stress.

As chromium is both the fluorescing ion and the ion causing the surface stress, the analysis of section III.2 must include the stress created by the in-diffusion of chromium. In this case, the frequency shift is expected to be the sum of three distinct contributions, that due to any applied stress, that due to diffusion-induced stresses σ^D and that due to variations in fluorescing ion concentrations:

$$\Delta\nu = \Pi_{ij}\,\sigma_{ij}^A + \Pi_{ij}\,\sigma_{ij}^D + \beta(c - c_0) \tag{28}$$

The overall peak shift from the in-diffused layer can be written as:

$$\overline{\Delta\nu} = \int \Delta\nu\, c(z)g(z)dz = \overline{\Delta\nu^A} + \overline{\Delta\nu^D} + \overline{\Delta\nu^C} \tag{29}$$

Since the frequency shift in equation 28 is the sum of the individual components, the mean peak shifts of each component are also linearly independent as shown by equation 29. Thus, in an experiment in which an external stress is applied to a residually stressed surface, the mean frequency shift observed is predicted to be due to the applied stress only:

$$\overline{\Delta\nu^A} = \int \Delta\nu^A c(z)g(z)dz = \Pi_{ij}\,\overline{\sigma_{ij}^A} \tag{30}$$

For four-point bending, the applied stress is essentially constant over the depth of the in-diffused layer, and so the mean frequency shift will be linearly related to the applied stress.

For the experiment, in-diffusion of chromium was performed in a three step process. In the first step, a chromium acetate solution was spun-coated onto a c-axis oriented sapphire

disc. The coating was then pyrolyzed and oxidized by heating to 600°C in air. Then, finally, the disc was annealed at 1600°C to diffuse in the chromium and beams cut from the disc. To investigate the effect of applied stress the sapphire beam was loaded in four-point bending with c-axis perpendicular to the loading plane, placed under the microscope of the microprobe, and the resulting fluorescence recorded as a function of load. The observed peak shift for the R_1 and R_2 lines as a function of applied stress is shown in figure 4. For this data, the stress dependence is 2.42 and 2.61 $cm^{-1}GPa^{-1}$ for the R_1 and R_2 lines respectively, which compares favorably to the mean Π_a value of 2.7 $cm^{-1}GPa^{-1}$ given in [13]. The fit coefficient R equals 0.996 and 0.994, respectively.

4.3 Thermal Expansion Anisotropy Stresses

Residual stresses are known to be produced in polycrystalline alumina on cooling as a result of the crystallographic anisotropy in thermal expansion coefficients along the c- and a- axes. In order to measure the average residual stresses, the fluorescence from three different sintered, polycrystalline aluminas (Coors AD96, Coors AD 995 and UCSB1) and a polycrystalline alumina hipped at UCSB (UCSB2) was recorded using an excitation probe diameter of 50μm. The UCSB1 material is a high purity alumina sintered at 1800°C for 1 hr. in hydrogen. The probe size was much larger than the grain size of the ceramics, assuring that the fluorescence was being averaged over a large number of grains. The ceramic samples contained an adequate chromium impurity level for the R_1 and R_2 fluorescence peaks to be recorded with sufficient signal-to-background ratio that precise measurements could be made of the peak shape and peak shift. The peak shift and peak broadening were measured relative to those recorded from a polished single crystal of sapphire that also contained a trace level of chromium impurity. For comparison, the spectrum obtained from the AD995 sample is

plotted together with that of a single crystal sapphire in Figure 5. Several spectra were taken at different spots for each sample, the average peak shifts and broadening for the samples are listed in table I. Also shown in the table are the average stresses, $\overline{\sigma_a}$, $\overline{\sigma_c}$ and the breath of stress distribution σ_w calculated using equations 16, 17 and 20 above.

5 CLOSING REMARKS

The preceding analyses and experiments illustrate how the technique of fluorescence spectroscopy can be used to make measurements of commonly arising types of stresses in ceramics. This is possible, despite the fact that the fluorescence shift is a scalar quantity whereas the complete stress state is tensorial, because considerable simplification of the equations (equation 3) can be made in many practical situations. For instance, stresses can be applied at prescribed orientations to the crystallographic axes of single crystals. Also, the polycrystalline nature of many ceramics enables the effects of crystallographic orientation to be averaged out. For instance, as equation 7 demonstrates, the frequency shift from a stressed polycrystalline ceramic is independent of its crystal structure and is only dependent on the trace of the applied stress.

Two of the analytical results are of particular interest. One, is the finding that the fluorescence shift is dependent only on the applied stress and not on the residual stresses produced by either thermal expansion mismatch as in the case of polycrystalline Al_2O_3, or by ion in-diffusion as in the case of Cr^{3+} in-diffusion into sapphire single crystal . The later also suggests that a fluorescent dopant ion can be deliberately introduced into a structure or material to monitor the applied stress through changes in the fluorescence frequency. In fact, we have been utilizing this characteristics to make measurements of stresses in metal-ceramic

laminates [14].

The second notable result concerns the measurement of the residual stresses due to anisotropic thermal expansion. The analysis indicates that the mean stress in the *a*- and *c*- crystallographic directions in aluminum oxide can be obtained from the mean frequency shift, and that the distribution in internal stresses can also be determined. These results represent an advance on previous studies of anisotropic thermal expansion stresses in aluminum oxide [2,15]. As already mentioned, Grabner's work led to an incomplete expression for the relationship between the frequency shift and stress, and so the values he derived are probably unreliable. The work of Blendell and Coble [15], was primarily concerned with the diffusional relaxation of the anisotropic thermal expansion stresses. They assumed an average stress in the material and calculated its relaxation for different grain sizes and cooling rates. They did not relate this average stress to any of the crystallographic stresses nor did they describe how they determined this average stress from their fluorescence observations. However, the measurements in table I indicate that the mean stresses in the samples of polycrystalline alumina examined are similar in magnitude to those calculated.

ACKNOWLEDGEMENT

This work was supported by the U. S. Office of Naval Research under contract number N00014-91-J-1875.

APPENDIX

A Peak Shifts and Broadening due to Stresses

If the probed volume were strain free, the fluorescence peaks would be Lorentzian in shape and have a breadth dependent only on the finite temperature of the sample. The presence of stresses, however, causes the peaks to be shifted and dispersed as shown in the following.

Let the peak shape in the unstrained crystal be represented by the frequency function, $f(\nu)$, with the peak centroid given by:

$$\nu_0 = \int f(\nu)\nu d\nu \tag{A1}$$

and the area of the peak is normalized to be unity:

$$\int f(\nu)d\nu = 1 \tag{A2}$$

The dispersion of the peak, corresponding to the peak width, can be expressed by the second moment of the distribution:

$$< \nu^2 >_0 = \int f(\nu)(\nu - \nu_0)^2 d\nu \tag{A3}$$

The effect of any stress distribution can be related to measured peak shape by assuming that the probability of causing a frequency shift, $\Delta\nu$, can be expressed as a weighting function $W(\Delta\nu)$. The resulting peak is then given by the function:

$$F(\nu) = \int f(\nu - \Delta\nu)W(\Delta\nu)d\Delta\nu \tag{A4}$$

Since $\int W(\Delta\nu)d\Delta\nu = 1$, $\int F(\nu)d\nu = 1$ the area under the peak is conserved.

The centroid, or mean value, of the peak from the stressed volume is given by the first moment of the function representing the peak:

$$\nu_c = \int F(\nu)\nu d\nu \tag{A5}$$

The peak shift is then:

$$\begin{aligned} \overline{\Delta\nu} &= \nu_c - \nu_0 \\ &= \int \Delta\nu W(\Delta\nu)d\Delta\nu \end{aligned} \tag{A6}$$

As spectra $f(\nu)$ and $F(\nu)$ can be obtained from unstressed and stressed regions, the mean shift $\overline{\Delta\nu}$ can be determined and from that the stress deconvoluted.

The width of the stress broadened peak, $F(\nu)$, is:

$$< \nu^2 >_F = \int F(\nu)(\nu - \nu_c)^2 d\nu \tag{A7}$$

The broadening is then seen to be the difference between the measured widths of the peaks from the strain free regions and from the stressed regions:

$$\begin{aligned} < \nu^2 >_F - < \nu^2 >_0 &= \int \Delta\nu^2 W(\Delta\nu)d\Delta\nu - \overline{\Delta\nu}^2 \\ &= < \Delta\nu^2 > \end{aligned} \tag{A8}$$

Again, the measured broadening and the stress distribution is related by the weighting function.

B Polycrystalline Averages of Direction Cosines

Collected here for convenience are the polycrystalline averages of the direction cosines a_{ij} appearing in tensor transformation relations of the form:

$$\sigma'_{ij} = a_{im} a_{jn} \sigma_{mn} \tag{B1}$$

In terms of the usual Euler angles (θ, ϕ, ψ), the transformation matrix is

$$a_{ij} = \begin{pmatrix} \cos\phi\cos\psi - \sin\phi\cos\theta\sin\psi & -\cos\phi\sin\psi - \sin\phi\cos\theta\cos\psi & \sin\theta\sin\phi \\ \sin\phi\cos\psi + \cos\phi\cos\theta\sin\psi & -\sin\phi\sin\psi + \cos\phi\cos\theta\cos\psi & -\sin\theta\cos\phi \\ \sin\theta\sin\psi & \sin\theta\cos\psi & \cos\theta \end{pmatrix}$$

where

$$0 \le \phi \le 2\pi\ ,\quad 0 \le \theta \le \pi\ ,\quad 0 \le \psi \le 2\pi \tag{B2}$$

If, as in a polycrystalline material, the orientations of the grains are at random, the probability a grain director is oriented at (θ, ϕ, ψ) is given by

$$P(\theta, \phi, \psi) = \frac{1}{8\pi^2} \sin\theta d\theta d\phi d\psi \tag{B3}$$

By averaging over all possible angles, the following relations used to derive equation 7 and 8 are obtained:

$$\overline{a_{ij}^2} = \frac{1}{3}\ ; \qquad \overline{a_{ij} a_{ik}} = 0\ ,\quad j \neq k\ ;$$

$$\overline{a_{ij}^4} = \frac{1}{5} ; \qquad \overline{a_{ij}^2 a_{ik}^2} = \frac{1}{15} , \quad j \neq k ; \qquad \overline{a_{ij}^2 a_{lk}^2} = \frac{2}{15} , \quad i \neq l, \; j \neq k ;$$

$$\overline{a_{21}^2 a_{22} a_{23}} = \overline{a_{21} a_{22}^2 a_{23}} = \overline{a_{21} a_{22} a_{23}^2} = 0 ;$$

and

$$\overline{a_{21} a_{22} a_{31} a_{32}} = \overline{a_{21} a_{23} a_{31} a_{33}} = \overline{a_{22} a_{23} a_{32} a_{33}} = -\frac{1}{15} .$$

REFERENCES

1. P. Zorabedian and F. Adar, "Measurement of Local Stress in Laser Recrystallized Lateral Epitaxial Silicon Films Over Silicon Dioxide Using Raman Scattering", Applied Physics Letters, **43** [2] 177-179 (1983).

2. L. Grabner, "Spectroscopic Technique for the Measurement of Residual Stress in Sintered Al_2O_3", Journal of Applied Physics, **49** [2] 580-583 (1978).

3. R. A. Forman, G. J. Piermarini, J. D. Barrett and S. Block, "Pressure Measurement Made by the Utilization of Ruby Sharp Line Luminescence", Science, **176** 284-285 (1972).

4. A.L. Schawlow, "Fine Structure and Properties of Chromium Fluorescence in Aluminum and Magnesium Oxide", pp 50-64 in Advances in Quantum Electronics. Edited by J.R. Singer, Columbia University Press, New York, 1961.

5. S. Sugano and Y. Tanabe, "Absorption Spectra of Cr^{3+} in Al_2O_3", Journal of the Physical Society of Japan, **13** [8] 880-910 (1958).

6. S. E. Molis and D. R. Clarke, "Measurement of Stresses Using Fluorescence in an Optical Microprobe: Stresses Around Indentations in a Chromium-Doped Sapphire", Journal of the American Ceramic Society, **73** [11] 3189-3194 (1990).

7. A.L. Schawlow, A. H. Piksis and S. Sugano, "Strain Induced Effects on the Degenerate Spectral Line of Chromium in MgO Crystals", Physical Review, **122** [5] 1469-1477 (1961).

8. Jun He, Qing Ma and D.R. Clarke, to be published.

9. D. R. Clarke and F. Adar, "Measurement of the Crystallographically Transformed Zone Produced by Fracture in Ceramics Containing Tetragonal Zirconia", Journal of the American Ceramic Society, **65** [6] 284- 288 (1982).

10. F. Adar and D.R. Clarke, "Raman Microprobe Spectroscopy of Ceramics", pp 307-310 in Microbeam Analysis. Edited by K.F.J. Heinrich, San Francisco Press, San Francisco,

1982.

11. S.L. Wunder and P.E. Schoen, "Pressure Measurement at High Temperatures in the Diamond Anvil Cell", Journal of Applied Physics, **52** [6] 3772-3775 (1981).

12. R.G. Munro, G.J. Piermarini, S. Block and W.B. Holzapfel, "Model Line-Shape Analysis for the Ruby R Lines Used for Pressure Measurement", Journal of Applied Physics, **57** [2] 165-169 (1985).

13.E. Feher and M.D. Sturge, "Effect of Stress on the Trigonal Splittings of d^3 Ions in Sapphire (α-Al_2O_3)", Physical Review , **172** [2], 244-249 (1968).

14. Qing Ma and D. R. Clarke, to be published.

15. J. E. Blendell and R. L. Coble, "Measurement of Stress Due to Thermal Expansion Anisotropy in Al_2O_3", Journal of the American Ceramic Society, **65** (3) 174-178 (1982).

FIGURE CAPTIONS

1. Schematic diagram of a representative grain cut by an arbitrary dividing plane ($z = 0$) through a polycrystalline material, illustrating the coordinates and angles used in the text in describing the orientation of the grain.

2. Measured peak shifts of the R_1 (top) and R_2 (bottom) fluorescence lines from a polycrystalline alumina sample as a function of applied stress. The sample was loaded under four-point bending and spectra were recorded from different positions on both the tensile and compressional sides and over the stress range indicated. The solid line through the data points represents the line of best-fit. Its slope is, within experimental uncertainty, the same as that predicted using equation 7.

3. Measured peak broadening of the R_1 and R_2 fluorescence lines as a function of stress. The broadening was obtained from the same spectra as were used to make the measurements in figure 2.

4. Peak shift of the R_1 and R_2 fluorescence lines as a function of applied stress for a sapphire crystal containing a surface stressed layer. The solid line is the line of best fit to the data.The surface stress was produced by in-diffusion of chromium. Details are given in the text.

5. A comparison of the R_1 and R_2 fluorescence lines from sapphire and a polycrystalline alumina (Coors AD995). The broadening of the lines from the polycrystalline alumina is a result of the distribution of residual thermal expansion anisotropy stresses within the material. Both materials contain a trace of chromium impurity, sufficient to cause fluorescence.

TABLE I

SAMPLE	$\overline{\Delta\nu}$	$\overline{\sigma_a}$	$\overline{\sigma_c}$	$\sqrt{<\Delta\nu^2>}$	σ_w
	cm^{-1}	MPa	MPa	cm^{-1}	MPa
AD96	-0.21	-100	160	2.5	440
AD995	-0.15	-74	120	3.6	620
UCSB1	-0.15	-74	120	1.9	340
UCSB2	-0.23	-110	180	1.4	270

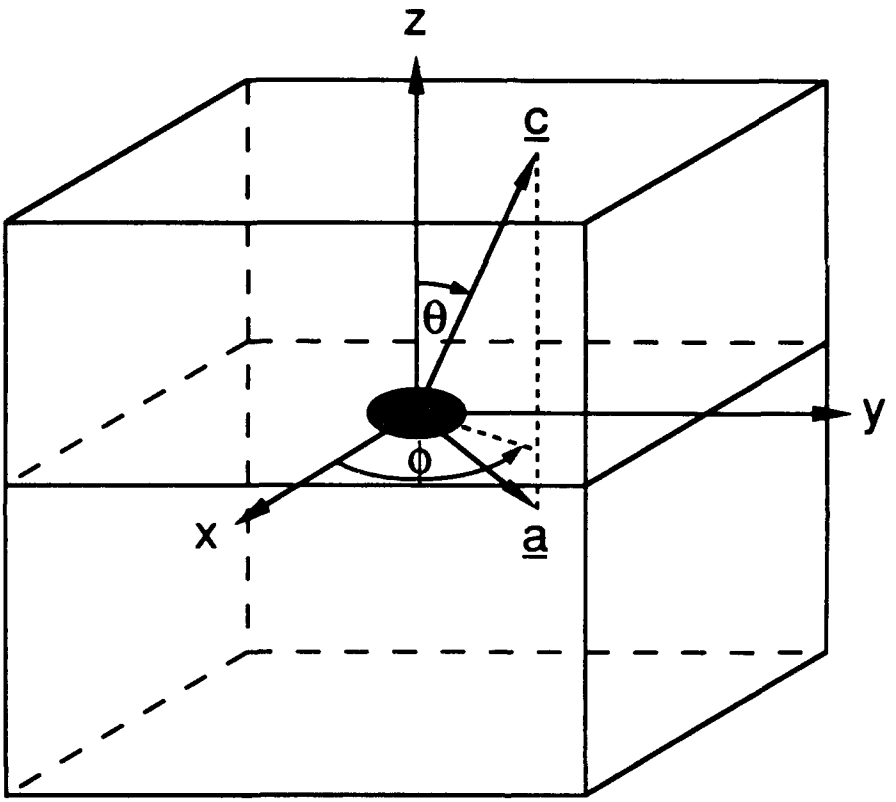

Fig. 1

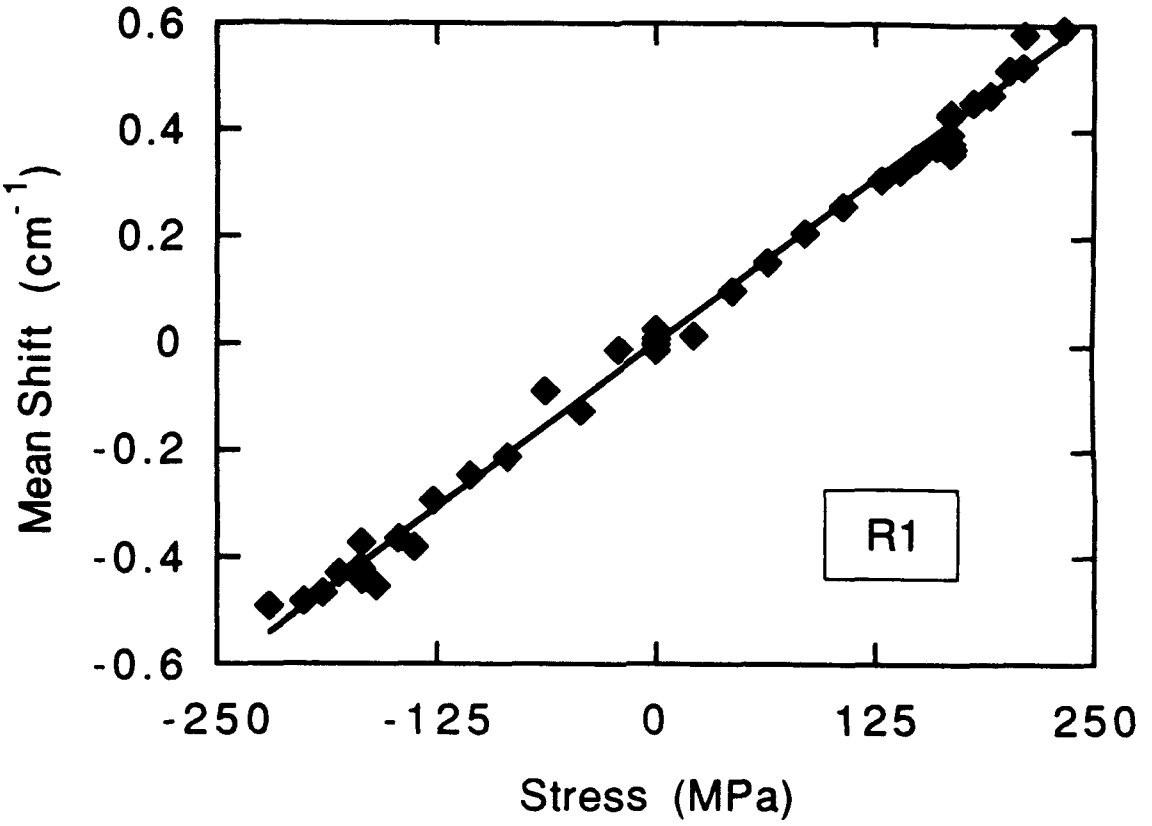
0.6
0.4
0.2
0
-0.2
-0.4
-0.6
Mean Shift (cm^{-1})
R1
-250
-125
0
125
250
Stress (MPa)

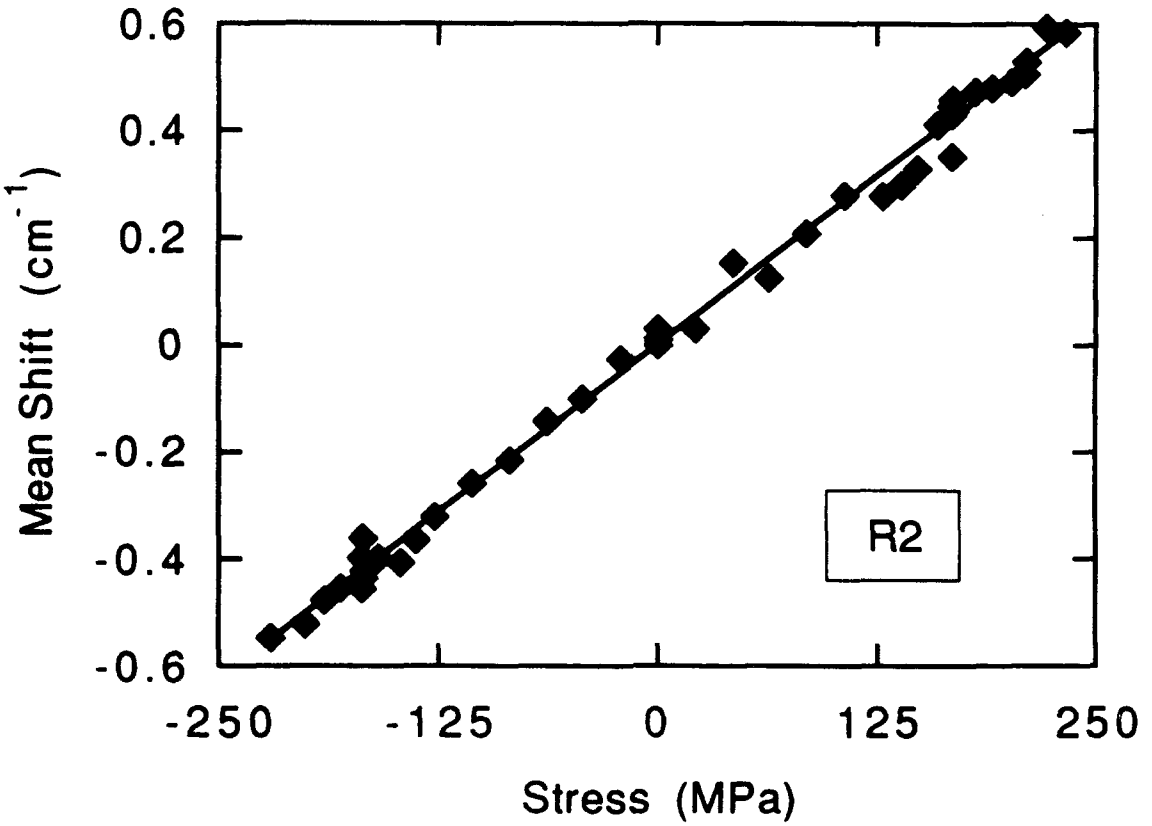
0.6
0.4
0.2
0
-0.2
-0.4
-0.6
Mean Shift (cm^{-1})
R2
-250
-125
0
125
250
Stress (MPa)

Fig 2

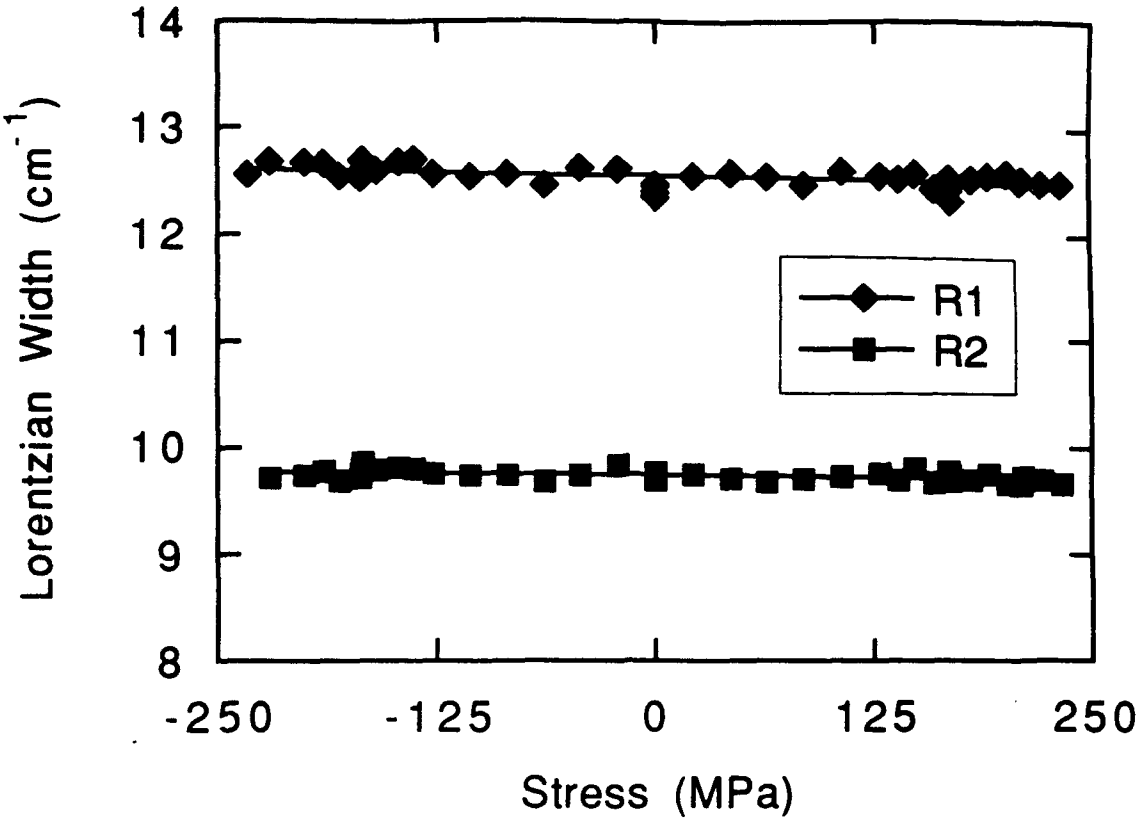
14
13
12
11
10
9
8
Lorentzian Width (cm^{-1})
-250
-125
0
125
250
Stress (MPa)
R1
R2

Fig. 3

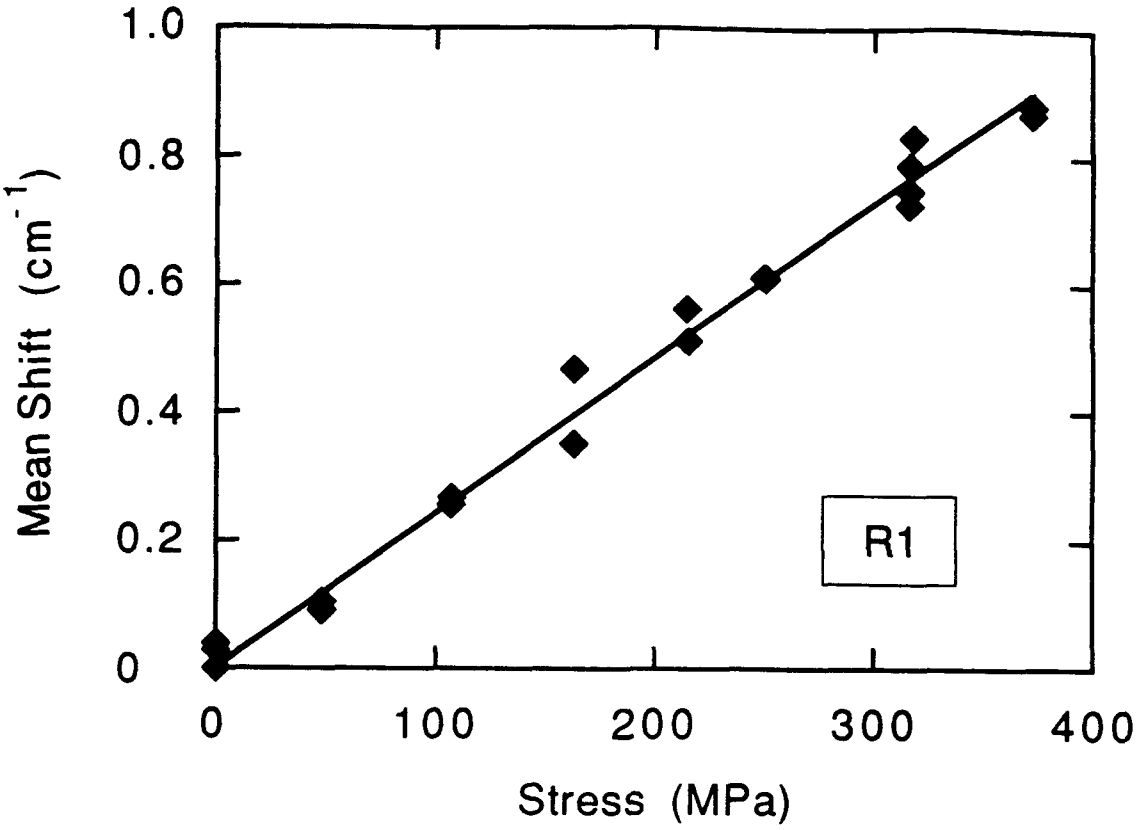
1.0
0.8
0.6
0.4
0.2
0
Mean Shift (cm^{-1})
R1
0
100
200
300
400
Stress (MPa)

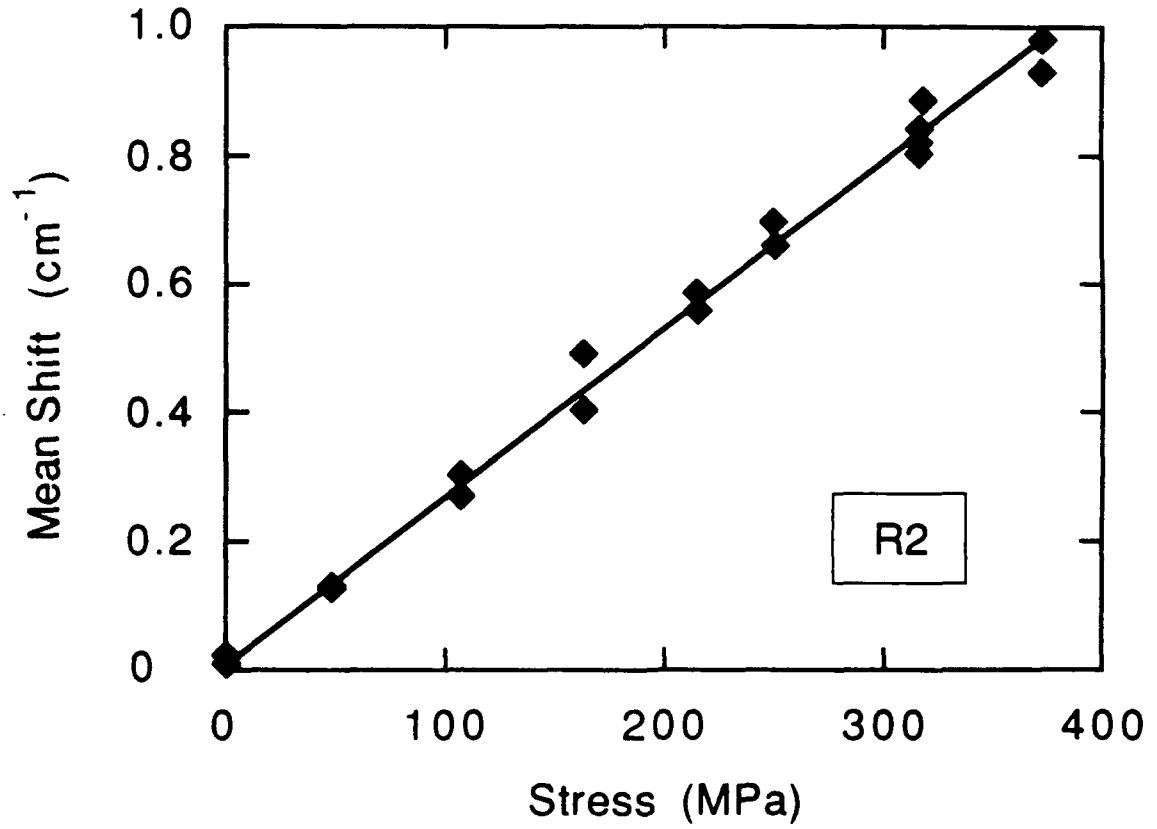
1.0
0.8
0.6
0.4
0.2
0
Mean Shift (cm^{-1})
R2
0
100
200
300
400
Stress (MPa)

Fig. 4

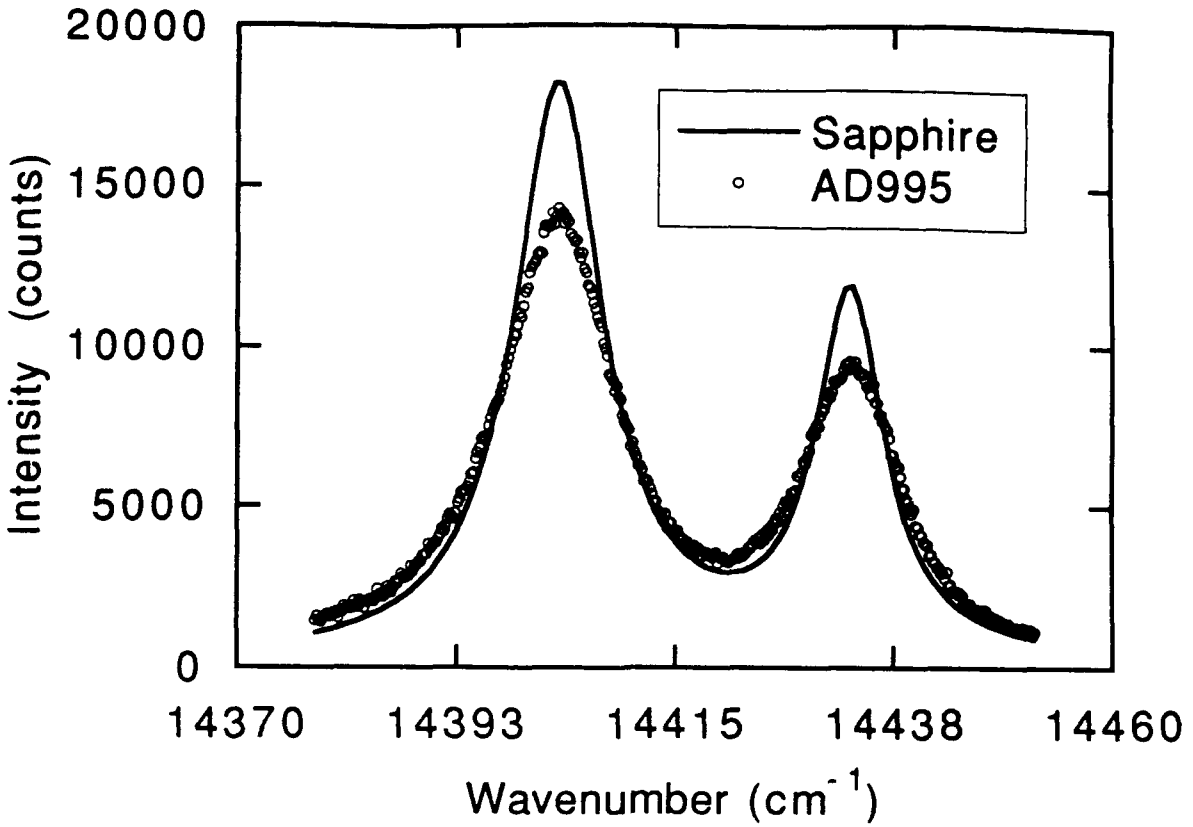
20000
15000
10000
5000
0
Intensity (counts)
Sapphire
AD995
14370
14393
14415
14438
14460
Wavenumber (cm-1)

Fig. 5

Ferroelectrics, 1992, Vol. 129, pp. 119–126
Reprints available directly from the publisher
Photocopying permitted by license only

ACOUSTIC EMISSION DURING POLARIZATION SWITCHING IN FERROELECTRIC CERAMICS

WUYI PAN

Materials and Metallurgical Engineering Department, New Mexico Institute of Mining and Technology, Socorro, NM 87801 USA

and

HENGCHU CAO

Materials Department, University of California, Santa Barbara, CA 93106 USA

(Received August 18, 1991)

Acoustic emission associated with the *polarization switching* in ferroelectric ceramics is investigated. Under bipolar ac electric field driving, whereby ferroelectric ceramics undergo a transition between the macroscopically poled and depoled states, the acoustic emission signal is large in the poled state and small in the depoled state. Under unipolar electric field driving, whereby a prepoled ferroelectric ceramic sample does not experience a macroscopic polarization reversal, the acoustic emission signal obtains the maximum amplitude at an intermediate polarization level. Furthermore, the acoustic emission signal decreases as the induced ferroelectric polarization decreases after ferroelectric fatigue. These phenomena have been interpreted by attributing the AE signal to the elastic energy release associated with the domain switching and the transmission of the elastic waves via a *electromechanical coupling*.

INTRODUCTION

Recently, ferroelectric switching has been explored for a number of potential applications. Typical examples are the ferroelectric thin films for non-volatile memory device,[1] translucent ferroelectric ceramics and thin films for optical information storage,[2] switchable antiferroelectric ceramics for high strain displacement transducer,[3] and soft ferroelectric ceramics for non-volatile displacement actuator.[4] Ferroelectric domain switching can induce a longitudinal strain of up to 0.5%, which can cause mechanical failure upon electric field excitation.[4] Consequently, in-situ measurement of acoustic emission during the device operation has been proposed for failure prediction.[5] In an early work, an in-situ measurement has indicated that under the bipolar field driving the AE signal for the square loop PLZT(3/52/48) was most pronounced at the coercive field and minimal beyond that. The authors[5] attribute this to the pronounced polarization switch around the coercive field, where the macroscopic depoling took place. However, for PLZT(3/52/48) ceramics driven by a unipolar ac electric field and for relaxor ferroelectric PLZT(9/65/35) driven by a bipolar ac field, no AE signal was detected. The authors attributed the missing of AE signal to the absence of polarization switching in these two cases.

Acoustic emission signals come from the stress waves generated during the events of elastic energy release within a solid body.[6] Domain switching and crack extension are the two basic mechanisms of the acoustic events in ferroelectric ceramics under applied electrical and/or mechanical fields. The energy stored in the stress wave

must be transmitted to the sensor/sample interface to be detected. In ferroelectric materials, this process involves electromechanical coupling. Consequently, the AE signals detected from the ferroelectric ceramic sample should be a function of the degree of poling. This behavior has not been revealed in a previous observation.[5] Namely, the AE signal amplitude is maximal at the polarization switching and minimal when the poling is established. It is the intent of this study to examine the effect of electromechanical coupling on the detected AE signals from ferroelectric ceramics under an ac electric field driving.

PHYSICAL BACKGROUND

Acoustic emissions are stress waves of 1 kHz to 3 MHz in frequency, that are generated inside the body of a material being deformed or ruptured, as a result of elastic energy release associated with the processes. The stress waves are attenuated within the body usually by reflection and scattering. By attaching a PZT sensor directly to the specimen at deformation, the signals can be correlated to the energy release associated with the events. The initial voltage output from the transducer, V_0, is shown to be proportional to the square root of the energy release, ΔE_g, during a given deformation process,[7]

$$V_0 = \psi\sqrt{\Delta E_g} \tag{1}$$

where ψ is a proportionality factor, reflecting both the preamplifier characteristics and the attenuation in the body as well as the efficiency of coupling between the sensor and the specimen. For materials that are piezoelectric, ψ involves an additional loss due to the electromechanical coupling. Specifically, the stress waves would be converted, through direct piezoelectric effect, to electric fields, which would then be converted back to stress waves through the converse piezoelectric effect. Energy transmission is involved during this process, as governed by the electromechanical coupling factor of the material. It is known that ferroelectric ceramics are also strong piezoelectric when poled, and the piezoelectricity disappears when completely depoled. The relaxor ferroelectrics are piezoelectric under a DC bias, so are the switchable antiferroelectrics when the applied electric field is high enough to cause antiferroelectric-ferroelectric phase transition. But they are not piezoelectric under a zero bias. Therefore, the electromechanical attenuation of the AE signals within a ferroelectric materials is a function of the polarization state.

Under an ac electric field driving, the ferroelectric ceramics experience constantly poling and depoling in association with domain switching. A large mismatch strain is involved in the process due to the high anisotropic mechanical and dielectric properties along different crystallographic directions, leading to an elastic energy release during the switching. On the other hand, the relaxor ferroelectric and antiferroelectric do not exhibit remanant polarization and the associated domain structure at zero bias. The relaxor ferroelectrics experience a microdomain to macromain phase change when a high bias is applied. Similarly, the antiferroelectric material undergoes an antiferroelectric to ferroelectric phase change under a high bias. However these phase change processes are more homogeneous throughout the body and involves less constraint deformation. As a result, the energy associated

with these processes is less than that involving domain switching in normal ferroelectrics. Another important acoustic emission event involves crack propagation, both from the macrocrack and microcracks. When microcrack propagates in a ceramic body, the energy release associated with cleavage of a single grain of diameter d is,[6]

$$\Delta E_g \cong \left(\frac{\sigma^2}{2E}\right) d^3 \tag{2}$$

where E is the Youngs modulus of the material and σ is the internal stress at which fracture takes place.

In summary, according to Equation (1), the measured signal reflecting V_0 will obtain a larger value for an event involving large ΔE_g and when the ferroelectric is at a high polarization state.

EXPERIMENTAL PROCEDURES

Ceramic samples studied in this investigation include three ferroelectric ceramics: normal ferroelectric, switchable antiferroelectric, and relaxor ferroelectric ceramics. The preparations of the antiferroelectric [$Pb_{0.97}La_{0.02}(Zr_{0.53}Ti_{0.12}Sn_{0.35})O_3$], ferroelectric [$Pb_{0.95}La_{0.05}(Zr_{0.585}Ti_{0.415})_{0.99}O_3$], and relaxor ferroelectric [0.9 $Pb(Mg_{1/3}Nb_{2/3})O_3$: 0.1 $PbTiO_3$] ceramic samples were described in References 3, 4 and 8 respectively. Thin specimens were cut from each of the three sintered ceramic body and fine-ground to square plates of dimensions 1 cm × 1 cm × 0.25 mm and 1 cm × 0.5 cm × 0.3 mm for the antiferroelectric and the ferroelectric respectively, and to disc plate of dimension Φ 1.25 cm × 1 mm for the relaxor ferroelectric ceramic. The thicknesses of the samples were chosen in such a way that high enough electric field can be applied to the specimen to complete ferroelectric switching for each material. The electrode was put on the specimen either by a metallic silver sintering technique in the case of antiferroelectric ceramic or by a gold sputterig deposition technique for normal and relaxor ferroelectric ceramics.

The dielectric hysteresis loops of these ceramic samples were obtained using a simple Sawyer-Tower circuit. The AE signals were detected using an acoustic emission sensor and associated amplification system (Acoustic Emission Inc.). The samples were placed on the sensor with one major surface in contact with the sensor (Figure 1). A small piece of alumina was placed on top of the sample to ensure good contact between the sample and sensor. In addition, a thin layer of organic coupling agent was applied in between. The acoustic emission signal and the P-E signals from the Sawyer-Tower system were simultaneously acquired using an IBM computer with a 16-bit data acquisition board.

The PLZT specimens were continuously driven by a 1 Hz electric field of triangular waveform until the polarization was reduced to less than two thirds of what was obtained from the fresh sample, a process referred to as ferroelectric fatigue.[8] Acoustic emission experiment was then conducted on the fatigue specimens without modifying the driving condition.

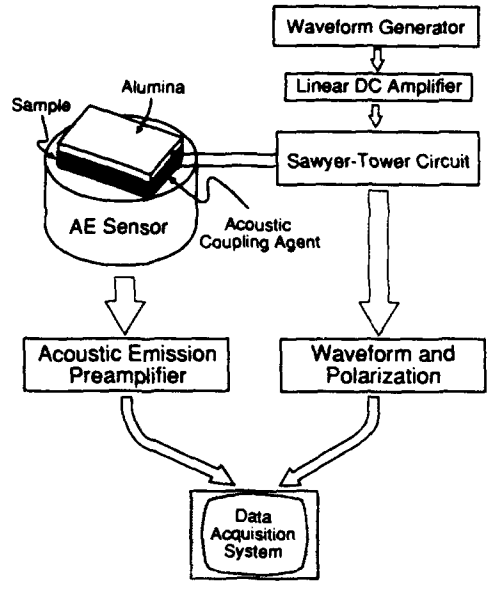

FIGURE 1 A schematic for the simultaneous measurement of acoustic emission and of ferroelectric polarization.

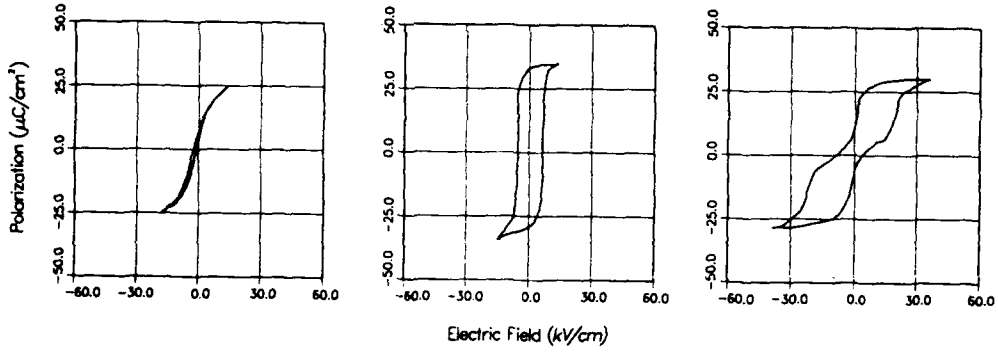

FIGURE 2 Dielectric hysteresis loops (0.1 Hz) of three typical ferroelectric types of ceramics: a) Relaxor ferroelectrics; b) Normal ferroelectrics; c) Antiferroelectrics.

RESULTS AND DISCUSSIONS

The P-E hysteresis loops for the three different ferroelectric ceramic samples are shown in Figure 2. The relaxor ferroelectric, normal ferroelectric, and antiferroelectric ceramic samples display the slim, square and double hysteresis loops respectively. The ferroelectric polarization and AE signal in-situ measurement results for the three different ceramics are shown in Figure 3. The three plots have one common feature, that is, the AE signal amplitude is minimal when polarization is being reversed, and maximal when the poling is established. Clearly, the electromechanical coupling plays an important role in governing the amplitude of the detected AE signal. At the maximum electromechanical coupling state (poled

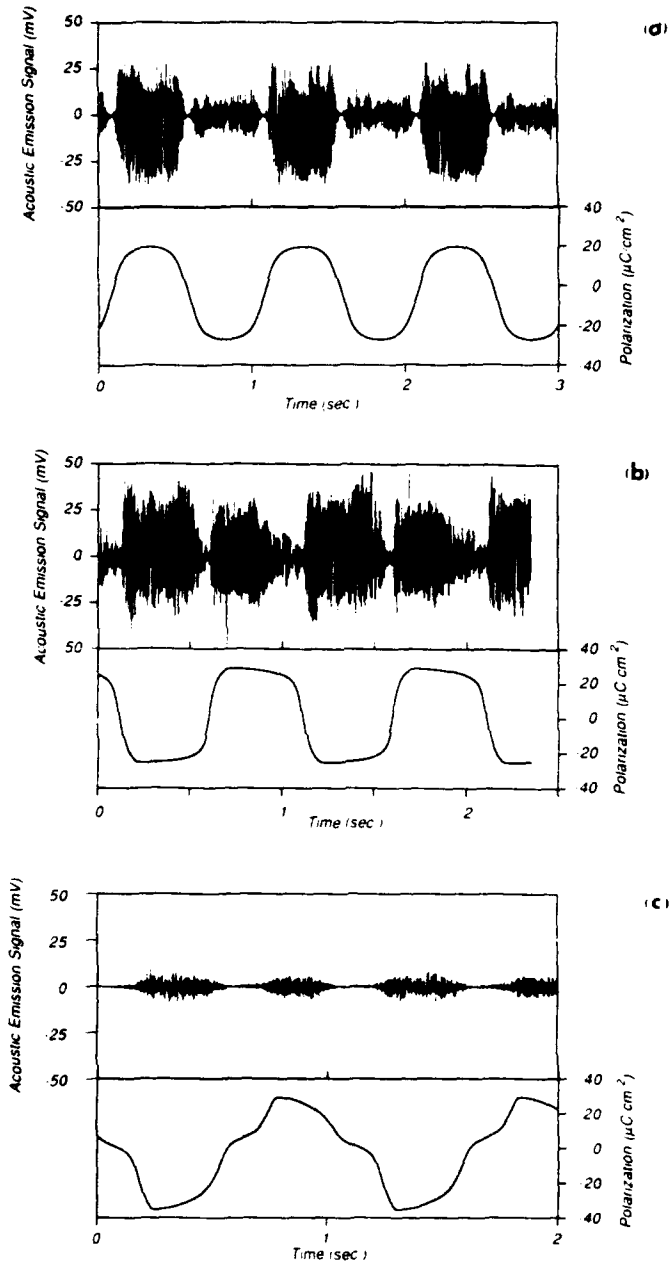

FIGURE 3 Acoustic emission signal and ferroelectric polarization versus time for three ferroelectric ceramics: a) Relaxor ferroelectrics; b) Normal ferroelectrics; c) Antiferroelectrics.

state), the AE signal is strong, while at the minimum electromechanical coupling state (depoled state) the AE signal is weak.

Figure 4 shows the result of the in-situ measurement of unipolar field induced polarization and the corresponding AE signal in the poled 5/58.5/41.5 PLZT ceramic

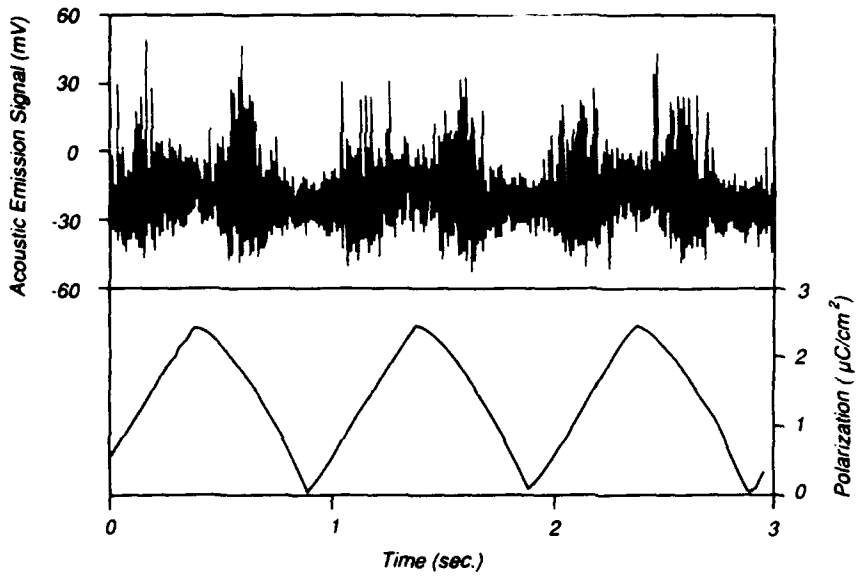

FIGURE 4 Acoustic emission signal and ferroelectric polarization versus time for PLZT (5/58.5/41.5) ceramic under a unipolar triangular electric field driving.

sample (the poling field is in the same polarity as the unipolar field). Again substantial AE signals were observed even though no remnant polarization depoling was experienced by the sample under the unipolar field driving. In this case, the acoustic emission signal amplitude is more uniformly distributed compared with that of the same ceramic under the bipolar ac field driving. This is because the remnant polarization, which is the origin of the electromechanical coupling, is not depoled under the unipolar ac field driving. From the graph, it is noted that the maximum AE signals occurs neither at the maximum induced polarization level nor at the zero polarization, but at an intermediate polarization level. The AE signal variation can be attributed to the variation of the domain switching under the applied electric field. Zhang *et al.*[9] demonstrated that in poled PZT ceramics, the irreversible domain wall motion can be excited by a field above a threshold field which is smaller than the macroscopic coercive field. When the field induced polarization increases from zero to the maximum, the polarizations are switched to the direction of the applied electric field. Near the zero polarization (zero electric field), the applied electric field is too small to switch a large number of polarization vectors, therefore the AE signal is small. Near the maximum induced polarization level, on the other hand, most of the switchable polarization vectors are already switched to the direction of the applied electric field, the polarizability near the maximum polarization level come largely from dielectric permittivity of the poled ceramics. So the AE signal is also small. The polarization switching contributes more to the polarizability in an intermediate polarization level, and the AE signal is thus maximal at an intermediate polarization level. When the field induced polarization decreases from the maximum polarization level to zero, the oriented polarization vectors drop back. That occurs before the applied electric field decreases to zero because these polarization vectors are not a part of the remnant

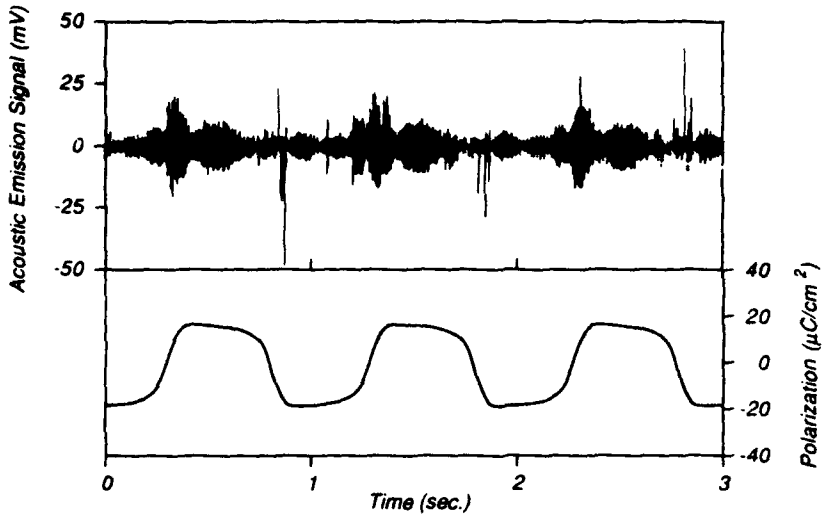

FIGURE 5 The acoustic emission signal of PLZT (5/58.5/41.5) and associated polarization versus time for a partially fatigued ferroelectric (PLZT 5/58.5/41.5) under a bipolar triangular wave driving.

polarization. Therefore the maximum AE signal also occurs at an intermediate polarization level as the driving field diminishes.

The effect of ferroelectric fatigue on the AE signal is displayed in Figure 5 for PLZT (5/58.5/41.5) specimen. When the ferroelectric polarization is reduced by fatigue, the AE signal decreases accordingly. This is consistent with above observations on three ferroelectric types of materials, because the orientable polarization, which is responsible for the electromechanical coupling under poled state, is reduced after fatigue.

It may also be seen from Figure 3 that the AE signal for the antiferroelectric ceramic sample is substantially smaller than that of the normal ferroelectric sample although the contact area of the antiferroelectric ceramic sample is larger than that of the normal ferroelectric ceramic sample. This may be attributed to the phase switching in antiferroelectric ceramic sample. The deformation of antiferroelectric ceramic sample under the applied electric field is more homogeneous inside the body and consequently fewer AE signals are generated.

CONCLUDING REMARKS

Experiments have been conducted on three typical ferroelectric ceramics to investigate the effects of electromechanical coupling on the acoustic emission under ac electric field driving. It has been demonstrated that the AE signals are due to the events of domain switching and the signal amplitude is strongly dependent upon the polarization state in the body as a result of the electromechanical coupling. Ferroelectrics involving domain switching generate significantly higher AE signal than phase change ferroelectrics (such as relaxor ferroelectrics and antiferroelectrics). Under the same macropolar state, the AE signal amplitude depends on the homogeneity of the internal strains.

ACKNOWLEDGEMENTS

The authors wish to thank Dr. A. G. Evans for the discussions on acoustic emission testing of ceramics. Financial support for this work is provided by DARPA/URI under ONR contract number N00014-86-K-0753.

REFERENCES

1. D. Bondurant, "Ferroelectric RAM Memory Family for Critical Data Storage," *Ferroelectrics*, **112**, 273–282 (1990).
2. C. E. Land, "Longitudinal Electrooptical Effect and Photosensitivities of Lead Zirconate Titanate Thin Films," *J. Amer. Ceram. Soc.*, **72**, 2059–2064 (1989).
3. W. Y. Pan, C. Q. Dam, Q. M. Zhang and L. E. Cross, "Large Displacement Transducers Based on Field-forced Transition in Tetragonal $(Pb_{0.97}La_{0.02})$ (Ti,Sn,Zr)O_3 Ceramics," *J. Appl. Phys.*, **66**, 6014–6023 (1989).
4. W. Y. Pan, Q. M. Zhang, Q. Y. Jiang and L. E. Cross, "Electric Field Induced Strain in (Pb,La)(Ti,Zr)O_3 Ferroelectric Ceramics near the Tetragonal-Rhombohedral Morphotropic Phase Boundary," *Ferroelectrics*, **88**, 1 (1989).
5. Kenji Uchino, Terukiyo Hirose and Ande Murali Varaprasad, "Acoustic Emission in Piezoelectric/Electrostrictive Actuators," *Japan. J. Appl. Phys.*, **26**, (supplement 26-2), 167–170 (1987).
6. A. S. Tetelman and A. G. Evans, "Failure Prediction in Brittle Materials Using Fracture Mechanics and Acoustic Emission," Fracture Mechanics of Ceramics, Vol. 2, (Eds. R. C. Bradt, D. P. H. Hasselman and F. F. Lange), Plenum Publ. Co. New York, pp. 895–924 (1974).
7. D. Harris, A. S. Tetelman and F. Darwish, Acoustic Emission Testing, ASTM, Philadelphia, STP 505, p. 238 (1972).
8. W. Y. Pan, E. Furman, G. O. Dayton and L. E. Cross, "Dielectric Aging Effects in Doped Lead Magnesium Niobate: Lead Titanate Relaxor Ferroelectric Ceramics," *J. Mater. Sci. Lett.*, **5**, 647 (1986).
9. Q. M. Zhang, W. Y. Pan, S. J. Jang and L. E. Cross, "Domain Wall Excitations and Their Contributions to the Weak-Signal Response of Doped Lead Zirconate, Titanate Ceramics," *J. Appl. Phys.*, **64**, 6445–6451 (1988).

MATERIALS

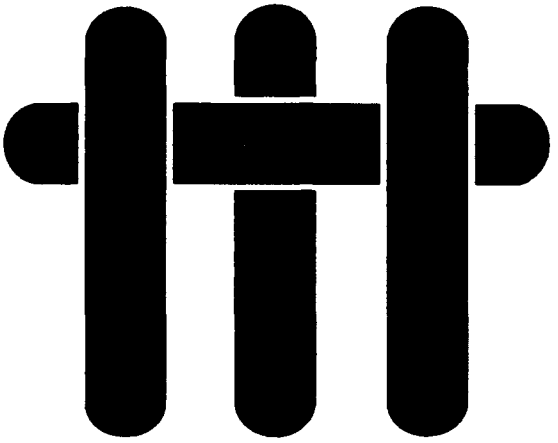

ELECTRIC FIELD-INDUCED FATIGUE CRACK EXTENSION IN FERROELECTRIC CERAMICS

by

Hengchu Cao and A. G. Evans
Materials Department
College of Engineering
University of California
Santa Barbara, California 93106–5050

June, 1992

To be finished

KJS-2•Post-Docs•Cao•TA-Elctr Fld 92/045/06•1:42 PM•4/6/92

ABSTRACT

In advanced actuator applications, ferroelectric ceramics are subjected to large alternating electric fields, which may induce cracking and mechanical degradation phenomena. This article describes an experimental procedure for characterizing crack extension from preexisting flaws in ferroelectric ceramics subject to high amplitude but low frequency electric fields. Fracture mechanics concepts are applied to interpret the observed cracking. Implications for the mechanical reliability of multilayered ferroelectric actuators are discussed.

MATERIALS

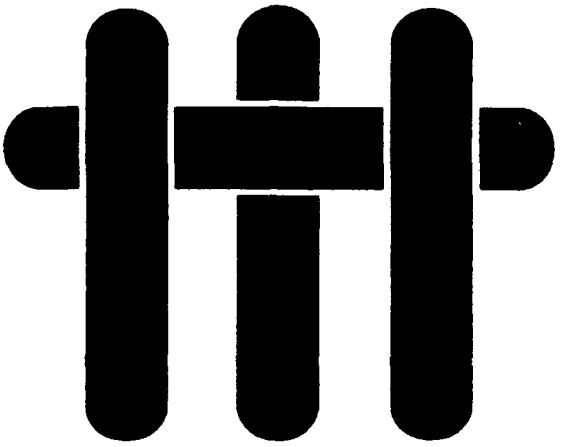

NON-LINEAR DEFORMATION OF FERROELECTRIC CERAMICS

by

H.C. Cao and A.G. Evans
Materials Department
College of Engineering
University of California
Santa Barbara, California 93106–5050

May 30, 1991

KJS-Evans-27•De-DI•TA-Dfrm Frict 91/07/10•4:36 PM•4/2/92

Submitted to the J. Am. Ceram. Soc

ABSTRACT

For ferroelectric ceramics used either as sensors or as actuators, the mechanical behavior of the material dictates the overall electromechanical response. Furthermore, in advanced actuator systems, the material may be subject to high stresses and large deformations, leading to non-linearity and degradation of the mechanical performance. A preliminary experimental investigation has been undertaken to study this response. For this purpose, polarization and strain are measured continuously on a compression cuboid. Severe non-linear and hysteretic behavior is observed in many cases. An attempt has been made to establish the constitutive laws applicable to this non-linear deformation.

1. INTRODUCTION

Multilayer ferroelectric ceramics are used as actuators and sensors.[1,2] Many advanced applications require either large actuator displacements or large forces. Such conditions may cause non-linearity, as well as permanent deformation, of both the ferroelectric and the metal electrodes, leading to degradation of the performance of the actuator.[3-5] Consequently, it is essential to thoroughly characterize the constitutive behavior before these materials can be successfully integrated into systems. Procedures for establishing the constitutive laws are developed in this study. The non-linearities are most pronounced in the vicinity of stress concentrations that occur near edges[6] and in association with flaws.[7-8] The latter may be present either in the ferroelectric or at the ferroelectric/electrode interface. Edges as well as flaws in the ferroelectric and at interfaces and thus afforded particular emphasis.

Two of the most frequently used actuator/sensor configurations are addressed: multilayer and annular (Fig. 1). The multilayer design (Fig. 1a) has been used for piezoelectrics and relaxor ceramics[6] as well as capacitors.[9] In this design, the stresses induced by the actuator displacements are aligned with the polarization. In the annular design (Fig. 1b), the induced stress axis is *normal* to the polarization direction.

Some early studies indicated that poled ferroelectrics are prone to non-linear deformation upon compression along the poling direction.[3] As a result, the remnant polarization is partially eliminated. Conversely, stresses applied *perpendicular* to the poling direction are believed to stabilize the polarization. The non-linear effects are attributed to domain switching, induced by the mechanical loads.[10] A more detailed study of these effects is presented in this article. An attempt is also made to rationalize the observed stress/strain curves with respect to the interplay between ferroelectric and ferroelastic domain switching.

2. EXPERIMENTAL PROCEDURES

2.1 Materials and Specimen Preparation

Ferroelectrics considered for large displacement actuator applications are of three types[11-12] (Table I): i) piezoelectrics; ii) ferroelectric relaxors; iii) antiferroelectrics. Accordingly, the electromechanical constitutive laws for each of these material types are explored. Poled piezoelectrics, PZTs, were obtained from a commercial source‡: PZT-A (Zr/Ti = 52/48) with hard dopants (Ba and Fe) and PZT-B (Zr/Ti = 53/47) with soft dopants (Nb). Relaxor materials, with composition 0.9 PMN–0.1 PT, were prepared through conventional solid-state sintering and by hot-pressing. The antiferroelectric, with a composition $Pb_{0.97}\ La_{0.02}\ (Ti_{0.64}\ Ti_{0.09}\ Sn_{0.27})\ O_3$, was sintered from a mixture of reagent-grade oxides.

Short compression cuboids with nominal dimensions 6 x 8 x 12 mm were cut from bulk ferroelectrics and all non-electroded faces ground, using a resin-bond diamond wheel. In some cases, one of the side faces was polished to facilitate observations during testing. For the relaxor and antiferroelectric materials, gold electrodes were deposited onto the top and bottom faces. In all cases, the electrodes were connected to a large capacitor for polarization measurement.

2.2 Testing and Measurements

Uniaxial compression testing of brittle materials is notoriously difficult, given the requirement that the load be applied at the geometric center to eliminate bending. Nearly perfect alignment is essential in order to characterize the non-linear deformation. Consequently, a special loading fixture (Fig. 2) has been designed to facilitate the alignment procedure and also to provide a means for recording the electric displacement. Two spherical cones were incorporated with two flat alumina blocks

---

‡ Channel Industries, Inc., Goleta, California.

used to insulate the electrodes. Specimens were carefully emplaced at the center between the alumina blocks. The fixture was then incorporated into a servohydraulic machine for testing. Final adjustments needed to minimize bending were made through *in situ* measurement of the strain differential upon exposing the specimen to loading/unloading cycles, within a very small range (< 5 MPa). The specimen was connected in a closed loop with a large capacitor, having capacitance five orders of magnitude larger than the specimen (Fig. 2). In this case, the voltage change across the capacitor, measured by a voltage follower, provided an indication of the charge transfer from the specimen to the capacitor.‡ Consequently, the polarization change, ΔP, could be obtained as

$$\Delta P = C_o V \tag{1}$$

where C_o is the capacitance of the shunt capacitor and V is the voltage measured across the capacitor. The convention adopted here is that *depolarization* is indicated by *positive* ΔP.

Other quantities measured simultaneously with the voltage include the load instantaneously carried by the specimen obtained from the load cell output of the testing machine. Also, bi-directional strain gauges were emplaced on two opposing side faces to measure the deformation along both the loading and transverse directions, as well as monitor possible bending caused by misalignment. The strain component along the *loading* direction is designated, ε_z. For specimens tested with the loading perpendicular to the polar axis, the strain along that axis is designated, ε_x, and the other normal strain, ε_y. When the loading is parallel to polar axis, $\varepsilon_x = \varepsilon_y$. Positive quantities for *stress*, and *strain*, denote *compression*, unless otherwise indicated.

---

‡ It is emphasized that the change in voltage is minimal.

3. RESULTS

3.1 Piezoelectric PZT

The deformation behavior found for hard and soft PZTs subject to stress applied *parallel* to the poling direction has similarities and important differences (Fig. 3). Both materials are non-linear when the stress exceeds ~ 20 MPa, and exhibit similar permanent deformations (~ 0.5%) after exposure to stresses above 500 MPa. The major difference occurs upon unloading. In the *"soft" material* (PZT-B), the non-linear deformation is nonrecoverable, at stress levels as low as 30 MPa (Fig. 3a). Conversely, the *"hard" material*, PZT-A, recovers most of the non-linear deformation, with considerable hysteresis (Fig. 3b): a phenomenon usually referred to as *anelastic* deformation. However, the capacity for *anelastic* strain is destroyed at stress > 300 MPa.

The strain measurements indicate that the volume strains ($\varepsilon_z + \varepsilon_x + \varepsilon_y$) are essentially linear for both material (Fig. 4). Consequently, the non-linear deformation is related *solely to the deviatoric* components of stress, σ', and strain, ε' (Fig. 5). The instantaneous Poisson's ratio (Fig. 6) reflects this feature. It increases initially, reaches a maximum, decreases upon further loading and finally, approaches a value characteristic of incompressible plastic flow (0.5). The deviatoric stress/strain curves have a form (Fig. 5) characteristic of that found for phase transformations, consisting of i) an initial hardening regime wherein the hardening-rate *diminishes* as the stress increases, followed by ii) a regime of *accelerated* hardening, as a saturation plastic strain is approached. Consequently, the stresses σ' and plastic strain, ε'_p, can be described by a bifunctional power law expression,

$$\sigma'/\sigma'_o = \left(\varepsilon'_p/\varepsilon'_o\right)^a + \left(\varepsilon'_p/\varepsilon'_o\right)^b \qquad (2)$$

where a and b are empirical power law coefficients ($a < 1$ and $b > 1$), σ'_0 is a reference stress and ε'_0 a reference strain. The magnitudes of the coefficients for the hard and soft materials are summarized in Table II.

For the both materials, the charge on the capacitor changes during loading, expressed as a depolarization, ΔP. The depolarization curves (Fig. 7) for each material resemble the corresponding stress/strain curves (Fig. 3), suggesting that the sources of the non-linear deformation are also responsible for the polarization changes. The total depolarization measured after a stress exposure of ~ 500 MPa is ~ 80% of the remnant polarization induced upon poling.

The stress/strain curves obtained when the stress is applied *normal* to the poling direction are qualitatively the same (Fig. 8) but exhibit more limited non-linearity. For example, the permanent strain in the soft material (~ 0.3%) is about half that obtained upon loading along the poling axis. However, the transverse strains ε_x and ε_y (Fig. 9) have *opposing* non-linearities, as a result of the anisotropy caused by poling.

The depolarization curves exhibit features (Fig. 10) dramatically different from those evident upon loading along the poling axis. Initially, the polarization *increases* as the strain increases, but when the strain exceeds ~ 0.1%, an inversion occurs and the polarization begins to *decrease* with continued straining.

3.2 Relaxor PMN·PT

The uniaxial compressive stress-strain curves obtained for PMN·PT (Fig. 11) indicate linear elastic behavior up to an axial stress, $\sigma_z \approx 500$ MPa. Thereafter, some non-linear deformation appears. Finally, at $\sigma_z \approx 600$ MPa, fracture occurs and the specimen fragments. Both the transverse strain and volume strain (Fig. 12) suggest that this non-linearity is connected with *microcracking*.[13-14] Notably, the volume *decreases* initially, in accordance with linear elasticity, such that the volume strain ε_v is given by,

$$\varepsilon_v = -(1-2\nu)\sigma_z/E \qquad (3)$$

where E is Young's modulus and ν is Poisson's ratio (see Table I). However, as non-linearity begins, *dilatation* occurs that exceeds the elastic shrinkage. At failure, a net 0.1% volume expansion is evident. Such dilatations are typical of microcracking effects upon compression loading of brittle solids.[14,15]

There were no polarization changes in this material, consistent with the PMN·PT being mostly paraelectric (at room temperature) and having no remnant polarization.

3.3 Antiferroelectric PLSnZT

Appreciable non-linear deformation is observed in an antiferroelectric PLSnZT at a stress slightly higher than 20 MPa* (Fig. 13). Some of this deformation is permanent, manifest in the unloading/reloading hysteresis. Further loading (beyond $\sigma_z \approx 100$ MPa) causes stiffening, apparent in the increased tangent modulus. The hysteresis loop then becomes slimmer. After the specimen has been loaded beyond ~ 500 MPa, the material reverts to essentially elastic behavior. The total permanent deformation from the virgin state is about 0.13%. The final tangent modulus at saturation is ~ 160 GPa, compared with an initial value of 130 GPa. The compressive strength is ~ 900 MPa at a failure strain ~ 0.8%. The Poisson's ratio decreases from its initial value ($\nu \sim 0.35$) to a *final* value (~ 0.25 at strains > 0.6%) (Fig. 14), typical for oxide ceramics.

No polarization change occurred, consistent with the overall polarization being zero for antiferroelectrics.

---

* No orientation distinction is necessary. Antiferroelectric materials do not exhibit remnant polarization. They are isotropic with respect to mechanical and electrical properties at zero field and stress.

4. NON-LINEAR DEFORMATION

Since the volume strain in all materials appears to be linear and non-hysteretic (unless microcracking occurs), when non-linearity arises, it is only necessary to understand and model the deviatoric deformation: as in metal plasticity. The incremental deviatoric strain upon loading then relates to the corresponding deviatoric stress, through a constitutive law (Eqn. 2).

The mechanism responsible for the non-linear deformation in the piezoelectric and antiferroelectric materials involves 90° domain switching, having the features schematically illustrated in Fig. 15. The as-processed polycrystalline material has a nominally random set of orientations in the polarization vector, P_i. An applied electric field induces both 180° and 90° domain switching, leading to a preferred alignment of P_i in the direction of the field. Residual stress also develops in association with 90° domain switching. Poling of PZTs is conducted with a field, E_x. Subsequent stressing may be along either the z or x. For domain A (Fig. 15), oriented along z, initially $P_x = P_y = 0$ and $P_z = P_o$. This type of domain is most likely to switch during poling,‡ above a critical field, to an orientation $P_y = P_z = 0$ and $P_x = P_o$. The new orientation is stable, subject to subsequent mechanical stress σ_{zz}, but depoling is possible when a σ_{xx} stress is applied. If poling did *not* cause the domain to switch (because the field is too small), switching may be activated by a subsequent σ_{zz} stress, whereupon the domain would realign along *either* P_x *or* P_y. For domain C, the situation is similar and an electric field E_x is again likely to induce $P_y \rightarrow P_x$ switching. Domain B is most illustrative of the interplay between the electric field and stress. No domain switching can occur subject to E_x, because there is no net change in P_x upon switching from P_1 to P_2: moreover, P_x *decreases* if switching occurs from P_1 to P_3. However, upon σ_{zz} stressing, switching from

‡ In some cases, 90° domain switching upon poling may be inhibited by the strain energy increase associated with the residualization.

P_1 to P_3 is expected when the normal stress ($\sigma_1 = \sigma_{zz}/2$) reaches a critical value. This event produces a *positive* strain in ε_y but *negative* strain in ε_x and ε_z. A related mode of switching may occur upon σ_{xx} stressing.

The basic insight obtained from Fig. 15 allows the major phenomena found by experiment to be rationalized. For the *poled PZT materials*, tested with the mechanical loading axis coincident with the poling direction, the mechanical field causes switching in a sense *opposite* to that caused by poling resulting in systematic depoling. Once the depoling is complete, further switching does not occur. However, this mechanically depoled state must be contrasted and distinguished from the original (unpoled) state, in that the spaciously random polarization vectors in the virgin material are now in a plane normal to the depoling stress. "Complete depoling" results in the saturation behavior found at plastic strains > 0.5% (Fig. 3). Thereafter, the material behaves as an elastic body until microcracking commences prior to mechanical failure.

Loading *normal* to the poling axis (usually thought to be linear) causes a non-linear response best illustrated by orientation B in Fig. 15. Some of the 90° domains are unfavorably oriented for switching upon poling, but are in a preferred orientation for switching upon loading. The important consequence is the relationship found between the polarization change, ΔP, and the ε_x strain (Fig. 10). The initial portion of these curves is the normal, linear piezoelectric effect. However, type B domain switching at larger stresses causes depolarization ($-\Delta P_x$) and an expansion along the x-axis, leading to the observed *inversion* in the polarization curve.

The parameters that characterize the non-linear deviatoric stress/strain (Eqn. 2), must depend on factors such as the domain wall mobility, the residual stresses, etc. More detailed analysis is needed to develop a general yield criterion and a flow law. For this purpose, experiments involving multiaxial stresses are necessary. Furthermore, the differences found between the "hard" and "soft" PZTs should be consistent with the yield criterion and flow law. One key feature concerns the residual stresses, which are

expected to be larger in the hard material, causing the domains to switch back when the applied load is removed.

For the antiferroelectric material, the permanent strain is associated with ferroelastic domain switching, with characteristics similar to those described above for PZT. However, it is noted that electric fields cause the antiferroelectrics to ferroelectric phase transition.

5. CONCLUSION

Mechanical non-linearity found in piezoelectric and antiferroelectric materials has been attributed to ferroelastic domain switching, with a yield criterion controlled by a deviatoric effective stress. The flow rule has not been established. However, curve fitting suggests a power law at small strains, similar to metal plasticity. At larger strain, accelerated hardening occurs and the inelastic strain approaches saturation. In addition, strong interconnections have been established between ferroelectric and ferroelastic deformation. Notably, electrically "hard" PZT can sustain a large mechanical load without significant permanent deformation, whereas a "soft" PZT is susceptible to deformation at small stresses, even though the "yield" stresses are similar for the two materials. Consequently, for actuator applications, hard PZT can be used at higher stress levels, without depoling.

By contrast, relaxor ferroelectric ceramics are capable of sustaining large mechanical stresses without either mechanical degradation or non-linearity. Furthermore, the strain-polarization curves have negligible hysteresis. These characteristics render the material a good candidate for large displacement, large force actuators. In addition, among the materials investigated, this material has the highest modulus, making it possible to produce appreciable actuation displacements, while sustaining relatively large mechanical stress.

TABLE I

Materials and Properties

Material	† Dielectric Constant K_{33}^T	Coecive Field E_c (MV/m)	Saturated ~~Remnant~~ Polarization P_r (C/m^2)	Elastic Constants Y_{33}^E (GPa)	Y_{11}^E (GPa)	c_{44}^E (GPa)	Piezoelectric Constants (10^{-12}m/V) d_{33}	d_{31}	d_{15}
(Hard) PZT-A#	1300	2.4	0.35	65	82	25	300	– 135	525
(Soft) PZT-B#	1750	1.0	0.35	52	64	20	400	– 185	625
PLSnZT	800	5.1	0.31	140					
PMN•PT	20,000		0.3	255					

† K is measured at room temperature and 10 kHz.

Channel Industries, Inc., Goleta, California.

TABLE II

Constants in Deviatoric Constitutive Law (Eqn. 2)

	Exponent a	Exponent b	Reference Stress σ'_0 (MPa)	Reference Strain ε'_0 (%)
(Hard) PZT-A	0.54	9	100	0.62
(Soft) PZT-B	0.7	12	75	0.65
PlSnZT	0.65	9	100	0.2

REFERENCES

[1] L.E. Cross, "Piezoelectric and Electrostrictive Sensors and Actuators for Adaptive Structures and Smart Materials," ONR Report, Penn. State, 1990.

[2] R.E. Newnham, Q.C. Xu, S. Kumar and L.E. Cross, "Smart Ceramics," *Ferroelectrics*, **102**, 77–89 (1990).

[3] H.H.A. Krueger, "Stress Sensitivity of Piezoelectric Ceramics, Part 1: Sensitivity to Compressive Stress Parallel to the Polar Axis," *J. of Acoustical Soc. of America*, **42[3]** 636–45 (1967).

[4] H.H.A. Krueger, "Stress Sensitivity of Piezoelectric Ceramics, Part 3: Sensitivity to Compressive Stress Perpendicular to the Polar Axis," *J. of Acoustical Soc. of America*, **43[3]** 385–91 (1968).

[5] H.H.A. Krueger and D. Berlincourt, "Effects of High Static Stress on the Piezoelectric Properties of Transducer Materials," *J. of Acoustical Soc. of America*, **33[10]** 1339–44 (1961).

[6] S.R. Winzer, N. Shankar and A.P. Ritter, "Designing Cofired Multilayered Electrostrictive Actuators for Reliability," *J. Am. Ceram. Soc.*, **72**, 2246–57 (1990).

[7] Z.G. Suo, C.-M. Kuo, D.M. Barnett and J.R. Willia, "Fracture mechanics for Piezoelectric Ceramics" *J. Mech. Phys. Solids*, (1991).

[8] J.G. Pepin and W. Boyland, "Electrode-Based Causes of Delaminations in Multilayer Ceramic Capacitors," *J. Am. Ceram. Soc.*, **72**, 2287–91 (1989).

[9] A.F. Dyson, *Electrocomponent Sci. Technol.*, **11**, 53–64 (1983).

[10] D. Berlincourt, "Piezoelectric Ceramics: Characteristics and Applications," *J. Am. Ceram. Soc.*, **706[6]** 1586–95 (1981).

[11] W.Y. Pan and L.E. Cross, "Piezoelectric and Electrostrictive Materials for Transducer Applications," ONR Report, Penn. State, 1990.

[12] W.Y. Pan and L.E. Cross, "Antiferroelectric to Ferroelectric Switching in Lead Zirconia Titanate Stannate Ceramics," *Proc. of 6th IEEE Symp on Appl. of Ferroelectrics*, Lehigh Univ., June 8–11, 1986, p. 648.

[13] Y. Fu and A.G. Evans, *Acta Metall.*, **33[8]** 1515–23 (1985).

[14] B. Budiansky and R.J. O'Connell, *Intl. Jnl. Solids Structures*, **12**, 81–97 (1976).

[15] M.F. Ashby and S.D. Hallam, *Acta Metall.*, **34**, 497 (1986).

FIGURE CAPTIONS

Fig. 1. Actuator configurations: a) multilayer, b) annular.

Fig. 2. Compression loading fixture with associated measurement circuits and orientation designation.

Fig. 3. Stress/strain curves from hard and soft PZTs subject to stress along polar axis.

Fig. 4. Change in volume strain with axial stress for hard and soft PZTs.

Fig. 5. The deviator plastic strain, as it relates to deviatoric stress, is solely responsible to the non-linear deformation.

Fig. 6. Change in instantaneous Poisson's ratio with axial strain for soft PZT.

Fig. 7. Electrical depolarization, ΔP, for hard and soft PZTs as a function of the applied stress.

Fig. 8. Stress/strain curves for hard and soft PZTs when the stress is applied normal to the polar axis.

Fig. 19. Transverse strain characteristics for both PZTs as a function of applied normal stress.

Fig. 10. Polarization changes in the polar axis caused by stress applied normal to the polar axis.

Fig. 11. Uniaxial stress/strain curves for PMN•PT relaxor material.

Fig. 12. Effects of stress on a) transverse and b) volume strain for PMN•PT.

Fig. 13. Uniaxial stress/strain curve for the antiferroelectric PLSnZT.

Fig. 14. Change in the Poisson's ratio as a function of stress for PLSnZT.

Fig. 15. Schematic of deformation by domain switching.

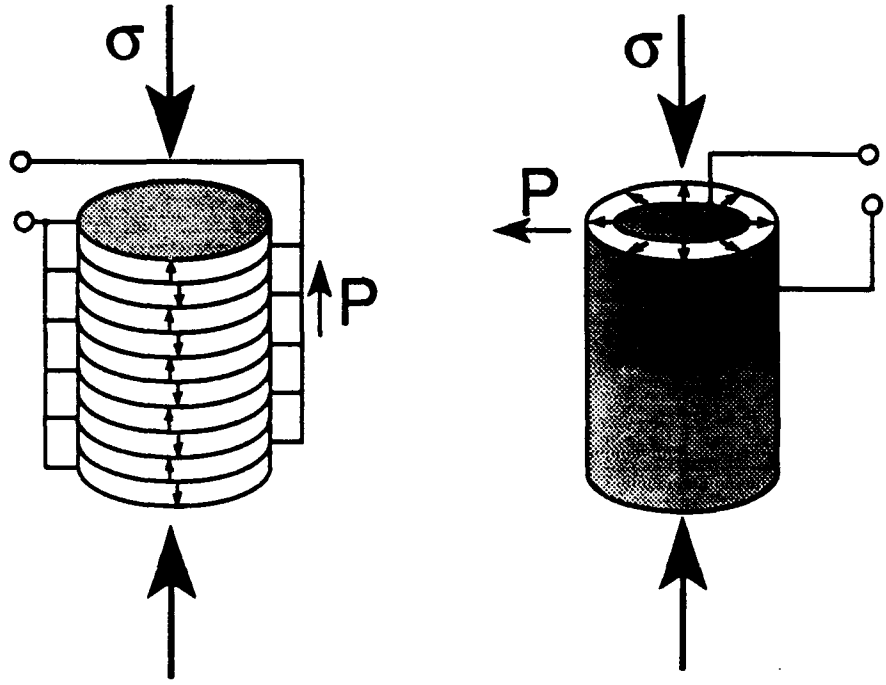

D33
Configuration

(a)

D31
Configuration

(b)

Fig. 1

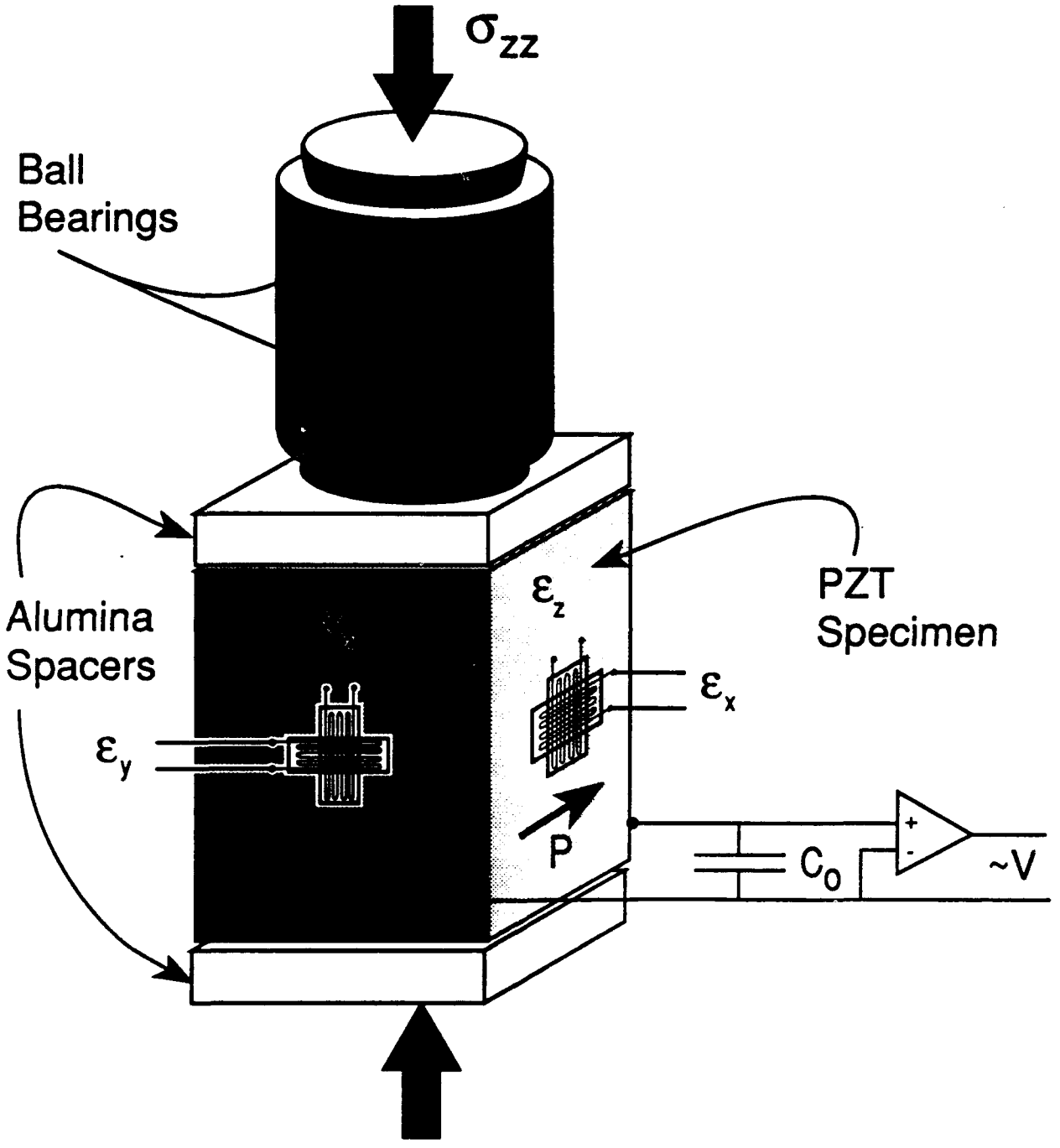
σ_{zz}
Ball
Bearings
Alumina
Spacers
PZT
Specimen
ε_z
ε_x
ε_y
P
C_0
~V

Fig. 3

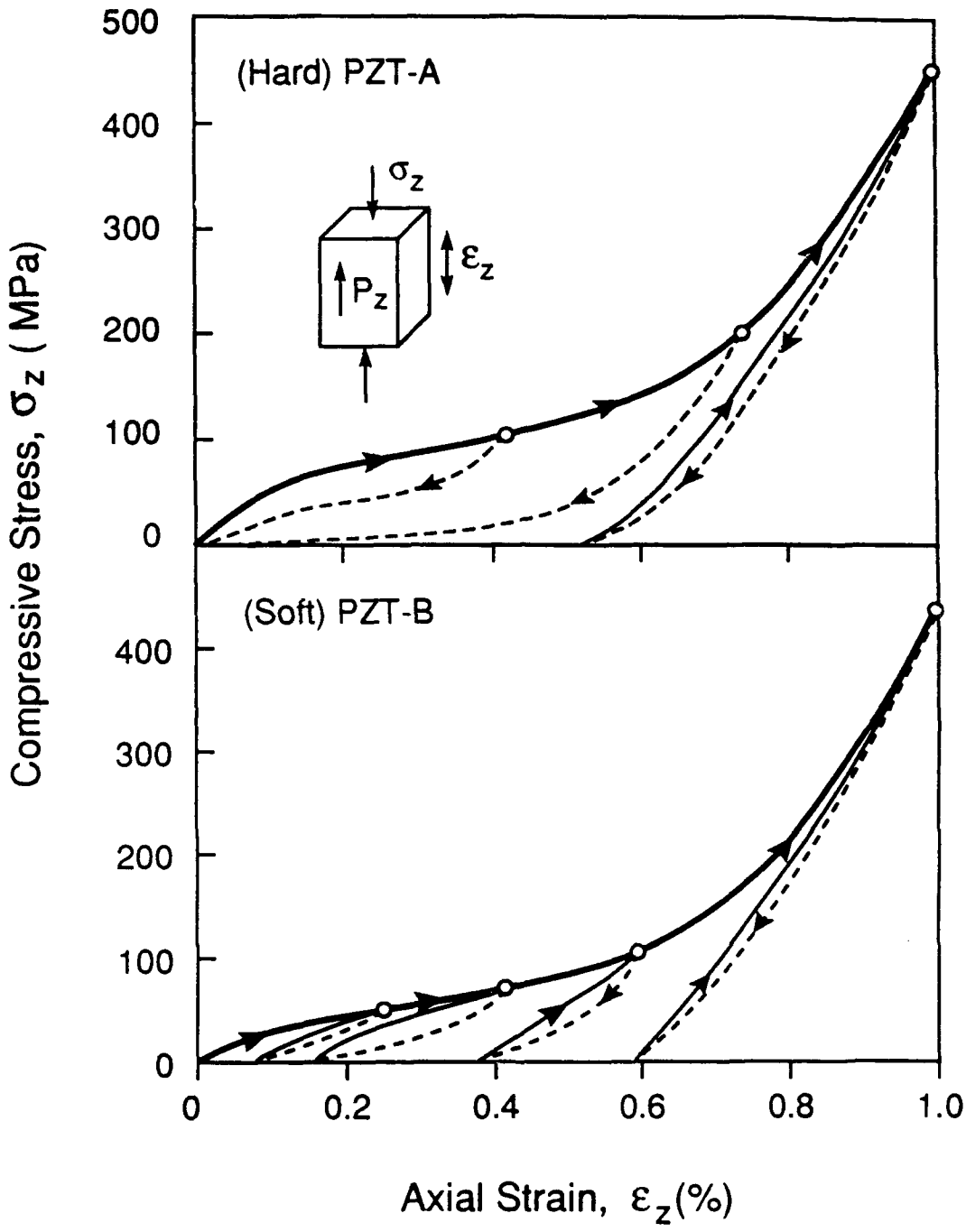
(Hard) PZT-A
(Soft) PZT-B
σ_z
ε_z
P_z
Compressive Stress, σ_z (MPa)
Axial Strain, ε_z(%)
500
400
300
200
100
0
0
0.2
0.4
0.6
0.8
1.0

Fig 3

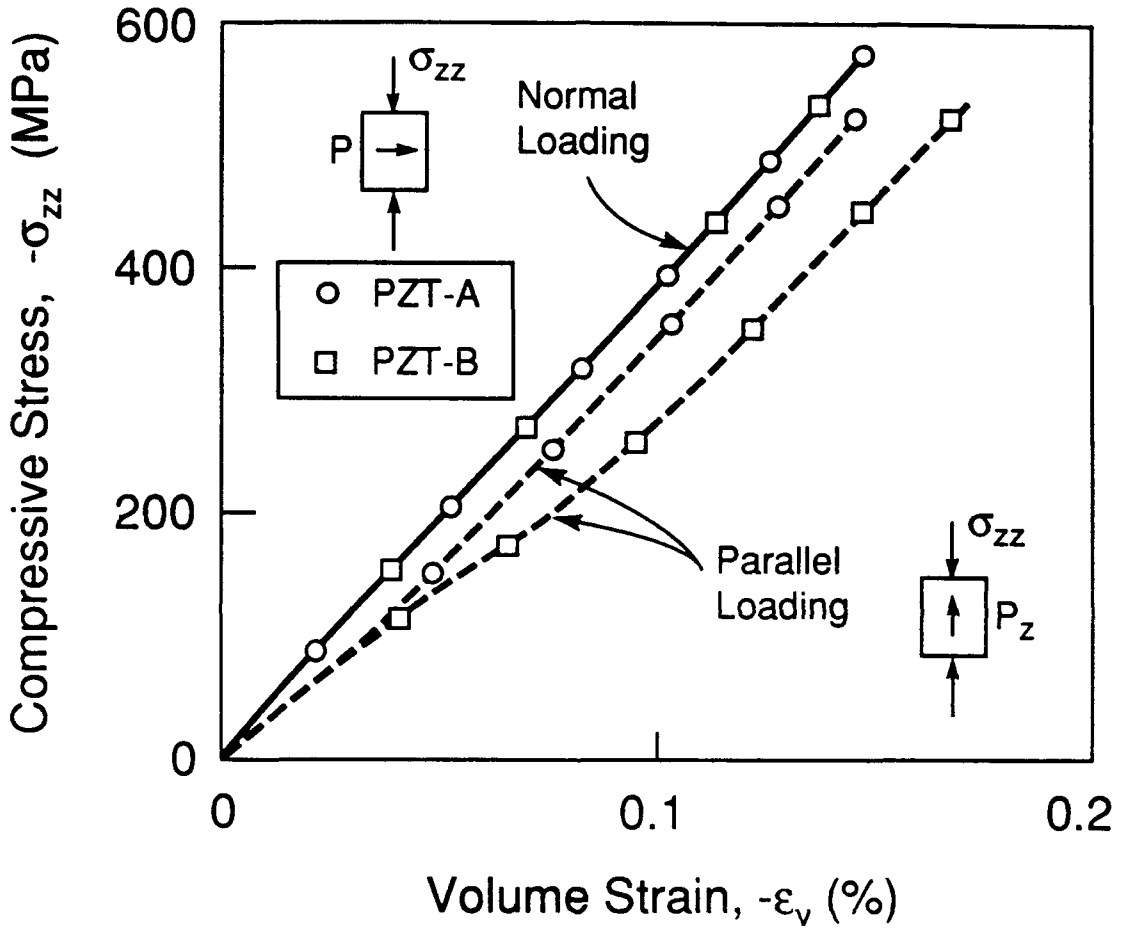

Cao:DC-3/92-amk-D4#657-2 (FIG. 4)

Fig 4

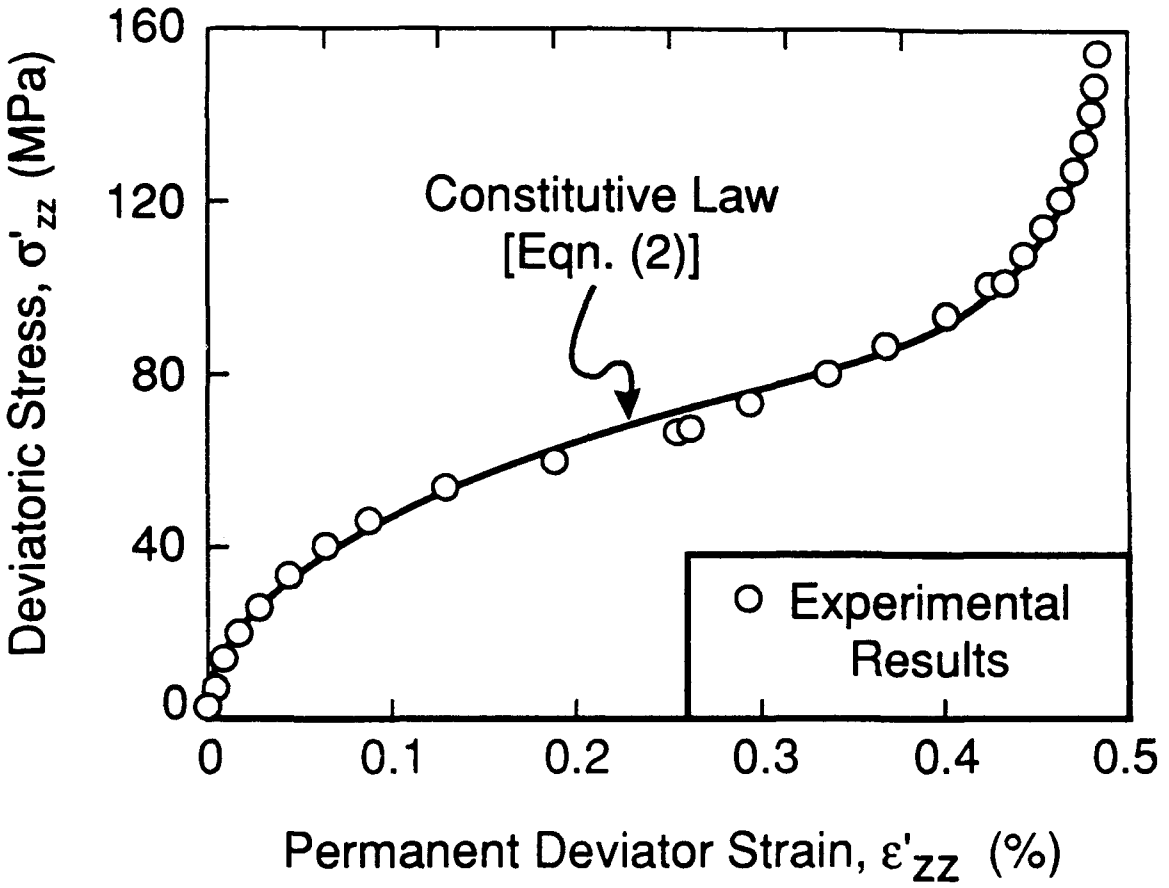
160
120
80
40
0
Deviatoric Stress, σ'zz (MPa)
Constitutive Law
[Eqn. (2)]
Experimental
Results
0
0.1
0.2
0.3
0.4
0.5
Permanent Deviator Strain, ε'zz (%)

Fig 5

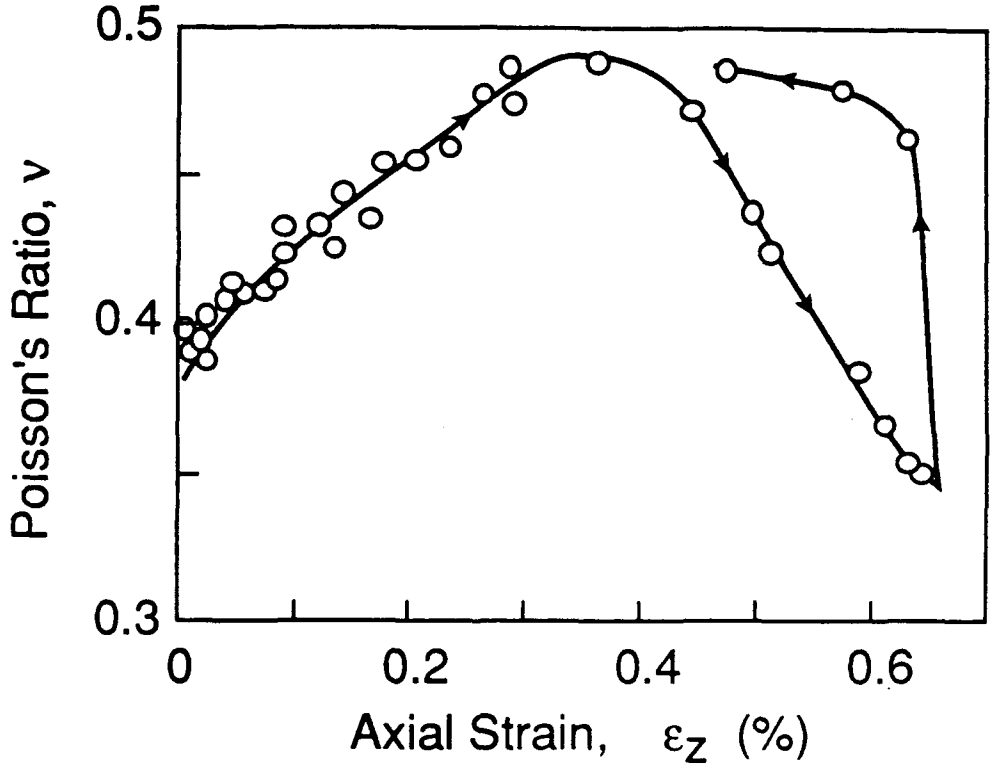

Fig 6

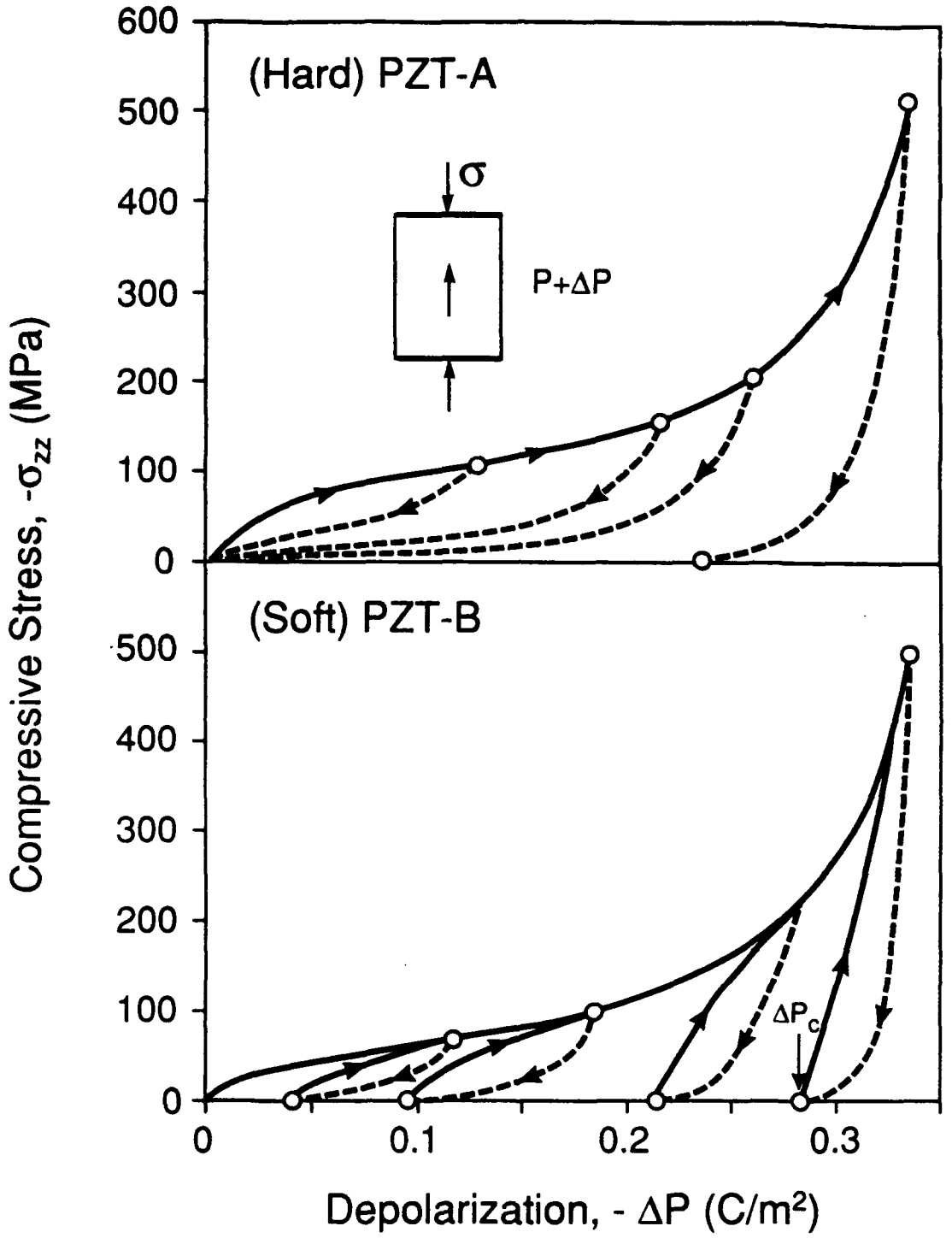

Cao.DC.3/92-amk-D46857-4 (FIG. 7)

Fig. 7

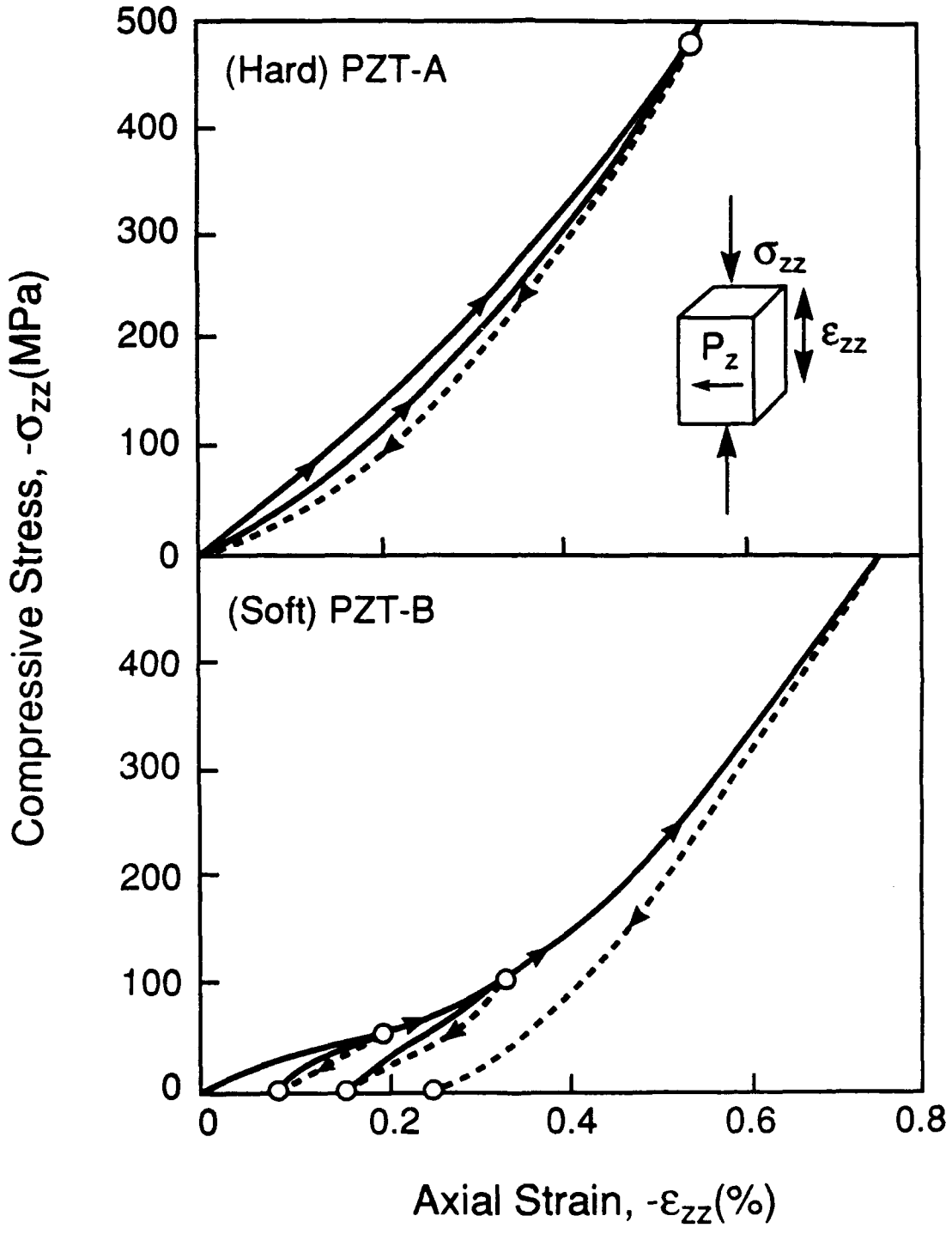
(Hard) PZT-A
(Soft) PZT-B
σ_{zz}
ε_{zz}
P_z
Compressive Stress, $-\sigma_{zz}$(MPa)
Axial Strain, $-\varepsilon_{zz}$(%)
500
400
300
200
100
0
0
0.2
0.4
0.6
0.8

Fig 8

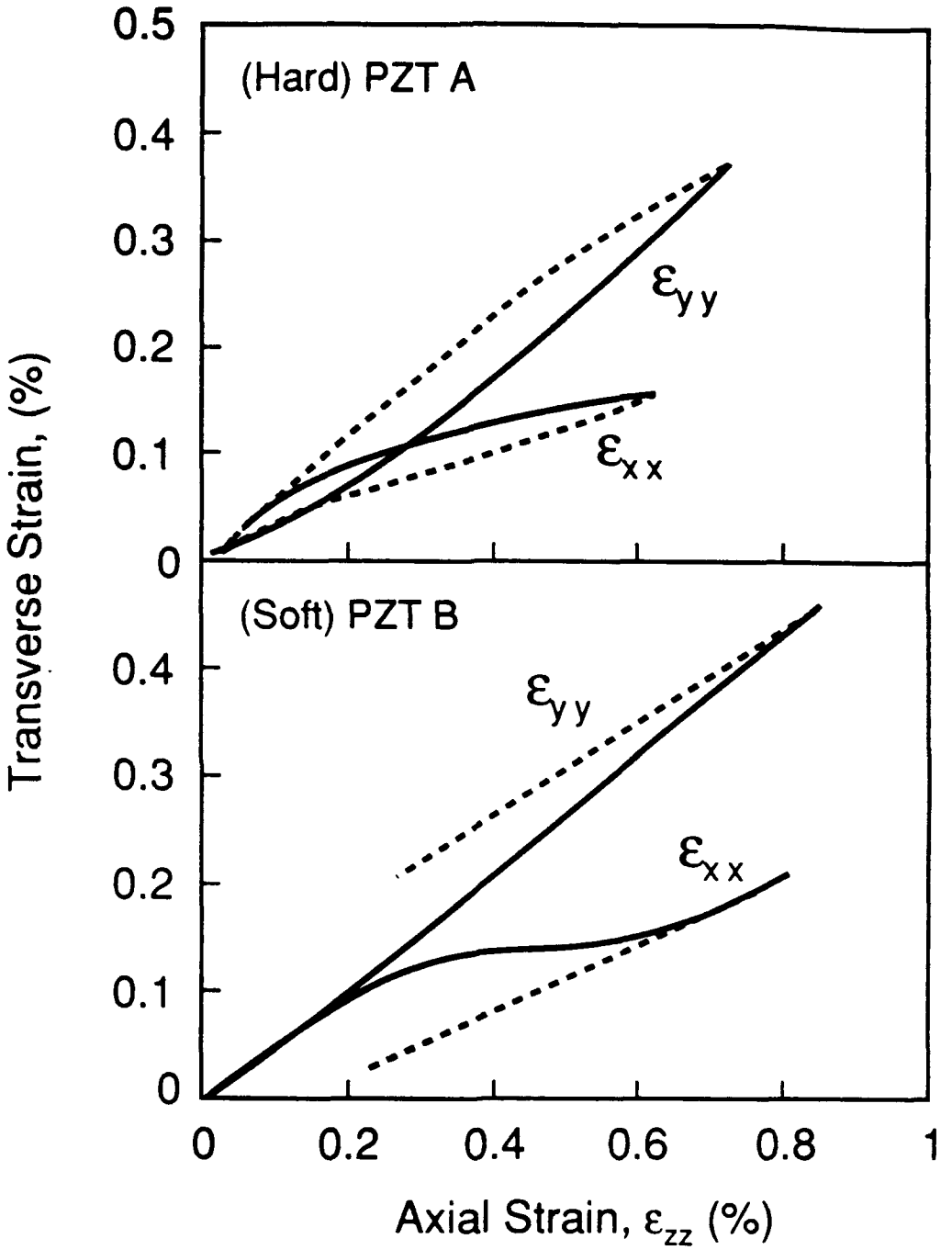
(Hard) PZT A
(Soft) PZT B
ε_{yy}
ε_{xx}
Transverse Strain, (%)
Axial Strain, ε_{zz} (%)
0.5
0.4
0.3
0.2
0.1
0
0.2
0.4
0.6
0.8
1

Fig 7

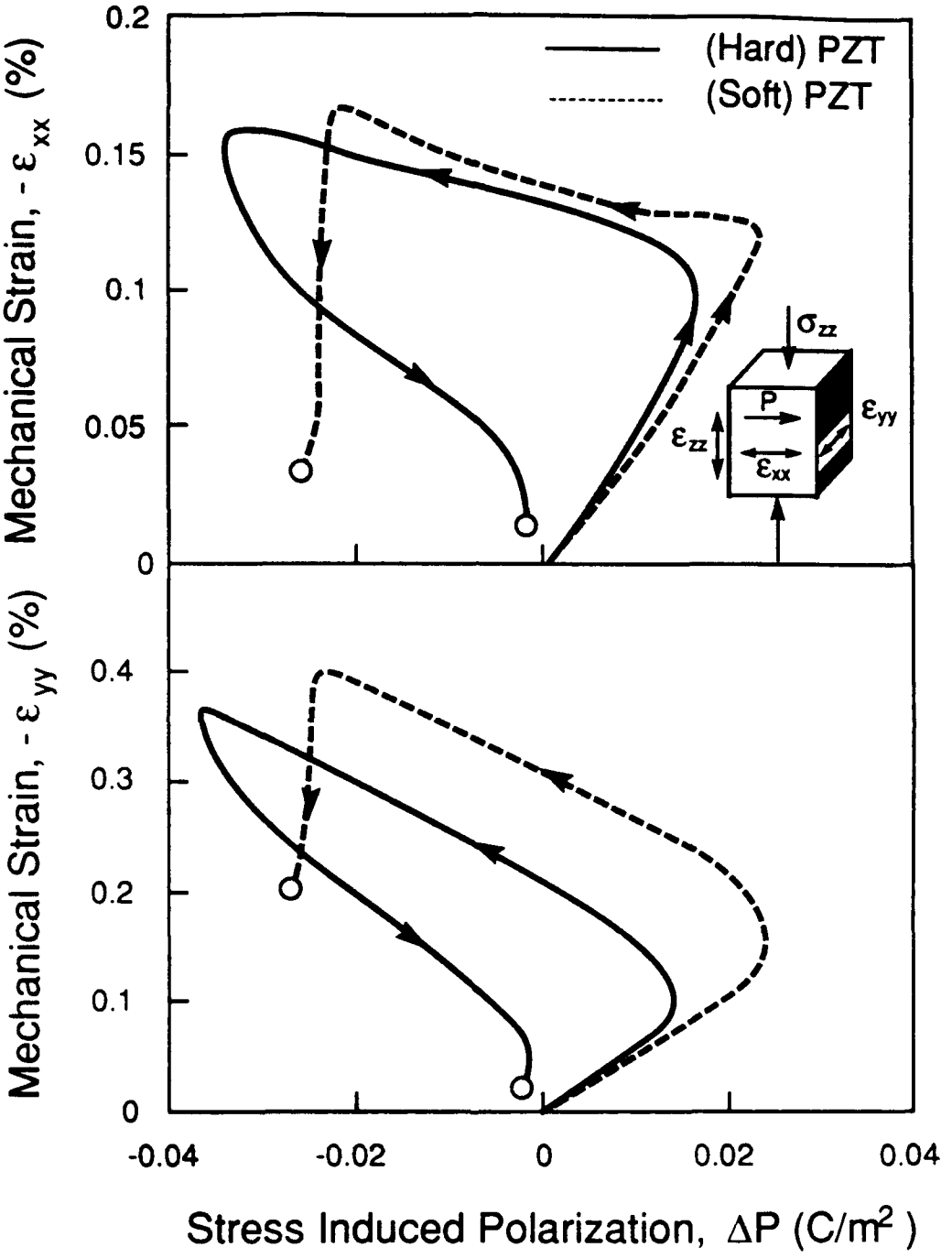
(Hard) PZT
(Soft) PZT
Mechanical Strain, - ε_{xx} (%)
Mechanical Strain, - ε_{yy} (%)
0.2
0.15
0.1
0.05
0
0.4
0.3
0.2
0.1
0
-0.04
-0.02
0
0.02
0.04
σ_{zz}
P
ε_{zz}
ε_{xx}
ε_{yy}
Stress Induced Polarization, ΔP (C/m^2)

Fig 10

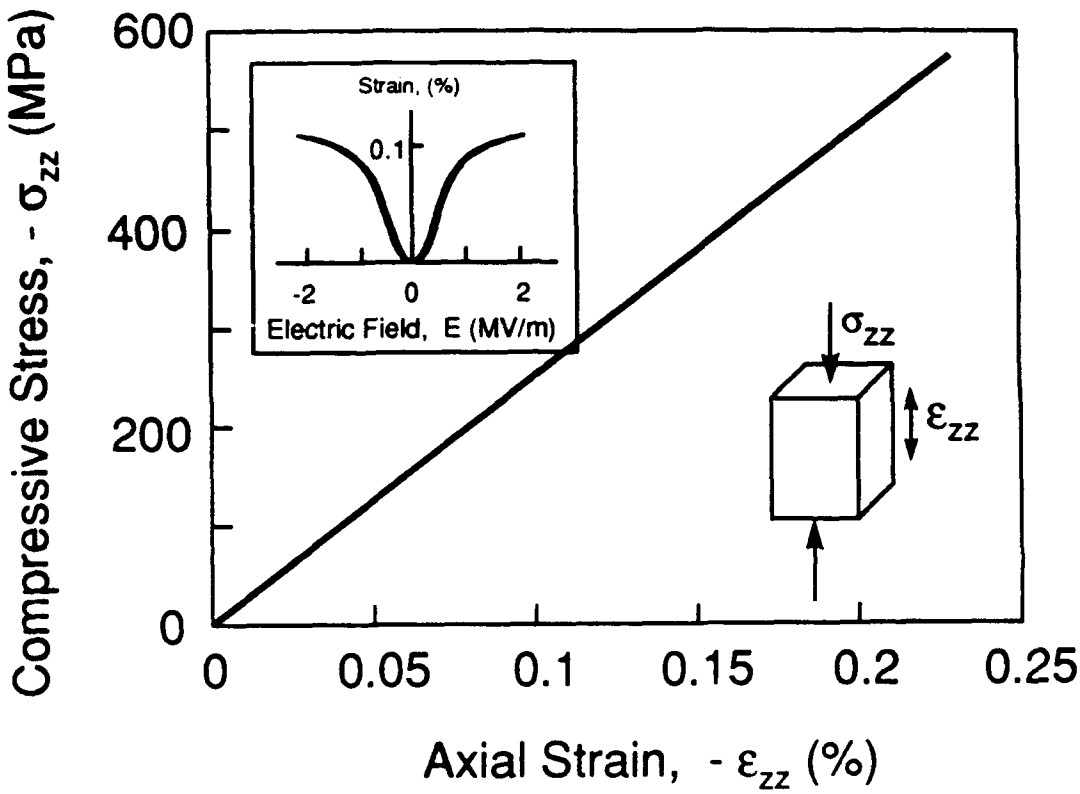
Compressive Stress, - σ_{zz} (MPa)
600
400
200
0
0
0.05
0.1
0.15
0.2
0.25
Axial Strain, - ε_{zz} (%)
Strain, (%)
0.1
-2
0
2
Electric Field, E (MV/m)
σ_{zz}
ε_{zz}

Fig 11

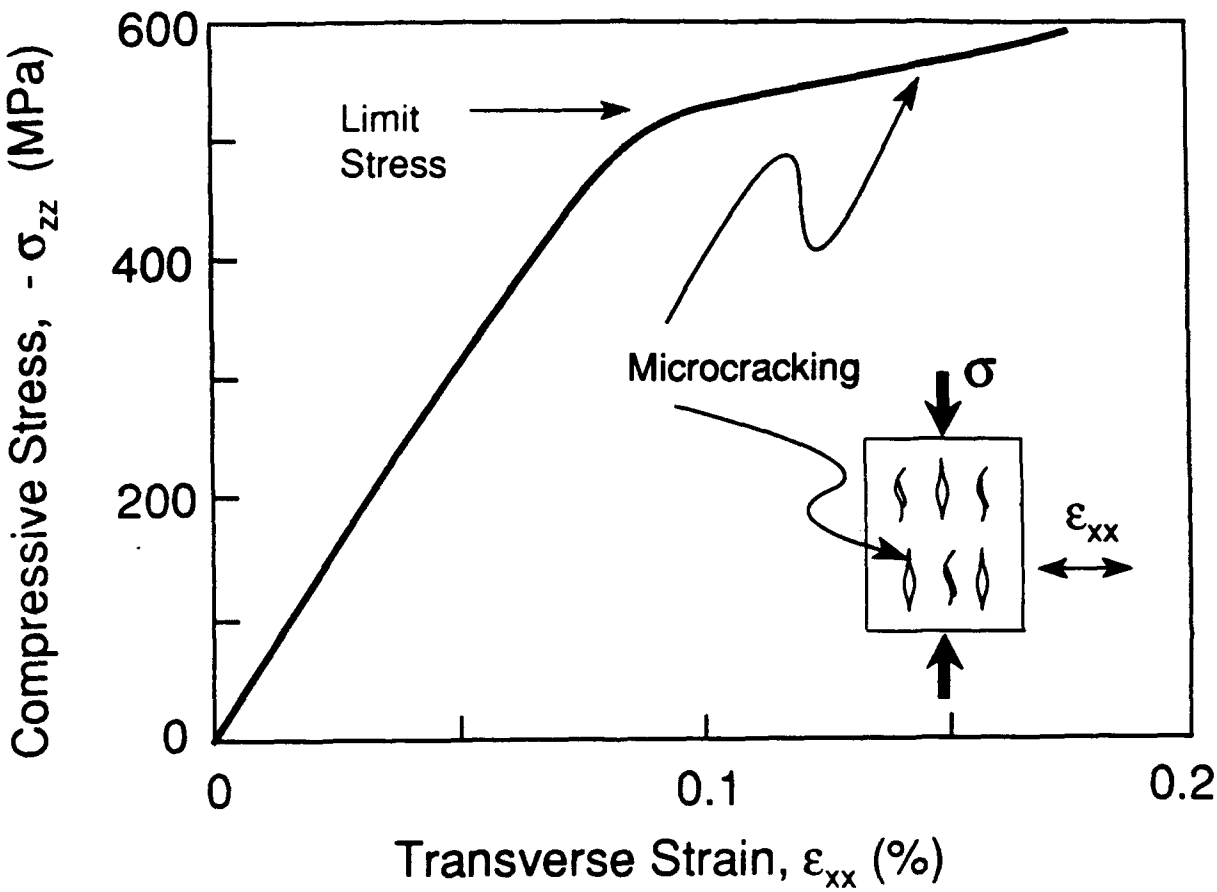

Cao.DC-3/92-amk-D4#657-9 (FIG. 13)

Fig. 12 (a)

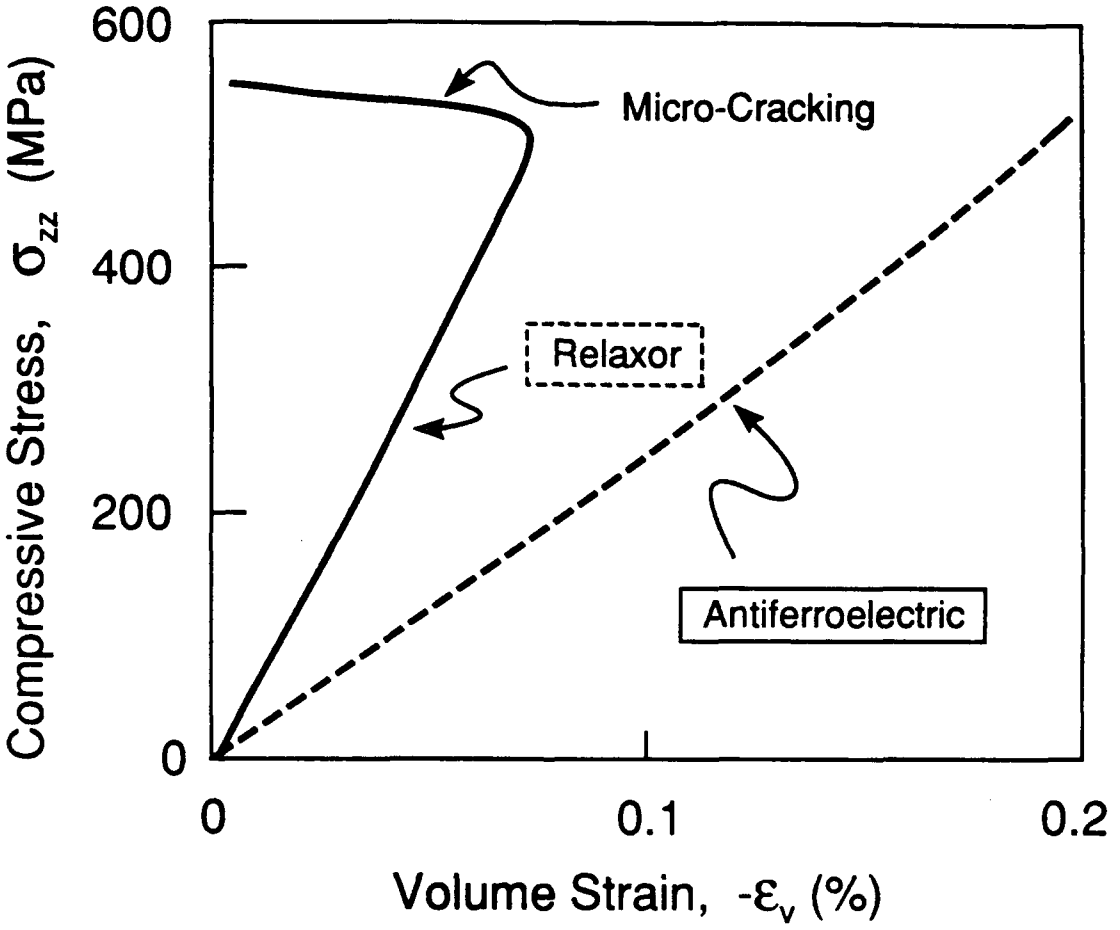
600
400
200
0
Compressive Stress, σ_{zz} (MPa)
Micro-Cracking
Relaxor
Antiferroelectric
0
0.1
0.2
Volume Strain, $-\varepsilon_v$ (%)

Fig. 12 (b)

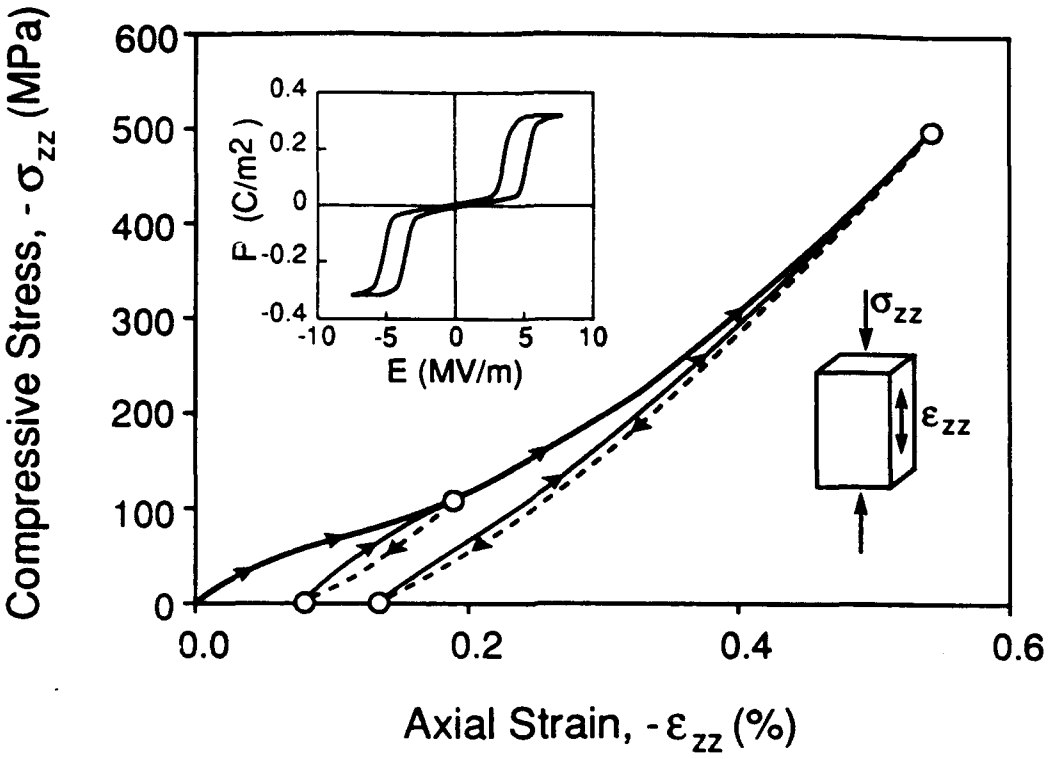
Compressive Stress, - σ_{zz} (MPa)
600
500
400
300
200
100
0
0.0
0.2
0.4
0.6
Axial Strain, - ε_{zz} (%)
P (C/m2)
0.4
0.2
0
-0.2
-0.4
-10
-5
0
5
10
E (MV/m)
σ_{zz}
ε_{zz}

Fig. 13

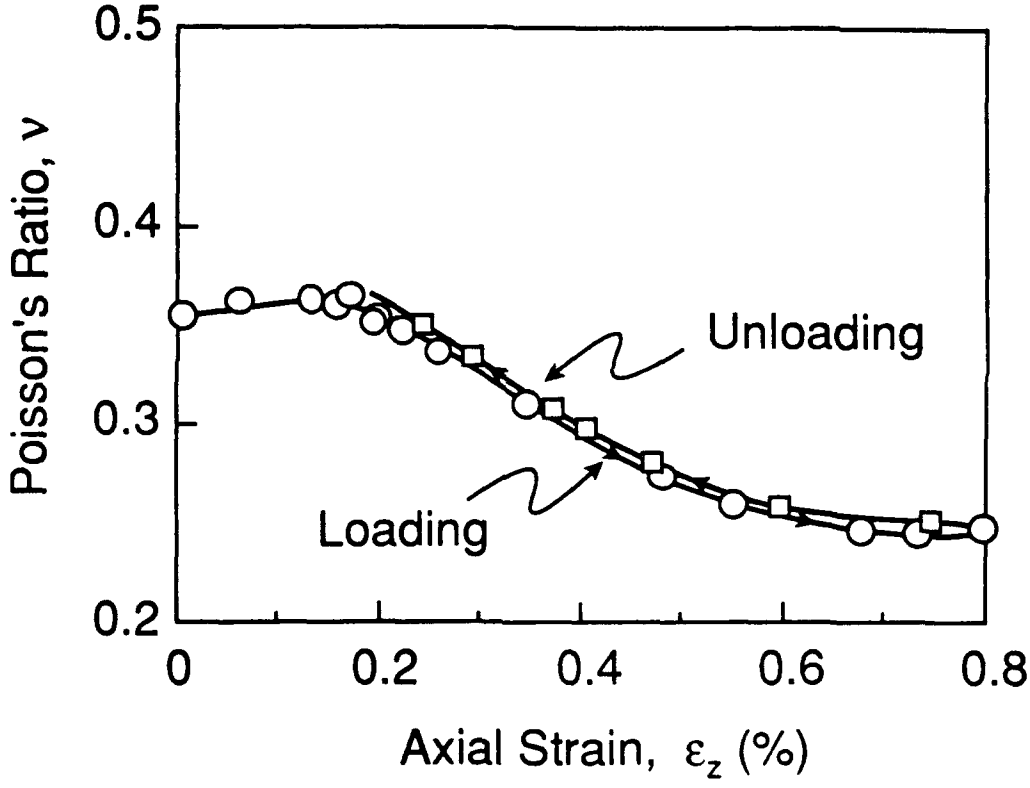
0.5
0.4
0.3
0.2
Poisson's Ratio, ν
Unloading
Loading
0
0.2
0.4
0.6
0.8
Axial Strain, ε_z (%)

Fig. 14

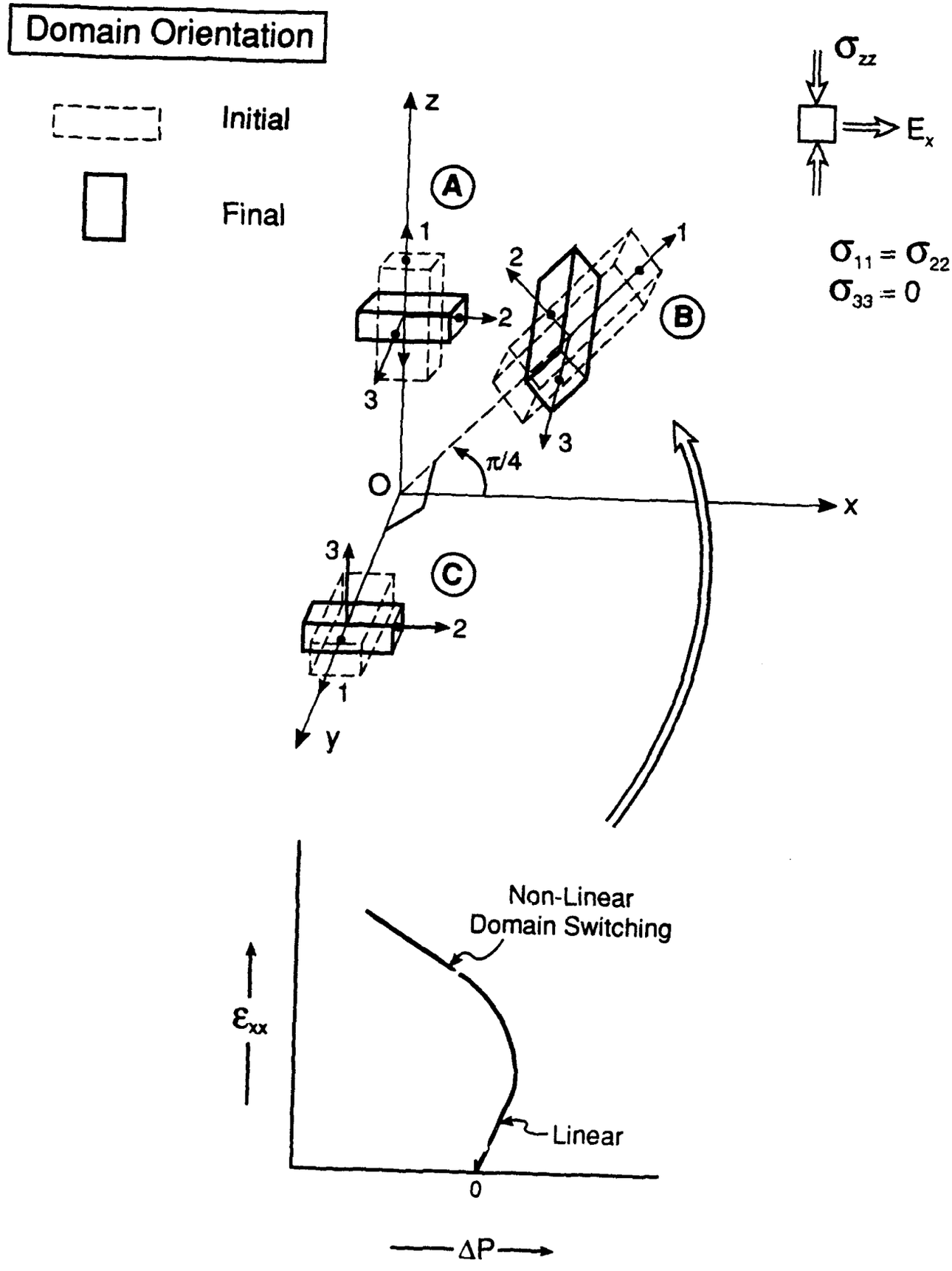

Cao.Evans.URI+11/91+amk+044675-1

Fig 15

MATERIALS

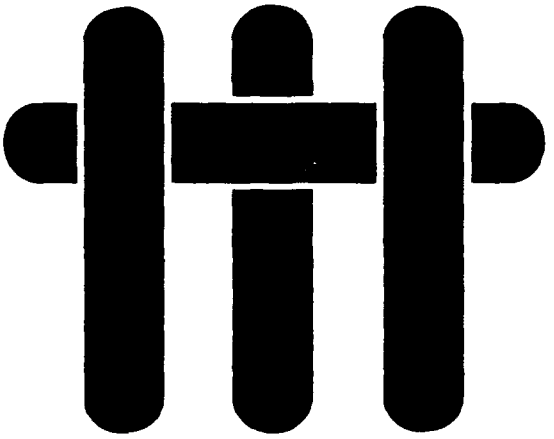

THE STRUCTURE AND PROPERTIES OF A FERROELECTRIC/ELECTRODE INTERFACE

by

H. C. Cao, M. De Graef and A. G. Evans
Materials Department
College of Engineering
University of California
Santa Barbara, California 93106–5050

Submitted to J. Am Ceram Soc.

KJS-Evans-5•S•TA-Str Prp 91/07/09•4:19 PM•5/21/92

Abstract

In advanced actuator systems, ferroelectric ceramics are usually made into multilayered stacks to obtain optimum performance. This is done by interlacing noble metals (such as Pt) with ceramic green sheet and cofiring. The present study proposes an alternative, more economic electrode. Copper has been successfully bonded to several PZT-based ferroelectric ceramics in a multilayer configuration by diffusion bonding. The microstructure and the relevant physical properties of the interfaces have been investigated using microscopy as well as mechanical and electrical characterizations. These studies indicate that no reaction product forms at the interface and, furthermore, the interface exhibits high resistance to decohesion, making Cu a promising alternative electrode material.

1. INTRODUCTION

The application of ferroelectric ceramics as actuators and sensors is reliant on multilayer concepts, wherein electrodes alternate with the ferroelectric.[1,2] While the electrodes are often regarded as being secondary to the actuator/sensor system, the ultimate performance of the system is strongly influenced by the electrical and mechanical characteristics of the electrode itself and, usually, the electrode/ ferroelectric interface.[3] The interfacial zone has particular ramifications on performance, through a multiplicity of potential degradation effects: fatigue, decohesion and charge injection. There has been minimal basic research on interfaces between metals and complex oxides (other than binary systems, Al_2O_3, NiO, etc.)[4]. Consequently, there are no rules on such issues as reaction products, decohesion, interface resistance, etc. Furthermore, there have been few systematic studies of ferroelectric/electrode interfaces and, as yet, there are no scientific governing principles.

Common electrode systems for PZT sensors and $BaTi0_3$ capacitors are typically noble metals (such as Pt and Ag). These materials are expensive and may be susceptible to degradation effects[5], such as debonding. Furthermore, Ag is subject to migration effects that lead to premature breakdown. Consequently, a Pd/Pt alloy, that is apparently resistant to migration, is often used for cofired multilayer actuators. The present article represents an initial attempt at studying a rational interface between a ferroelectric and an *inexpensive* metal, with implications for multilayer systems.

For this purpose, bonds consisting of alternate layers of Cu and two ferroelectric ceramics have been produced by diffusion bonding. The microstructure of the interface has been characterized using a combination of electron microscopy techniques. The interfacial mechanical properties have also been assessed, using an

indentation technique. Furthermore, the Polarization/Field (P/E) behavior has been characterized in order to validate that Cu can be used as an economic alternative electrode, without adverse effects on the ferroelectric and electromechanical response.

2. EXPERIMENTAL

2.1 Materials

The oxide ferroelectrics used for this study include a hard PZT† and an antiferroelectric PLSnZT, with a chemical composition $Pb_{.97}La_{.02}(Zr_{.66}Ti_{.11}Sn_{.23})O_3$. Thin plates having dimensions 5 x 8 mm and 2 mm thickness were cut from bulk sintered material and ground using a resin-bonded diamond wheel to minimize machining damage. High purity (99.98%) Cu foil, 25 μm in thickness, was interspersed to form a multilayer (Fig. 1). Bonding was conducted in a vacuum at 1050°C for 10 hrs. A small pressure of about 5 MPa was maintained throughout. Under these conditions, lead loss is minimal. A slow cooling rate of about 3°C/min was used to alleviate residual stress. The bonded specimen was sectioned normal to the interface and polished.

2.2 Characterization

Thin sections for transmission electron microscopy (TEM) were prepared using the off-center dimpling technique discussed elsewhere.[6] Discs, 3 mm in diameter, with the interface region about 0.5 mm from the center of the dimple were ion-milled at 4 kV, 15° beam angle. Semi-circular quartz shields were used to protect one side of the interface from the ion beams. The resulting samples showed a large hole adjacent to the interface in the ceramic (about 0.8 mm diameter) with interface

† PZT C5500, Chanel Industries , Inc. Goleta, California

regions sufficiently thin for TEM observations at 400 kV. Electron diffraction measurements, energy dispersive X-ray analysis (EDS), high resolution imaging (HREM) and parallel electron energy loss spectroscopic measurements (PEELS) were all carried out on a JOEL 4000 FX side entry microscope.

Bonded samples with Cu electrodes were incorporated into a *Sawyer-Tower* circuit to measure the polarization (P/E) behavior. For comparison, the P-E curves of the ferroelectrics were also measured by using thin slice samples with sputtered *gold* electrodes. The capacitance of the multilayer was measured by an LRC meter. Dielectric breakdown measurements were also performed, by applying a high DC voltage across the specimen.

2.3 Indentation

The fracture resistance of the interface between the metal electrode and the ferroelectric was assessed using an indentation technique. A Vicker's indent was emplaced into the ceramic, adjacent to the interface, aligned such that one radial crack had normal incidence with the interface (Fig. 2). Indentation loads between 5 and 30N were used. The consequent deformation of the metal and slip along the interface, as well as the occurrence of interface decohesion, were inspected in a scanning electron microscope, after the specimen had been coated with gold by plasma sputtering.

3. RESULTS

3.1 Interface Structure

i) Cu / PLSnZT

A low magnification TEM view of Cu / PLSnZT (Fig. 3a) indicates a relatively planar interface. Faceted regions were identified at several locations (Fig. 3b). Diffraction and EDS established that these regions were pure Cu, with no evident

interdiffusion with the ferroelectric. The Cu grain size was substantially larger than the ferroelectric grain size. PEELS measurements confirmed the absence of O in the Cu layer, although in some Cu grains close to the interface, a weak N-edge was visible. Observations at high magnification were unable to identify a discrete Cu oxide layer at the interface, but revealed the presence of ZrO_2 precipitates (Fig. 4a, arrowed regions, and b). The shape of the precipitate suggests a cubic crystal structure. The composition of the precipitate was established by means of combined EDS and PEELS analysis. The average precipitate size was about 50 nm and all particles were observed to protrude into the metal layer.

Electron diffraction analysis of the ferroelectric perovskite [001] and [110] zone axis orientations[7,8] revealed the presence of a long period superlattice modulation of an (as yet) undetermined origin. A complete structure determination of this phase by means of electron, X-ray and neutron diffraction is currently underway. High defect concentrations (dislocations and domain walls) were observed in the *ferroelectric* close to the interface (Fig. 4a).

ii) Cu / PZT

The interface in the cross-section Cu / PZT samples is not as planar as that in the Cu / PLSnZT samples (Fig. 5a). EDS analysis of the metal again revealed no interdiffusion of cations from the ferroelectric into the Cu. Several precipitates occur along the interface having sizes in the range 40 to 100 nm. Electron diffraction analysis combined with EDS identified these particles as cubic zirconia. Again, a high defect concentration was observed in the *ferroelectric* close to the interface, consisting of both the dislocations and domain cells (Fig. 5b). The domain walls are identified by the fringe contrast with features being asymmetric in bright field and symmetric in dark field imaging mode. In addition, well-developed domains were present in all ferroelectric grains.

3.2 Measurements

Capacitance measurements, performed on the multilayer, gave values for the dielectric constants, K = 1460. This value is identical to that measured on the material with sputtered-gold electrodes, prior to diffusion bonding. It also coincides with the value quoted by the manufacturer [9]. The ferroelectric hysteresis loop, and the dielectric strength measured on the bonded trilayer system, were also identical to values obtained before bonding.

Cracks introduced within the ferroelectric by indentation that extend to the electrode interface are invariably arrested at that interface (Fig. 6).There is no evidence of interface debonding. Furthermore, the plastic zone developed in Cu is similar to those developed in an Al/Alumina system[10]: a well-characterized strong interface between a metal and an oxide. Typically, the cracks blunt at the interface, indicative of a 'strong' bond and extensive yielding in the metal. Such strong interface bonding has also been noted between Cu and certain binary oxides.[5]

4. ANALYSIS

Creation of a thin foil section in preparing the TEM samples introduces surfaces that act as edge sites, which concentrate the thermal expansion mismatch stress[11]. Yielding occurs from this edge if the equivalent stress, σ_e, exceeds the yield strength of either constituent material. Dimensional arguments suggest that the foil thickness, t, relative to the thickness of the Cu layer, h, controls plastic zone evolution, as thinning proceeds (Fig. 7a). Consequently, two typical t/h ratios are analyzed: 1 and 0.1. The latter represents a limiting case, wherein the bond can be regarded as a bi-material interface separating semi-infinite Cu and ferroelectric materials.

A finite element procedure (ABAQUS) has been used to analyze the plastic strain contours at the interface. The elastic-plastic behavior, assumed for Cu, is governed by a von Mises yield condition, with power law hardening (Table I). For the ferroelectric material, a two-term power law is used to model the ferroelectric deformation, associated with domain switching under stress [12]. Constitutive parameters used for this calculation are summarized in Table I. Geometric symmetry allows the calculations to be performed using a quarter of the cross-section(Fig. 7). The plastic strain contours are computed (for both t/h configurations), as the specimen is cooled from the processing temperature. It is assumed that creep relaxation occurs at high temperatures, such that residual stresses do not begin to develop above $T \approx 0.7\ T_m$, with T_m being the melting point of the copper. The results (Fig. 8) indicate a relatively small effect of t/h. In both cases, there is a much larger plastic zone in the ferroelectric than in the Cu. The plastic strain in the PZT near the interface approaches 0.6% (the permanent saturation strain exhibited by PZT [12]). The features exhibited by the plastic zone are consistent witn the high dislocation density and the domain wall configurations observed by TEM (Fig. 4, 5).

5. Concluding Remarks

Two of the present observations indicate that Cu has desirable characteristics as an electrode for a ferroelectric, multilayer actuator. i) There are no reaction products at temperatures needed for diffusion bonding, (except for occasional, small precipitates of ZrO_2). ii) The interface is strongly bonded and resistant to decohesion.

A possible detriment is the occurrence of plastic deformation in the ferroelectric, near the interface. Such deformation is an edge effect, associated with

the thermal expansion mismatch, and arises because of the low 'yield strength' of the ferroelectric. The concern is that superposed effects of electric field, during operation, may result in fatigue damage that spreads from the edge[13]. Further study is deemed necessary to elucidate this effect.

Acknowledgements

The antiferroelectric material was provided by Dr. Wuyi Pan at the New Mexico Tech. Funding for this research is partially provided by the Office of Naval Research, under the contract #N00014-91-J-4024.

Table I Contitutive Properties of the Cu / PZT System

Material	Cu	PZT
Young's modulus, E(GPa)	130	80
Poisson's ratio, ν	0.343	0.4
Thermal expansion coefficient, α ($10^{-6}K^{-1}$)	16.6	1.8 (T>Tc) 9.0 (T<Tc)
Yield strength, σ_o (MPa)	60	
Hardening exponent, n¶	0.32	
Reference stress, σ'_o (MPa)§		75
Reference strain, ε'_o §		0.65
Exponent a §		0.7
Exponent b §		12

¶ The power hardening law [14] for Cu relates the true stress, σ, with the true plastic strain, ε;

$$\sigma = \sigma_o(\varepsilon / \varepsilon_o)^n$$

§ The two-term power law for PZT satisfies the following expression [12];

$$\sigma'/\sigma'_o = (\varepsilon'/\varepsilon'_o)^a + (\varepsilon'/\varepsilon'_o)^b$$

where σ' and ε' are the deviatoric stress and plastic strain , respectively.

REFERENCES

[1] S.R. Winzer, N. Shanker and A.P. Ritter, "Designing Cofired Multilayered Electrostrictive Actuators For Reliability," *J. Am. Ceram. Soc.*, **72**, 2246–57 (1990).

[2] L. E. Cross, "Piezoelectric and Electrostrictive Sensors and Actuators for Adaptive Structures and Smart Materials." ONR Annual Repart, Penn. State University, (1990).

[3] W.J. Menz and R. Anderson, AT&T Bell Laboratory Report. (1978).

[4] I.E. Reimanis, B. J. Dalgleish and A.G. Evans, "The Fracture Resistance of A Model Metal/Ceramic Interface," Acta metall. **39**, 3133-3141, 1991.

[5] M. Rühle, A. G. Evans, M. F. Ashby and J. P. Hirth, Metal Ceramic Interfaces, Acta, Scripta Metallurgica Proc. Series, Vol. 4 (1990).

[6] M. De Graef, B.J. Dalgleish, M.R. Turner and A.G. Evans, "Interfaces Between Blumina and Platinum: Structure and Fracture Resistance," *Acta Metall. Mater.* in press, (1992).

[7] Y.-J. Chang, Y.-J. Lian and Y.-L. Wang, "One dimensional regular arrays of antiphase domain boundaries in anti-ferroelectric Sn-substituted lead zirconate titanate (PZT) ceramics," *Appl. Phys.*, **A36**, 221 (1985).

[8] M. De Graef, J. Speck, D.R. Clarke and D. Dimos, "Electron microscopy study of domain boundaries in relaxor ferroelectrics," submitted to Symposium I, *Ferroelectric Thin Films*, Materials Research Society Fall Meeting (Boston 1991).

[9] Catalogue, Channel Industries, Inc.

[10] H. C. Cao, M. D. Thouless and A. G. Evans, "Residual Stresses and Cracking in Brittle Solids Boded with a Thin Ductile Layer." *Acta metall.* **36** [8], 2037-2046, (1988).

[11] H. C. Cao, "A Model for Crack Extension in Metal Reinforced Brittle Solids," Advanced Composites Materials, *Ceramic Transactions* (Ed. M. Sacks) Vol. **42**, pp. 485-492, (1991).

[12] H. C. Cao and A. G. Evans, "Nonlinear Deformation of Ferroelectric Ceramics." submitted to *J. Amer. Ceram. Soc.*, (1992).

[13] Q. Y. Jiang, L. E. Cross, et al, to be published.

[14] J. H. Hollomon, "Tensile Deformation," *Trans. AIME*, 162, p. 268, (1945).

FIGURE CAPTIONS

Fig. 1. Schematic showing the layout of Cu/PZT multilayered stack for diffusion bonding

Fig. 2. A schematic illustrates the indentation in a ferroelectric ceramic close to an interface and the associated plastic zone in the electrode.

Fig. 3. a) Low magnification TEM micrograph indicates a planar interface between Cu and PZT (arrows indicate locations of the interface).

b) Faceted Cu regions near the Cu/PLSnZT interface. Some precipitates can also be observed near the interface.

Fig. 4. a) 50 nm ZrO_2 precipitates (Arrowed) at the Cu/PLSnZT interface.

b) A cube-shaped ZrO_2 precipitate at the interface, protruding into the metal layer.

Fig. 5. a) Interface (arrowed) between Cu an d PZT. Ferroelectric domain walls are present in all grains.

b) High defect concentration in the PZT close to the interface.

Fig. 6. Indentation crack arrests at the electrode/ferroelectric interface and blunting takes place. No interface decohesion is observed (interfaces marked by arrows).

Fig. 7. Geometry of thin foils used for FEM analysis and a typical finite element mesh for t/h=1.

Fig. 8. Plastic strain contours in a Cu/PZT bond, caused by thermal mismatch straining: a) $t/h = 1$; b) $t/h = 0.1$.

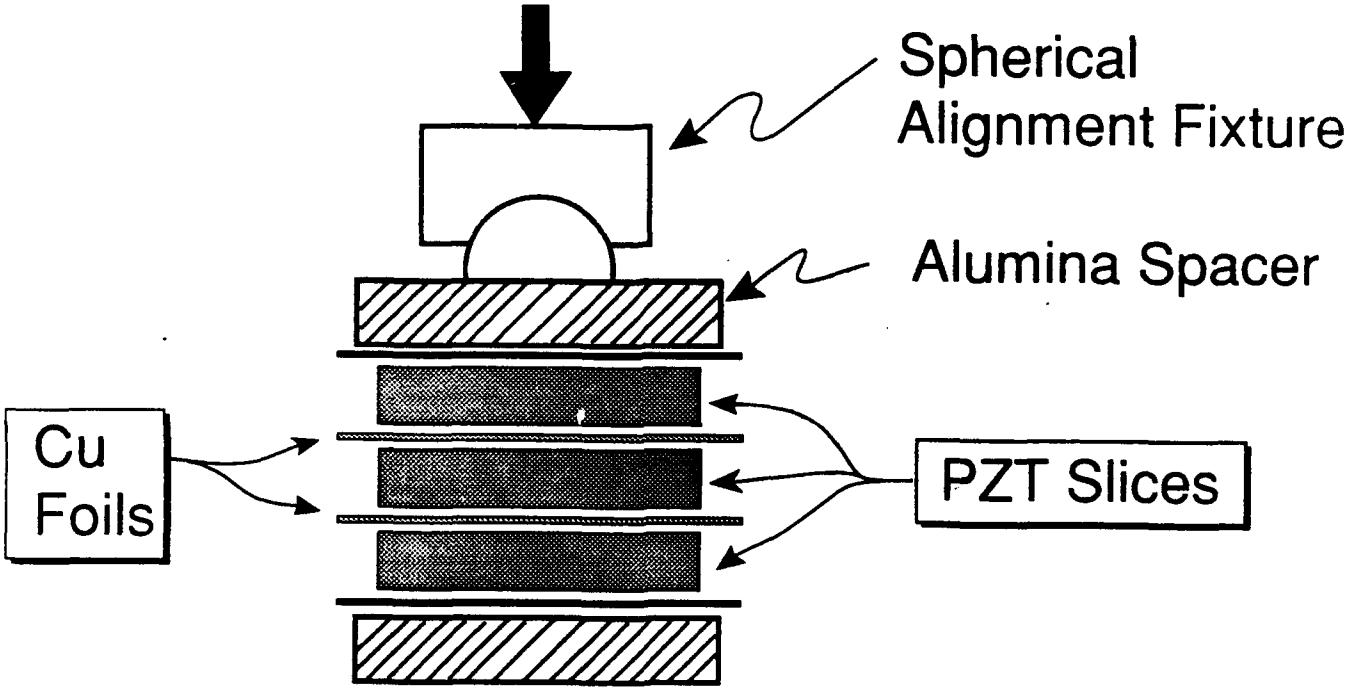
Spherical
Alignment Fixture
Alumina Spacer
Cu
Foils
PZT Slices

Fig. 1

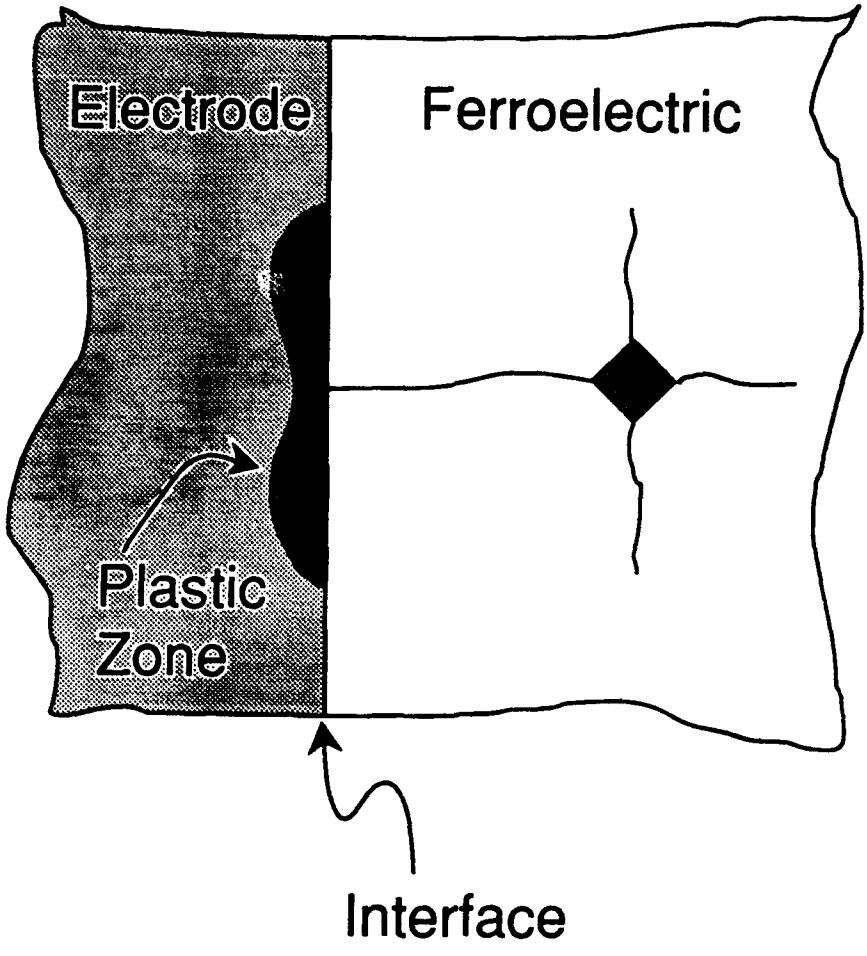

Fig. 2

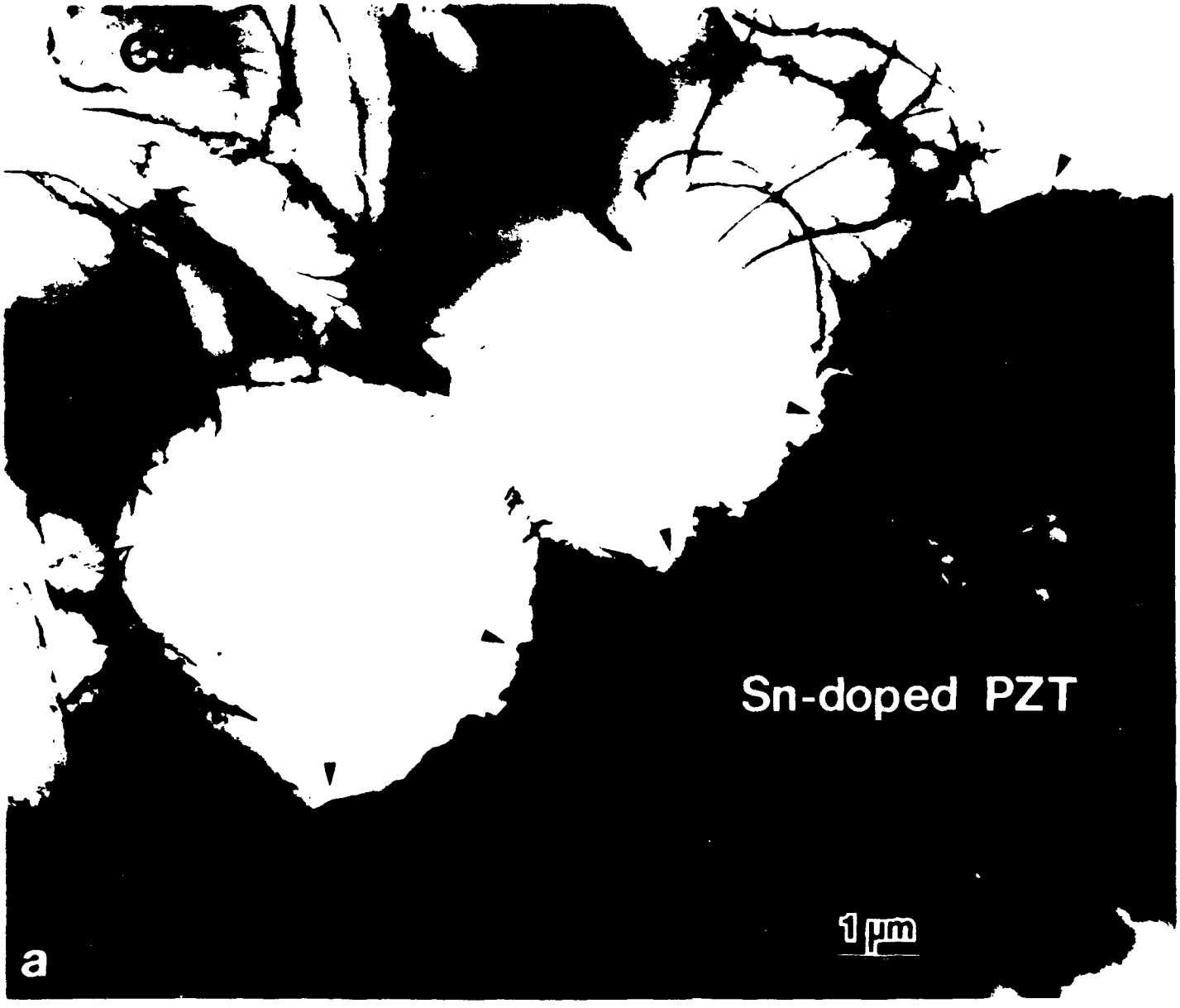

Fig. 3a

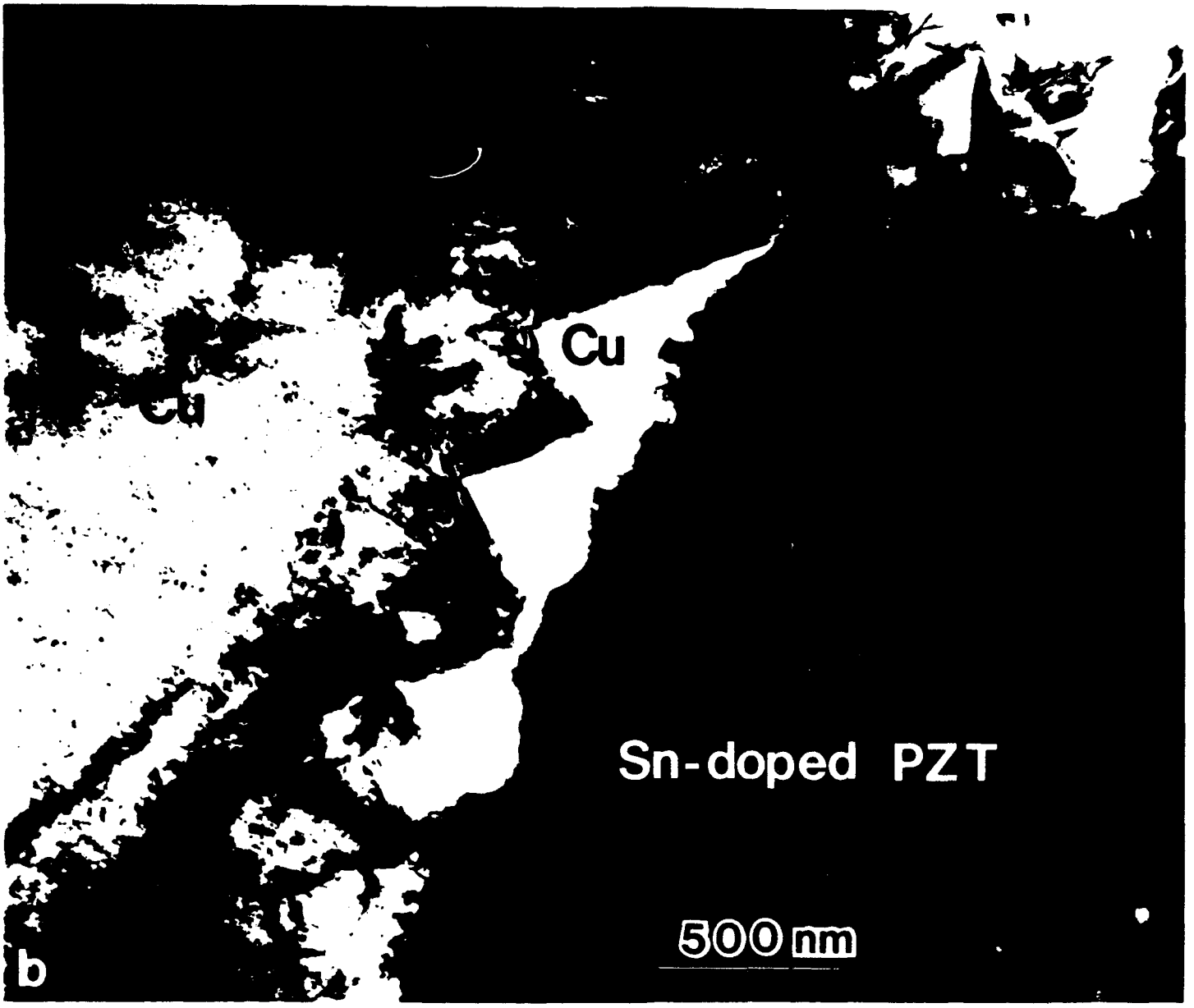

Fig. 3b

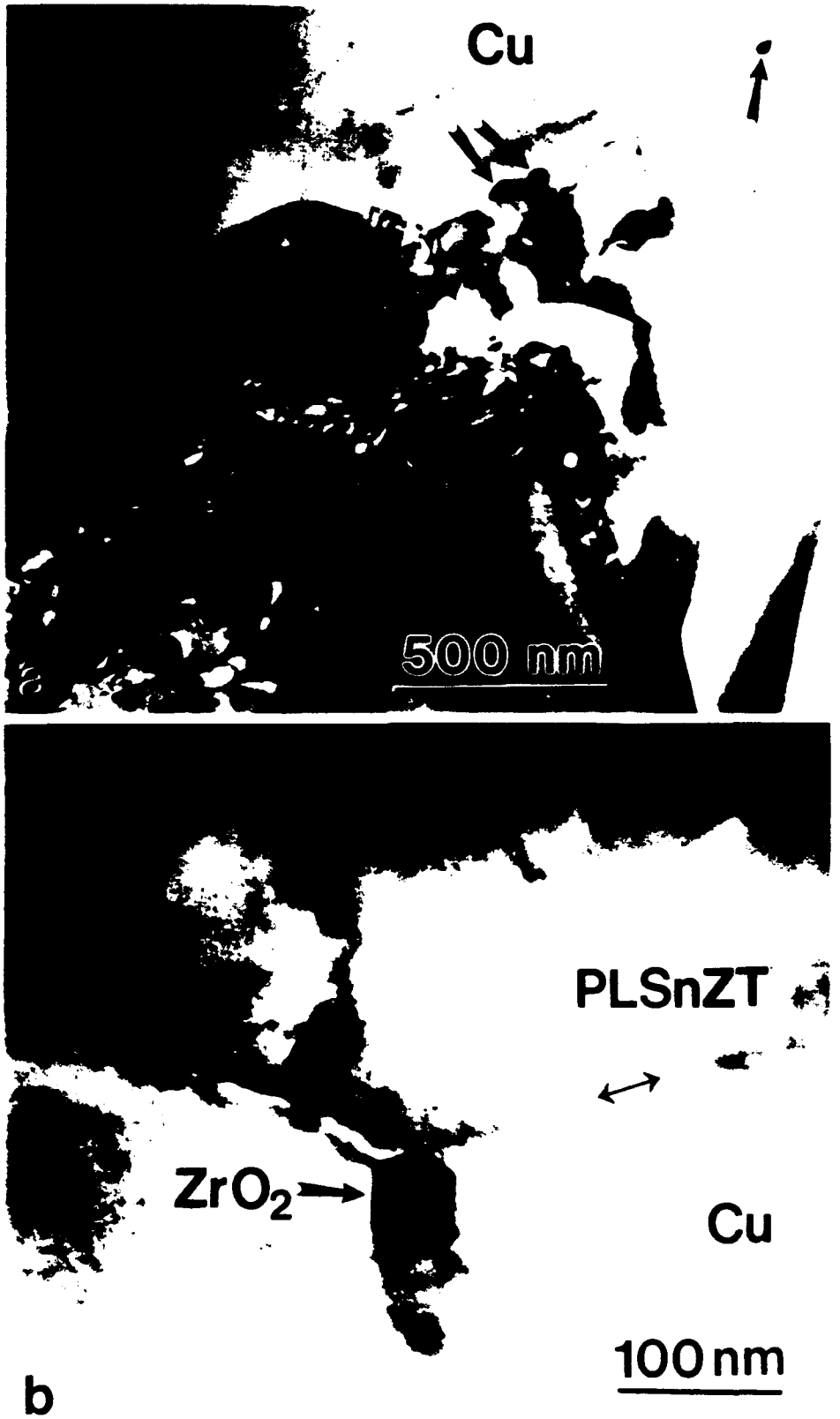

Fig. -

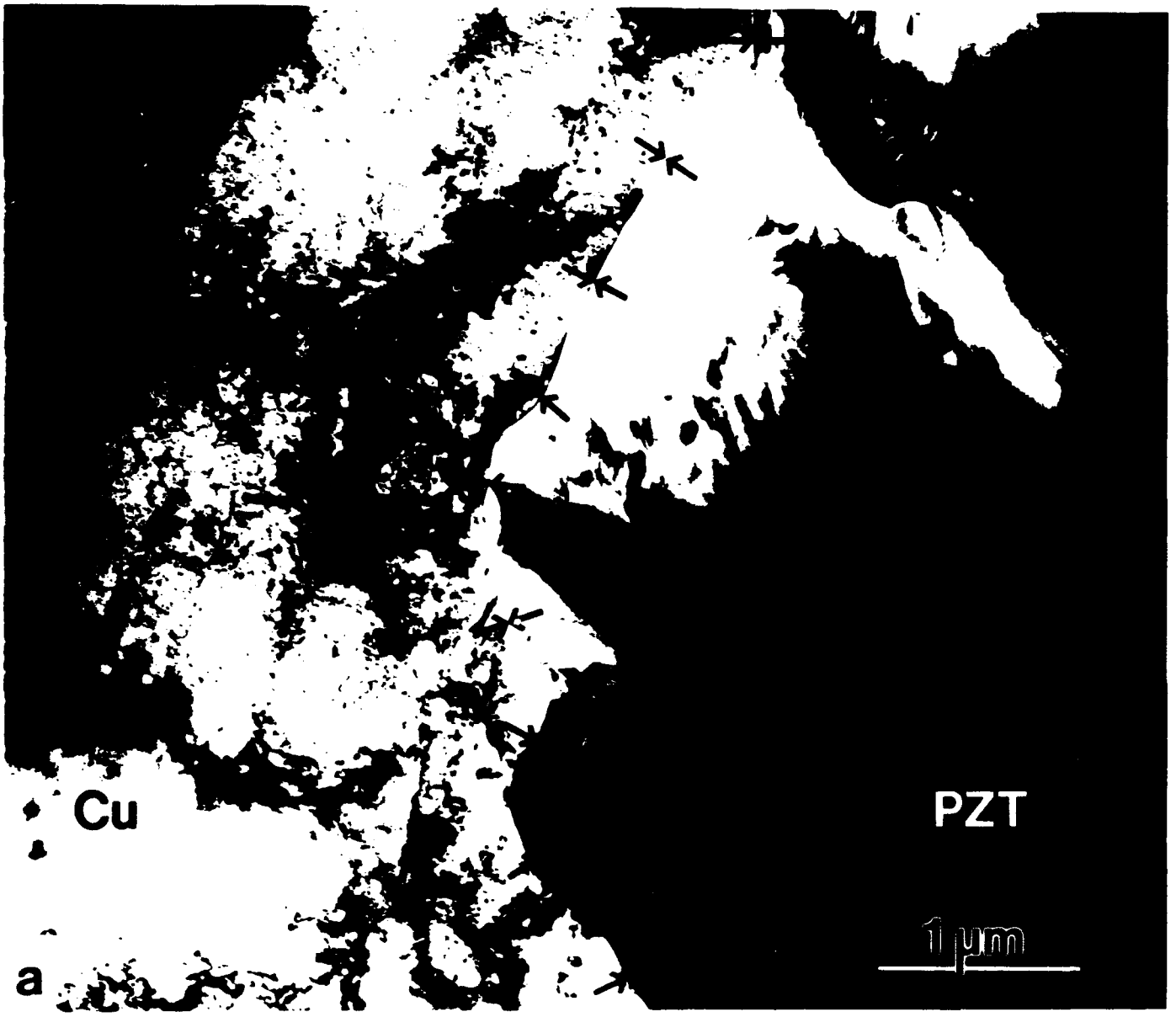

Fig. 5a

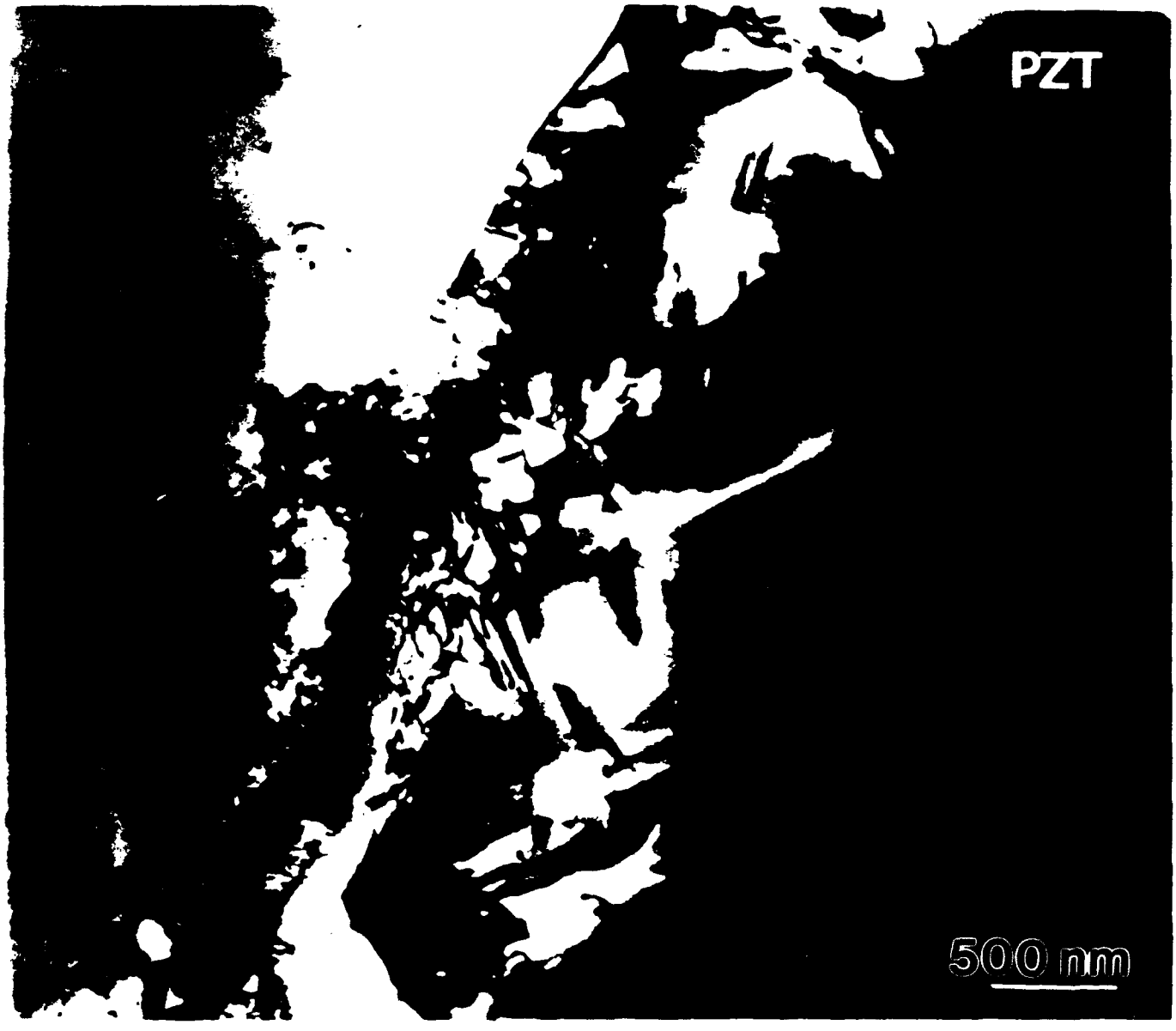

Fig. 5b

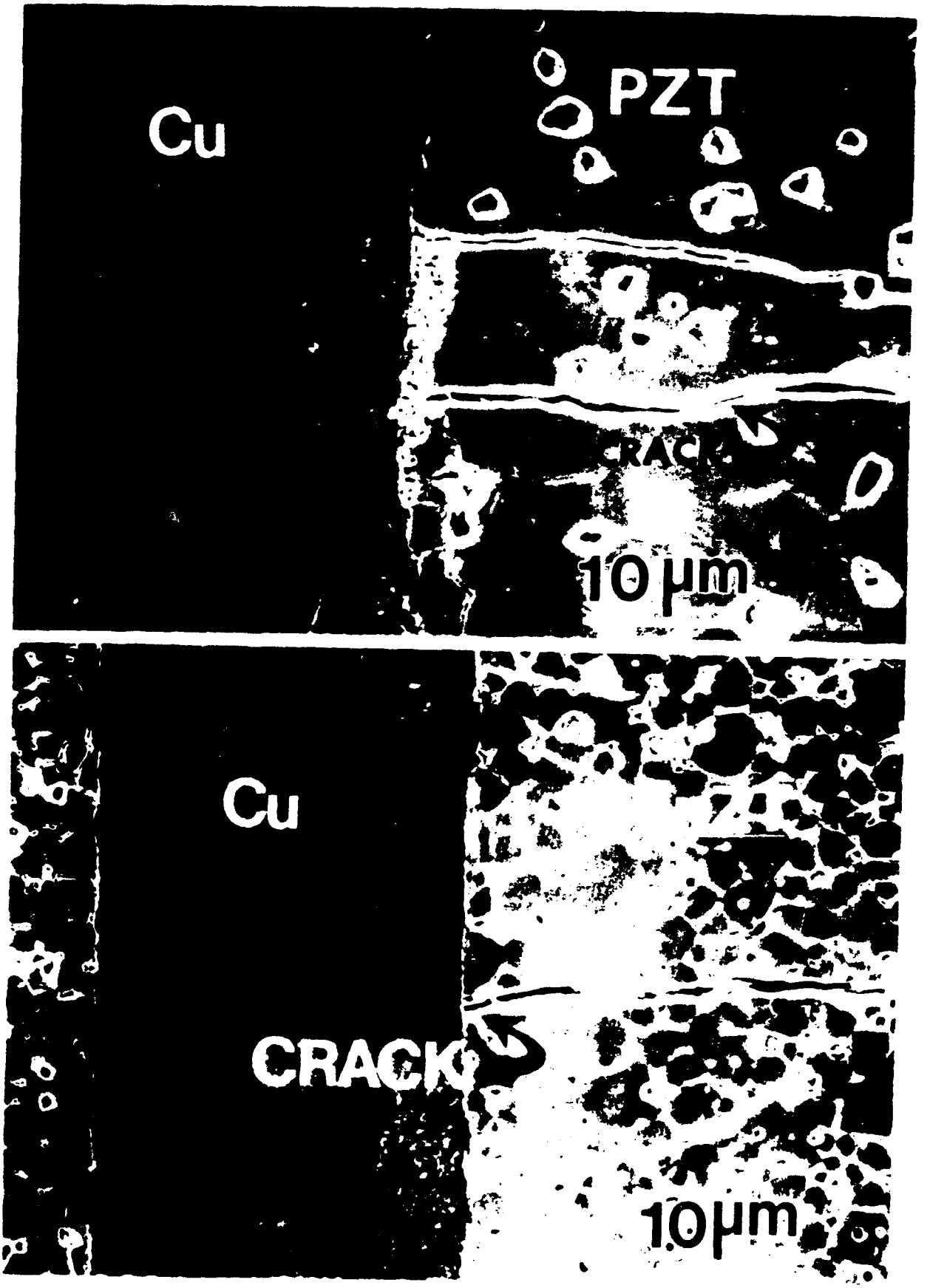
Cu
PZT
CRACK
10 μm
Cu
CRACK
10μm

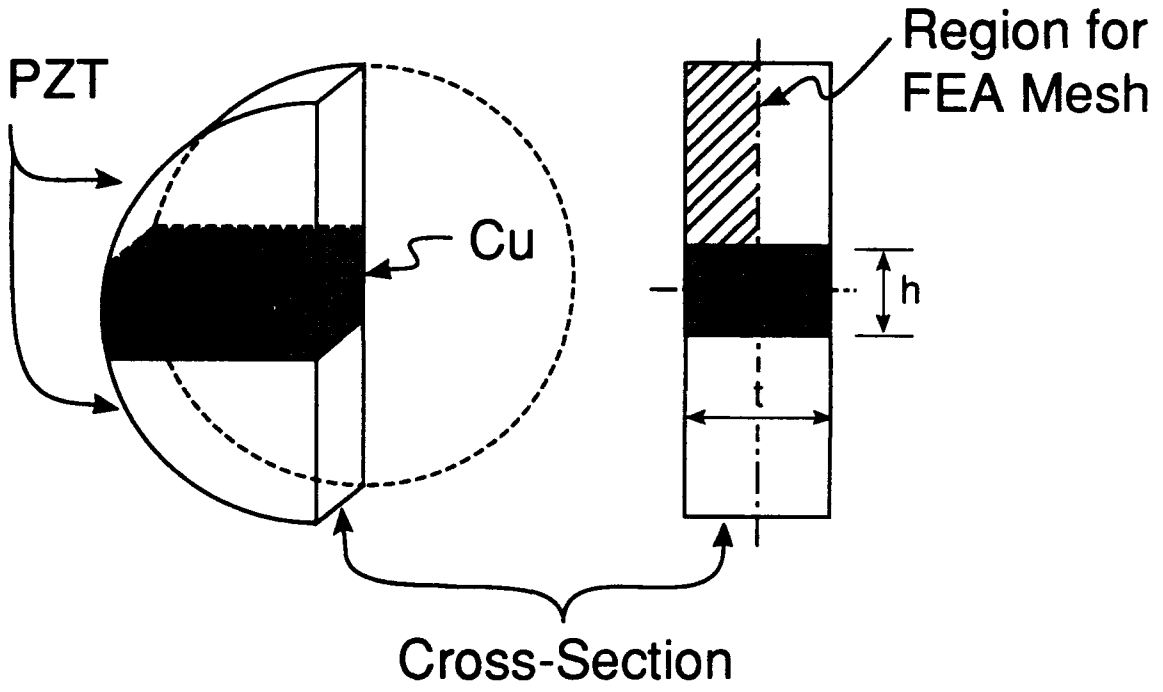

Fig. 7a

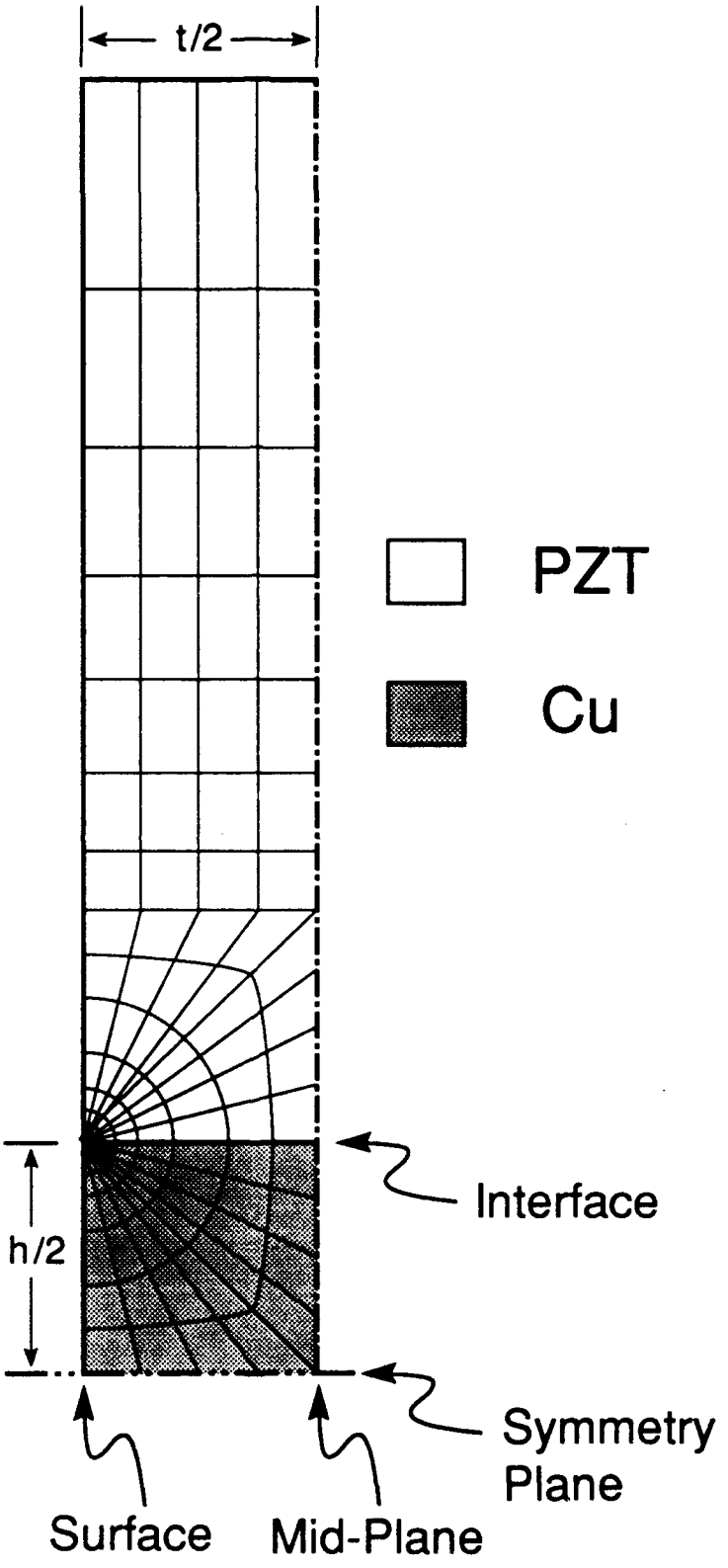

Fig. 7b

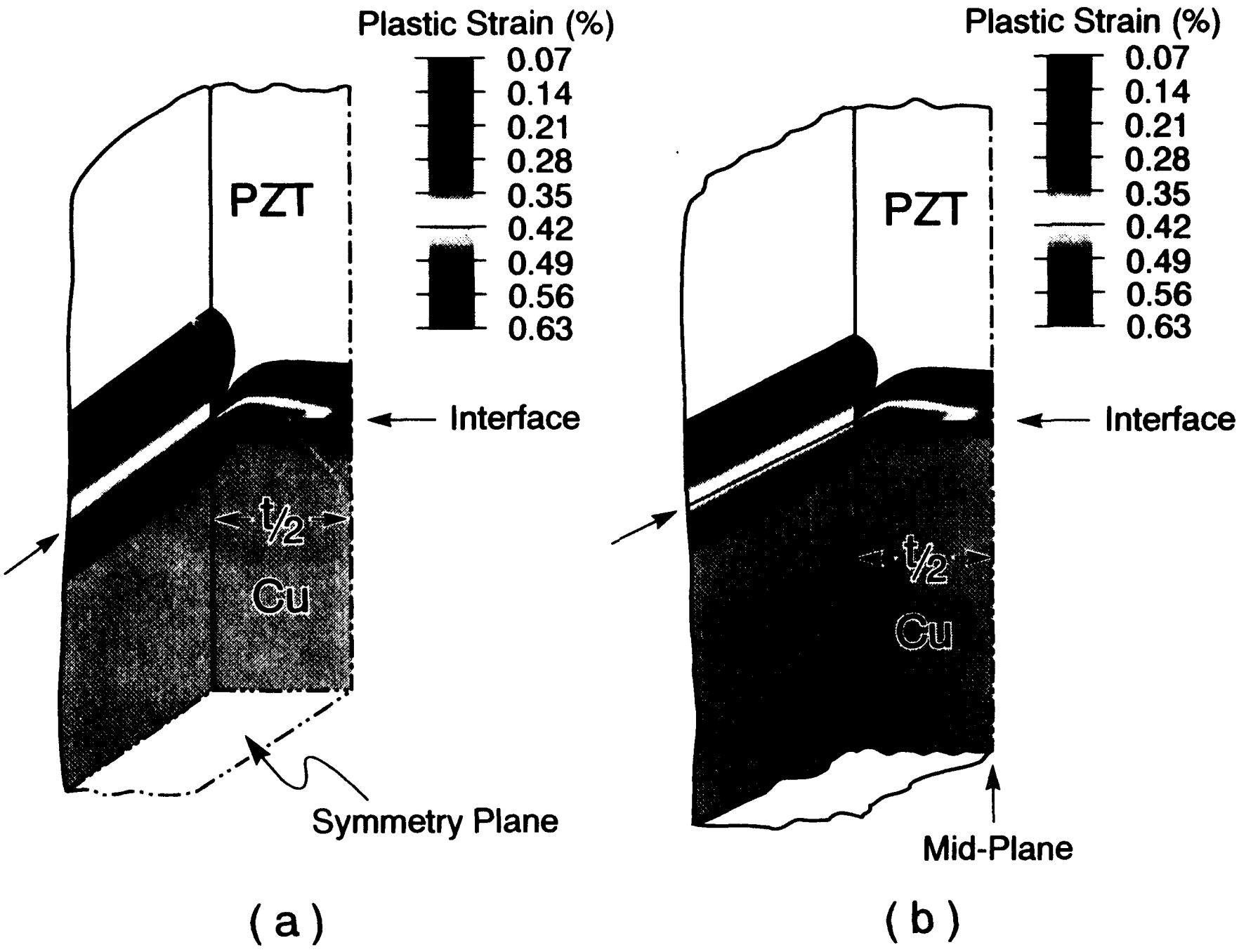

Cao DARPA-6/92-amk-D37#751-S

Fig. 8

Non-Linear Constitutive Properties of Piezoelectric Ceramics

H.C. Cao and A.G. Evans

Materials Department, University of California, Santa Barbara, California 93106

ABSTRACT

Experiments have been conducted to study the nonlinear constitutive properties of ferroelectric ceramics for large strain operation applications, where the mechanical behavior of the material dictates the overall electromechanical response of the devices. For this purpose, polarization and strain are measured continuously on a compression cuboid. Severe non-linear and hysteretic behavior is observed in these materials. An empirical formulation has been proposed to model the constitutive laws applicable to this non-linear deformation. Physical mechanism is provided , that is attributed to this constitutive law.

1. INTRODUCTION

Multilayer ferroelectric ceramics are used as actuators and sensors.[1,2] Many advanced applications require either large actuator displacements or large forces. Such conditions may cause non-linearity, as well as permanent deformation, of both the ferroelectric and the metal electrodes, leading to degradation of the performance of the actuator.[3-5] The non-linearities are most pronounced in the vicinity of stress concentrations that occur near edges[6] and in association with flaws.[7-8] The latter may be present either in the ferroelectric or at the ferroelectric/electrode interface. Consequently, it is essential to thoroughly characterize the constitutive behavior, before these materials can be successfully integrated into systems. Some of the procedures necessary for establishing the constitutive laws are developed in a series of studies.

Two of the most frequently used actuator/sensor configurations are addressed: multilayer and annular. Both designs have been used for piezoelectric actuators.[9] In the multilayer design, the stresses induced by the actuator displacements are aligned with the polarization. In the annular design, the induced stress axis is *normal* to the polarization direction.

Some early studies indicated that poled ferroelectrics are prone to non-linear deformation upon compression along the poling direction.[3] As a result, the remnant polarization is partially eliminated. Conversely, stresses applied *perpendicular* to the poling direction are believed to stabilize the polarization. The non-linear effects are attributed to domain switching, induced by the mechanical loads.[10] A more detailed study of these effects is presented in this article. An attempt is also made to rationalize the observed stress/strain curves with respect to the interplay between ferroelectric and ferroelastic domain switching.

2. EXPERIMENTAL PROCEDURES

2.1 Materials and Specimen Preparation

Ferroelectrics considered for large displacement actuator applications are of three types[11-12]: i) piezoelectrics; ii) ferroelectric relaxors; iii) antiferroelectrics. The first category has been most popular in practice and therefore is emphasized in the preliminary study. Poled piezoelectrics, PZTs, were obtained from a commercial

Submitted to the MRS Spring meeting Proceedings.

source‡: PZT-A (Zr/Ti = 52/48) with hard dopants (Ba and Fe) and PZT-B (Zr/Ti = 53/47) with soft dopants (Nb). The relaxor material and the antiferroelectrics were examined in a companion study.[13]

Short compression cuboids with nominal dimensions 6 x 8 x 12 mm were cut from bulk ferroelectrics and all non-electroded faces ground, using a resin-bond diamond wheel. In some cases, one of the side faces was polished to facilitate observations during testing. The electrodes were connected to a large capacitor for polarization measurement.

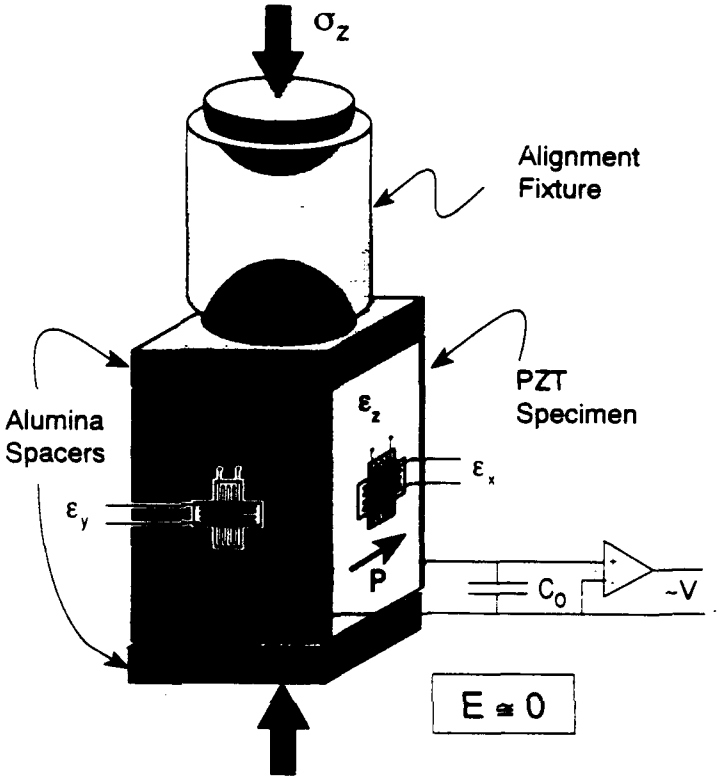

Fig.1. Compression loading fixture with associated measurement circuits.

2.2 Testing and Measurements

Uniaxial compression testing of brittle materials is notoriously difficult, given the requirement that the load be applied at the geometric center to eliminate bending. Nearly perfect alignment is essential in order to characterize the non-linear deformation. Consequently, a special loading fixture (Fig. 1) has been designed to facilitate the alignment procedure and also to provide a means for recording the electric displacement. Two spherical cones were incorporated with two flat alumina blocks used to insulate the electrodes. Specimens were carefully emplaced at the center between the alumina blocks. The fixture was then incorporated into a servohydraulic machine for testing. Final adjustments needed to minimize bending were made through *in situ* measurement of the strain differential upon exposing the

‡ Channel Industries, Inc., Goleta, California.

specimen to loading/unloading cycles, within a very small stress range (< 5 MPa). The specimen was connected in a closed loop with a large capacitor, having capacitance five orders of magnitude larger than the specimen (Fig. 1). In this case, the voltage change across the capacitor, measured by a voltage follower, provided an indication of the charge transfer from the specimen to the capacitor.‡ Consequently, the polarization change, ΔP, could be obtained as

$$\Delta P = C_o V \tag{1}$$

where C_o is the capacitance of the shunt capacitor and V is the voltage measured across the capacitor. The convention adopted here is that *depolarization* is indicated by *positive* ΔP.

Other quantities measured simultaneously with the voltage include the load instantaneously carried by the specimen obtained from the load cell output of the testing machine. Also, bi-directional strain gauges were emplaced on two opposing side faces to measure the deformation along both the loading and transverse directions, as well as monitor possible bending caused by misalignment. The strain component along the *loading* direction is designated, ε_{zz}. For specimens tested with the loading perpendicular to the polar axis, the strain along that axis is designated, ε_{xx}, and the other normal strain, ε_{yy}. When the loading is parallel to polar axis, $\varepsilon_{xx} = \varepsilon_{yy}$. Positive quantities for *stress*, and *strain*, denote *compression*, unless otherwise indicated.

3. RESULTS

The deformation behavior found for hard and soft PZTs subject to stress applied *parallel* to the poling direction (Fig. 2) indicate that both materials are non-linear when the stress exceeds ~ 20 MPa, and exhibit similar permanent deformations (~ 0.5%) after exposure to stresses above 500 MPa. The major difference between these materials occurs upon unloading. In the *"soft" material* (PZT-B), the non-linear deformation is nonrecoverable, at stress levels as low as 30 MPa (Fig. 2a). Conversely, the *"hard" material*, (PZT-A), recovers most of the non-linear deformation, with considerable hysteresis (Fig. 2b): a phenomenon usually referred to as *anelastic* deformation. However, the capacity for *anelastic* strain is destroyed at stress > 300 MPa.

The strain measurements indicate that the volume strains ($\varepsilon_{zz} + \varepsilon_{xx} + \varepsilon_{yy}$) are essentially linear for both materials (Fig. 3). Consequently, the non-linear deformation is related *solely to the deviatoric* components of stress, σ', and strain, ε' (Fig. 4). The instantaneous Poison's ratio obtains a value characteristic of incompressible plastic flow (0.5) as the nonlinear deformation proceeds. The deviatoric stress/strain curves have a form (Fig. 5) characteristic of that found for phase transformations, consisting of i) an initial hardening regime wherein the hardening-rate *diminishes* as the stress increases, followed by ii) a regime of *accelerated* hardening, as a saturation plastic strain is approached. Consequently, the stresses σ' and plastic strain, ε'_p, can be described by a bifunctional power law expression,

---

‡ It is emphasized that the change in voltage is minimal.

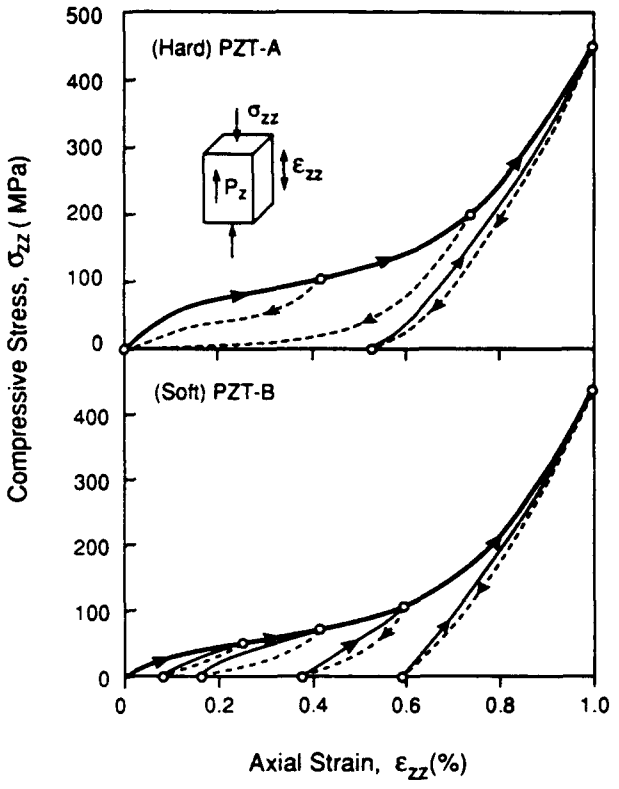

Fig. 2. Stress/strain curves from hard and soft PZTs subject to stress along polar axis.

$$\sigma'/\sigma'_o = \left(\varepsilon'_p/\varepsilon'_o\right)^a + \left(\varepsilon'_p/\varepsilon'_o\right)^b \quad (2)$$

where a and b are empirical power law coefficients ($a < 1$ and $b > 1$), σ'_o is a reference stress and ε'_o a reference strain. The magnitudes of the coefficients for the hard and soft materials are summarized in Table I.

TABLE I Constants in Deviatoric Constitutive Law (Eqn. 2)

	a	b	σ'_o (MPa)	ε'_o (%)
(Hard) PZT-A	0.54	9	100	0.62
(Soft) PZT-B	0.7	12	75	0.65

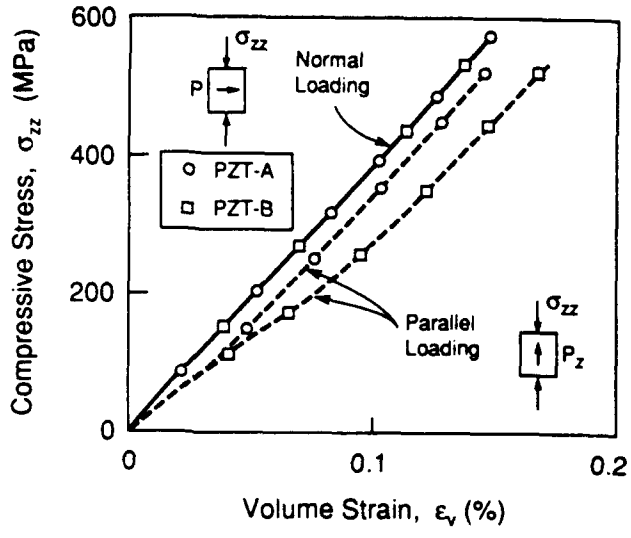

Fig. 3. Change in volume strain with axial stress for hard and soft PZT's.

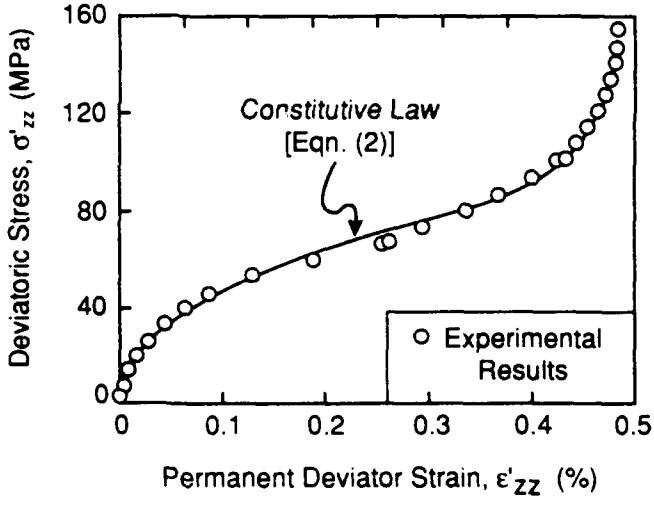

Fig. 4. The deviator plastic strain, as it relates to deviatoric stress, is solely responsible to the non-linear deformation.

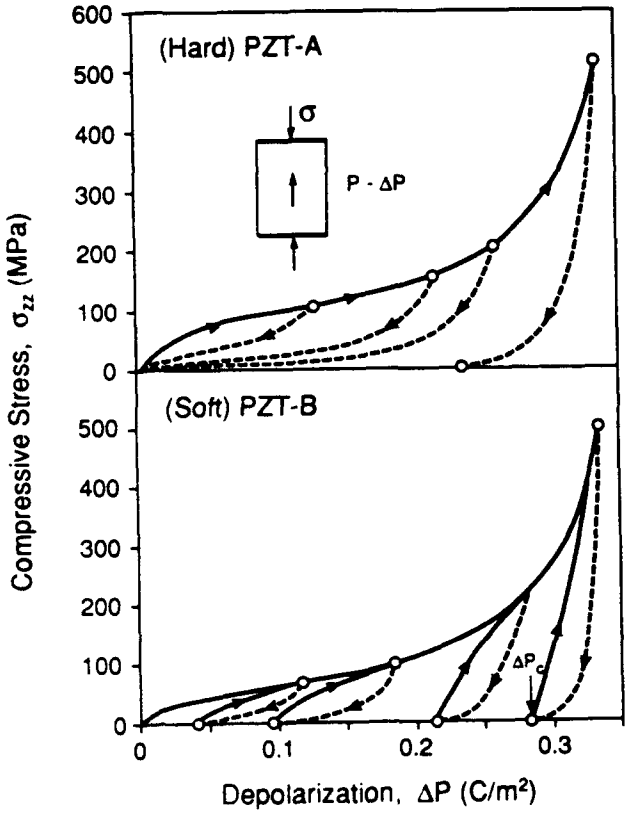

Fig. 5. Electrical depolarization, ΔP, for hard and soft PZTs as a function of the applied stress.

For the both materials, the charge on the capacitor changes during loading, expressed as a depolarization, ΔP. The depolarization curves for each material (Fig. 5) resemble the corresponding stress/strain curves (Fig. 2), suggesting that the sources of the non-linear deformation are also responsible for the polarization changes. The total depolarization measured after a stress exposure of ~ 500 MPa is ~ 80% of the remnant polarization induced upon poling.

The stress/strain curves obtained when the stress is applied *normal* to the poling direction are qualitatively the same (Fig. 6) but exhibit more limited non-linearity. For example, the permanent strain in the soft material (~ 0.3%) is about half that obtained upon loading along the poling axis. However, the transverse strains ε_{xx} and ε_{yy} (Fig. 7) have *opposing* non-linearities, as a result of the anisotropy caused by poling. The depolarization curves exhibit features (Fig. 8) dramatically different from those evident upon loading along the poling axis. Initially, the polarization *increases* as the strain increases, but when the strain exceeds ~ 0.1%, *an inversion occurs and the polarization begins to decrease with continued straining.*

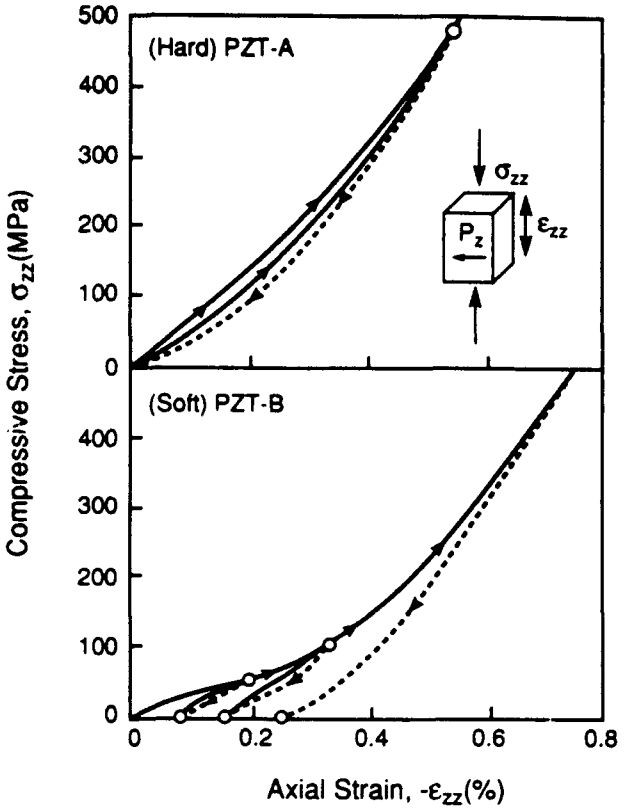

Fig. 6. Stress/strain curves for hard and soft PZTs when the stress is applied normal to the polar axis.

4. NON-LINEAR DEFORMATION

The volume strain in all specimens appears to be linear and non-hysteretic (unless microcracking occurs). Consequently, when non-linearity arises, it is only necessary to understand and model the *deviatoric deformation:* as in metal plasticity. The incremental deviatoric strain upon loading then relates to the corresponding deviatoric stress, through a constitutive law (Eqn. 2).

The mechanism responsible for the non-linear deformation in the piezoelectric materials involves 90° domain switching, having the features schematically illustrated in Fig. 9. The as-processed polycrystalline material has a nominally random set of orientations in the polarization vector, P_i. An applied electric field induces both 180° and 90° domain switching, leading to a preferred alignment of P_1 in the direction of the field. Residual stress also develops in association with 90° domain switching. Poling of PZTs is conducted with a field, E_x. Subsequent stressing may be along either z or x. For domain B (Fig. 9), oriented along z, initially $P_x = P_y = 0$ and $P_z = P_o$. This type of domain is most likely to switch during

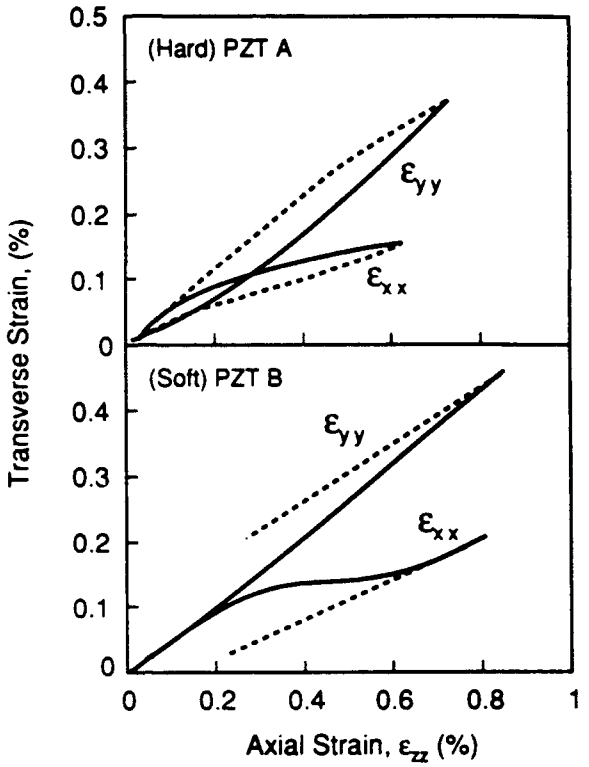

Fig. 7. Transverse strain characteristics for both PZTs as a function of applied normal stress.

poling,‡ above a critical field, to an orientation $P_y = P_z = 0$ and $P_x = P_o$. The new orientation is stable, subject to subsequent mechanical stress σ_{zz}, but depoling is possible when a σ_{xx} stress is applied. If poling did *not* cause the domain to switch (because the field is too small), switching may be activated by a subsequent σ_{zz} stress, whereupon the domain would realign along *either* P_x *or* P_y. For domain C, the situation is similar and an electric field E_x is again likely to induce $P_y \rightarrow P_x$ switching. Domain D is most illustrative of the interplay between the electric field and stress. No domain switching can occur subject to E_x, because there is no net change in P_x upon switching from P_1 to P_2: moreover, P_x, *decreases* if switching occurs from P_1 to P_3. However, upon σ_{zz} stressing, switching from P_1 to P_3 is expected when the normal stress ($\sigma_1 = \sigma_{zz}/2$) reaches a critical value. This event

‡ In some cases, 90° domain switching upon poling may be inhibited by the strain energy increase associated with the residual strain.

produces a *positive* strain in ε_{yy} but *negative* strain in ε_{xx} and ε_{zz}. A related mode of switching may occur upon σ_{xx} stressing.

The basic insight obtained from Fig. 9 allows the major phenomena found by experiment to be rationalized. For the *poled PZT materials*, tested with the mechanical loading axis coincident with the poling direction, the mechanical field causes switching in a sense *opposite* to that caused by poling resulting in systematic depoling. Once the depoling is complete, further switching does not occur. However, this mechanically depoled state must be contrasted and distinguished from the original (unpoled) state, in that the random polarization vectors in the virgin material are now in a plane normal to the depoling stress. "Complete depoling" results in the saturation behavior found at plastic strains > 0.5% (Fig. 2). Thereafter, the material behaves as an elastic body until microcracking commences prior to mechanical failure.

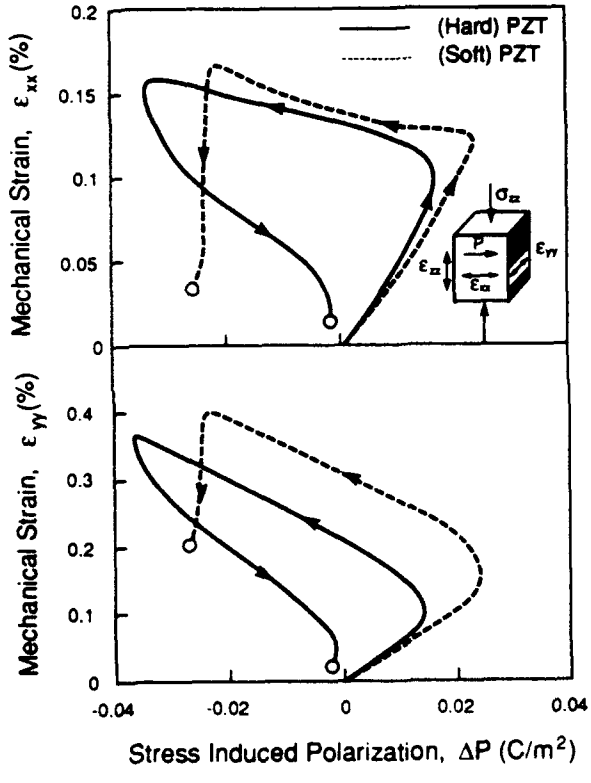

Fig. 8. Polarization changes in the polar axis caused by stress applied normal to the polar axis.

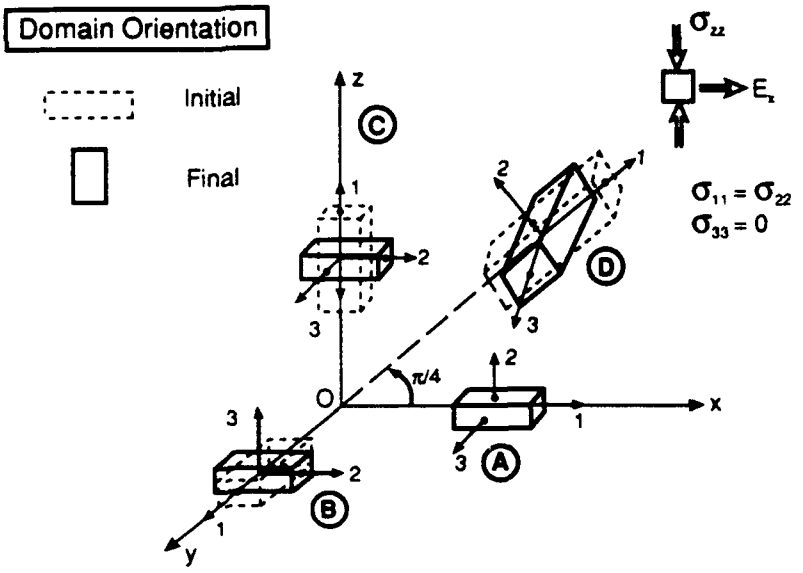

Fig. 9. Schematic of deformation by domain switching.

Loading *normal* to the poling axis (usually thought to be linear) causes a non-linear response best illustrated by orientation D in Fig. 9. Some of the 90° domains are unfavorably oriented for switching upon poling, but are in a preferred orientation for switching upon loading. The important consequence is the relationship found between the polarization change, ΔP, and the ε_{xx} strain (Fig. 8). The initial portion of these curves is the normal, linear piezoelectric effect. However, type D domain switching at larger stresses causes depolarization ($-\Delta P_x$) and an expansion along the x-axis, leading to the observed *inversion* in the polarization curve.

The parameters that characterize the non-linear deviatoric stress/strain (Eqn. 2), must depend on factors such as the domain wall mobility, the residual stresses, etc. More detailed analysis is needed to develop a general yield criterion and a flow law. For this purpose, experiments involving multiaxial stresses are necessary. Furthermore, the differences found between the "hard" and "soft" PZTs should be consistent with the yield criterion and flow law.

5. CONCLUSION

Mechanical non-linearity found in piezoelectric ceramics has been attributed to ferroelastic domain switching, with a yield criterion controlled by a deviatoric effective stress. The flow rule obeys a power law formula at small strains, similar to metal plasticity. At larger strain, accelerated hardening occurs and the inelastic strain approaches saturation. Consequently, a bifunctional power law is proposed to model the overall nonlinear response.

Strong interconnections have been established between ferroelectric and ferroelastic deformation. Electrically "hard" PZT can sustain appreciable mechanical loads without significant *permanent deformation*, whereas "soft" PZT is susceptible to permanent deformation at small stresses. This difference arises even though the "yield" stresses are similar for the two materials. Consequently, for actuator applications, hard PZT can be used at higher stress levels, without depoling.

Acknowledgments

Financial support for this work is provided by the Office of Naval Research, , under the contract No: N00014-91-J-4024.

REFERENCES

1. L.E. Cross, ONR Report, Penn. State, 1990.
2. R.E. Newnham, Q.C. Xu, S. Kumar and L.E. Cross, *Ferroelectrics*, **102**, 77–89 (1990).
3. H.H.A. Krueger, *J. of Acoustical Soc. of America*, **42[3]** 636–45 (1967).
4. H.H.A. Krueger, *J. of Acoustical Soc. of America*, **43[3]** 385–91 (1968).
5. H.H.A. Krueger and D. Berlincourt, *J. of Acoustical Soc. of America*, **33[10]** 1339–44 (1961).
6. S.R. Winzer, N. Shankar and A.P. Ritter, *J. Am. Ceram. Soc.*, **72**, 2246–57 (1990).
7. Z.G. Suo, C.-M. Kuo, D.M. Barnett and J.R. Willis, *J. Mech. Phys. Solids*, (1991).
8. J.G. Pepin and W. Boyland, *J. Am. Ceram. Soc.*, **72**, 2287–91 (1989).
9. A.F. Dyson, *Electrocomponent Sci. Technol.*, **11**, 53–64 (1983).
10. D. Berlincourt, *J. Am. Ceram. Soc.*, **706[6]** 1586–95 (1981).
11. W.Y. Pan and L.E. Cross, ONR Report, Penn. State, 1990.
12. W.Y. Pan and L.E. Cross, *Proc. of 6th IEEE Symp on Appl. of Ferroelectrics*, Lehigh Univ., June 8–11, 1986, p. 648.
13. H.C. Cao and A.G. Evans, *J. Am. Ceram. Soc.* in press.

MATERIALS

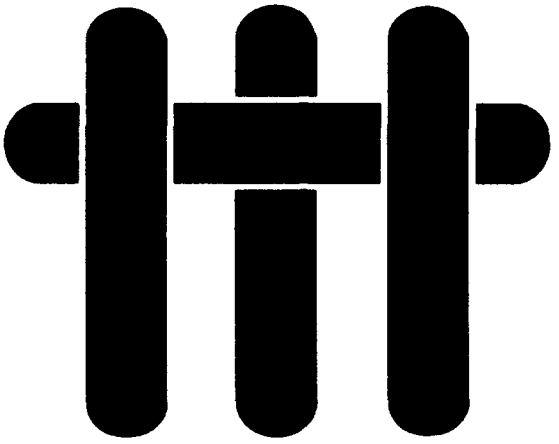

Singular Behavior Near a Crack Tip In an Elastic Electrostrictive Material

by

HengChu Cao and R. M. McMeeking
Materials Department
College of Engineering
University of California
Santa Barbara, California 93106–5050

June, 1992

To be published

KJS-2•Post-Docs•Cao•TA-Elctr Fld 92/045/06•1:42 PM•4/6/92

ABSTRACT

Singular stress and electric fields around a crack are studied for a linear elastic, electrostrictive body by using an energy conservation integral and by solving the eigein functions to the equilibrium equations. When the dielectric permeativity of the materials is very large ($>10^6 - 10^7\ \varepsilon_0$), the stress and electric field decouple and exhibit the classical square-root singularity ($r^{-1/2}$). However, when the electrostrictive deformation becomes comparible with the elastic strain at the crack tip, the asymptotic solution obtained form this study suggests that the stress and electric field exhibit different types of sigularity: with stress exhibiting square-root singularity ($r^{-1/2}$) and the electric field exhibiting a-quarter-root singularity ($r^{-1/4}$). Complete angular field distributions are obtained numerically for the asymptotic solutions. Energy release rates are also derived to correlate the intensity factors.

Prelimenary comparison of the solution with recent experiments on crack extension in an electrostrictive material is presented. These materials are intended for advanced actuator applications. Implications for mechanical reliability of multilayered ferroelectric actuators are discussed.

NOMENCLATURE

a	Crack length
D_i	Electric displacement vector (electric induction)
E_i	Electric field vector
$\tilde{E}_i(\theta)$	Angular function of strain around a crack tip
e_{ij}	Strain tensor (small strain theory)
$\tilde{e}_{ij}(\theta)$	Angular function of strain around a crack tip
G	Shear modulus
$I(\nu,m)$	Numerical function
J	J-integral (energy release rate)
$\mathcal{J}_{\mathcal{R}}$	Jacobian for planar approximation of surfaces
K	Dielectric constant
K_E	Electric intensity factor
K_{IE}	Stress intensity factor induced by electromechanical coupling
m	Electrostriction ratio; $m=S_2/S_1$
P_i	Electric polarization vector
Q_{11} ,Q_{12}	Electrostrictive constants
(r, θ)	Polar coordinate with crack tip as origin
$\mathcal{R}_1$, $\mathcal{R}_2$	Residuals at the left boundary condition for shooting method
S	Equivalent electrostrictive coefficient
S_1, S_2	Electrostrictive coefficient
u_i	Mechanical displacement
(x, y)	Cartisian coordinates
Y	Young's modulus
$y_1,...y_6$	variables for numerical solutions
δ_{ij}	Kronecker-delta

ε	Electric permitivity ($\varepsilon = K \varepsilon_o$)
ε_o	Electric permitivity of vacume ($\varepsilon_o = 0.88 \times 10^{-11}$)
Ψ	Potential energy of a body
Φ	Electric potential
σ_{ij}	Mechanical stress tensor
ν	Poisson's ratio

1. INTRODUCTION

Electrostrictive materials has been widely employed as capicitor material where application demands large capacitance but limit space is available. More recently, they are been designed for large strain actuators to be incorporated into smart materials and systems[1,2]. In these applications, they are subjected to large mechanical loading as well as the high electric driving field. Consequentely, the mechanical and electrical degradation has become an important concern [3]. McMeeking has attempted to analyze the stress distribution around a crack-like flaw in a linear elastic, electrostrictive body using an energy conservation integral approach[4,5]. The solutions are limited to less sharp flaws, such as processing porosities, where the stress concentration is less severe than those found around a sharp crack. The stress and electrical field distribution around a brittle crack have not been rinvestigated. The intent of this artical is to derive the solutions in a rigorious and self-consistent fashion, such that a plausible fracture criterion could be derived and furthermore be used to predict the mechanical failure in these materials.

2. CONSTITUTIVE EQUATIONS

We consider a linear elastic electrostrictive dielectric body. The constitutive properties can be described in two dimensional problem, by the following equation;[5]

$$e_{ij} = \frac{1}{2G}\left(\sigma_{ij} - \frac{\nu}{1+\nu}\delta_{ij}\sigma_{kk}\right) + (Q_{11} - Q_{12})P_iP_j + Q_{12}P_kP_k\delta_{ij} \qquad (1)^{\P}$$

where σ is the mechanical stress, e is the inifinitesimal strain, **P** is the local electric palorization, G is the elastic shear modulus, ν is the Poisson's ratio, Q_{11} and Q_{12} are the electrostrictive constants and δ_{ij} is the Kronecker's delta ($\delta_{ij}=1$ if i=j, and $\delta_{ij}=0$ if $i\neq j$).

¶ In all equations, summation over repeated index is implied . Index 1 and 2 refer to coordinates x and y in Cartesion coordinate and r and θ in polar coordinate.

Here the term mechanical stress referes to tractions transmitted by contact in a body. Consequently the Comlombic forces are treated as body forces (which equals to the flux of Maxwell stresses in a rigid dielectric body). If the material behaves as a linear dielectric under stress-free state, that is;

$$P_i=\varepsilon E_i \tag{2}$$

where ε is the free-body dilectric permeativity and $\varepsilon=K\varepsilon_o$ with ε_o being the dielectric permeativity of the vacume and K the dielectric constant. Equation (1) can be rearranged by making use of eqns. (2);

$$\sigma_{ij} = 2G\left(e_{ij} + \frac{\nu}{1-2\nu}\delta_{ij}e_{kk}\right) + S_1E_iE_j + S_2E_kE_k\delta_{ij} \tag{3}$$

where S_1 and S_2 are the electrostrictive coefficients, which can be expressed as;

$$\begin{aligned} S_1 &= -2G\,(Q_{11}-Q_{12})\,\varepsilon^2 \\ S_2 &= -2G\,(Q_{11}+Q_{12})\,\frac{1-\nu}{1-2\nu}\varepsilon^2 \end{aligned} \tag{4}$$

Under the action of both the mechanical strain and electric field, the electric displacement is related to E by;

$$D_i = \varepsilon_{ij}E_j = \left(\varepsilon\delta_{ij} - 2S_1e_{ij} - 2S_2e_{kk}\delta_{ij}\right)E_j \tag{5}$$

3. ENERGY DENSITY AND CONSERVATION INTEGRAL

The mechanical and electric equilibrium conditions provide the field governing equations;

$$\begin{aligned} \sigma_{ij,j} &= 0 \\ D_{i,i} &= 0 \end{aligned} \tag{6}$$

where no body force or free charges are present in the body. A potential energy expression is sought whereby the conjugate variables (E, D) and (σ, e) are related by;

$$D_i = -\frac{\partial \Psi}{\partial E_i}$$

$$\sigma_{ij} = \frac{\partial \Psi}{\partial e_{ij}} \tag{7}$$

Integration of eqns. (3) and (5) leads to;

$$\Psi = G\left[e_{ij}e_{ij} + \frac{\nu}{1-2\nu}(e_{kk})^2 + \frac{S_1}{G}\left(E_iE_j + mE_kE_k\delta_{ij}\right)e_{ij} - \frac{\varepsilon}{2G}E_kE_k\right] \tag{8}$$

McMeeking has derived an energy conservation integral for two dimensional problems;

$$J = \int_\Gamma \left[\Psi n_1 - n_j t_{jk} u_{k,1} + n_j D_j E_1\right] ds \tag{9}$$

In order that J is independent of any contour, Γ, enclosing the crack tip, it is necessary that the last two terms vanish on the crack surfaces,

$$\sigma_{xy}\frac{\partial u_x}{\partial x} + \sigma_{yy}\frac{\partial u_y}{\partial x} + D_y E_x = 0 \tag{10}$$

It is clear that both a traction-free conducting crack and a traction-free impermeable crack satisfy eqn. 10. In the former, E_x vanishes along crack surface (Φ = constant). And in the latter, $D_y = 0$ along the crack surface.

4. CRACK TIP SINGULARITIES

Evaluating J integral from eqn. 9 over a circular path of radius r from the crack tip leads to,

$$\frac{J}{r} = \int_{-\pi}^{\pi}\left\{\Psi\left[e(r,\theta)\right]cos(\theta) - T(r,\theta)\frac{\partial u}{\partial x}(r,\theta) + \left[D_r cos(\theta) + D_\theta sin(\theta)\right]E_x\right\} ds \tag{11}$$

Evidently, for J to have a finite value, the terms in {...} must exhibit a sigularity as r approaches the crack tip. A carefull scrutiny of these terms suggests that they consist of three different combination terms:

$$\frac{J}{r} \propto G e_{ij} e_{ij} + S_1 E_i E_j e_{ij} + \varepsilon E_k E_k$$

$$\equiv G\left[e_{ij} e_{ij} + \left(\frac{E_i}{\sqrt{G/S_1}}\right)\left(\frac{E_j}{\sqrt{G/S_1}}\right) e_{ij} + \left(\frac{E_k}{\sqrt{G/\varepsilon}}\right)^2 \right] \tag{12}$$

Three classes of sigularities might be exhibited by the strain and the field components. They will be discussed consecutively in the following.

Case I:

For many advanced relaxor ferroelectric ceramics (such as PMN•PT), the dielectric constant is on the order of 10^6. Consequently, it is nature to assume that the contribution to dielectric permeability from the mechanical distortion through the last two terms in eqn. 5 can be ignored compared with ε. However, the strain produced by the electric distortion is significant when compared with the mechanical strain. The electric force can be simulated by a body force. In this case, the e and E both possess conventional sqare root sigularity;

$$e_{ij} \propto K_{IE}\, r^{-1/2}\, \tilde{e}_{ij}(\theta)$$
$$E_i \propto K_E\, r^{-1/2}\, \tilde{E}_i(\theta) \tag{13}$$

where K_{IE} and K_E determines the amplitude of the field singularity, $\tilde{e}_{ij}$ and $\tilde{E}_i$ are angular distribution functions. In particular, $\tilde{e}_{ij}$ are given by the conventional Mode I elastic solutions and $\tilde{E}_i$ coincide with the angular functions in the Mode III elastic solutions. McMeeking has analyzed this situation where he provided the following solutions for a crack of length 2a in an infinte body subject to an uniform remote electric field E_y^∞ ,

$$K_{IE} = -4S\left(E_y^\infty\right)^2 \sqrt{\pi a}$$
$$K_E = E_y^\infty \sqrt{\pi a} \tag{14}$$

where $S = \dfrac{1-2\nu}{8(1-\nu)}(S_1 + 2S_2)$

It must be noted that for many electrostrictive ferroelectrics, the coeffiecient, S, is negative by defination (Eqn. 4), and therefore the stress intensity factor is positive. In contrast, for some common dielectrics such alumina and quartz, S is positive and the electric field is said to suppress the mechanical cracking.

Case II:

If the strain, e_{ij}, and the field, E_i, are both singular, the third term in the energy density function (eqn. 8), Ψ, would become negligibly small as r goes to zero. Consequently, we can make the first and the second term to exhibit the same oredr of singularity.

Let

$$e_{ij} = O\left(r^p\right)$$

and

$$E_i = O\left(r^q\right) \tag{15}$$

Substitution of eqns. 15 into eqn. 8 leads to;

$$\Psi = O\left(r^{2p}\right) + O\left(r^{2q+p}\right)$$

Therfore, we must have: p=-1/2 and q=-1/4. Consequently, the following formal solutions are sought;

$$u_r = \left(\frac{Jr}{G}\right)^{1/2} \tilde{u}_r(\theta)$$

$$u_\theta = \left(\frac{Jr}{G}\right)^{1/2} \tilde{u}_\theta(\theta)$$

$$\Phi = \left(\frac{Jr^3}{G}\right)^{1/4} \left(\frac{G}{S_1}\right)^{1/2} \tilde{\Phi}(\theta) \tag{16}$$

where $\tilde{u}_r$, $\tilde{u}_\theta$, $\tilde{\Phi}$ are angular functions to be determined by the field governing equations (eqn. 6).

5. STRESS AND FIELD AT AN IMPERMEABLE CRACK

In this section, an impermeable crack with type II singularity is considered. The solution can be expressed by eqn. 16. The strain and electric field can be derive from these expressions;

$$
\begin{aligned}
e_{rr} &= \frac{\partial u_r}{\partial r} \\
e_{\theta\theta} &= \frac{u_r}{r} + \frac{1}{r}\frac{\partial u_\theta}{\partial \theta} \\
e_{r\theta} &= \frac{1}{2}\left[\frac{\partial u_\theta}{\partial r} + \frac{1}{r}\frac{\partial u_r}{\partial \theta} - \frac{u_\theta}{r}\right] \\
E_r &= -\frac{\partial \Phi}{\partial r} \\
E_\theta &= -\frac{1}{r}\frac{\partial \Phi}{\partial \theta}
\end{aligned}
\tag{21}
$$

The stresses and electric displacements can be obtained by subsituting eqn. 21 into eqn. 3 and 5. Specifically, the following equations exist;

$$
\begin{aligned}
\sigma_{rr} &= 2G\left(e_{rr} + \frac{\nu}{1-2\nu}e_{kk}\right) + S_1 E_r E_r + S_2 E_k E_k \\
\sigma_{\theta\theta} &= 2G\left(e_{\theta\theta} + \frac{\nu}{1-2\nu}e_{kk}\right) + S_1 E_\theta E_\theta + S_2 E_k E_k \\
\sigma_{r\theta} &= 2G e_{r\theta} + S_1 E_r E_\theta
\end{aligned}
\tag{22}
$$

Substitution of eqns. 16 and 21 into eqn. 22 leads to;

$$
\begin{aligned}
\sigma_{rr} &= \left(\frac{JG}{r}\right)^{1/2}\left[\frac{1+\nu}{1-2\nu}\tilde{u}_r + \frac{2\nu}{1-2\nu}\tilde{u}_\theta' + \frac{9}{16}(1+m)\tilde{\Phi}^2 + m\tilde{\Phi}'^2\right] \\
\sigma_{\theta\theta} &= \left(\frac{JG}{r}\right)^{1/2}\left[\frac{2-\nu}{1-2\nu}\tilde{u}_r + \frac{2(1-\nu)}{1-2\nu}\tilde{u}_\theta' + \frac{9m}{16}\tilde{\Phi}^2 + (1+m)\tilde{\Phi}'^2\right] \\
\sigma_{r\theta} &= \left(\frac{JG}{r}\right)^{1/2}\left[\tilde{u}_r' - \frac{1}{2}\tilde{u}_\theta + \frac{3}{4}\tilde{\Phi}\tilde{\Phi}'\right] \\
D_r &= \left(\frac{JG}{r}\right)^{3/4}\left(\frac{S_1}{G}\right)^{1/2}\left[\frac{3}{4}(1+3m)\tilde{u}_r\tilde{\Phi} - \frac{1}{2}\tilde{\Phi}'\tilde{u}_\theta + \frac{3m}{2}\tilde{\Phi}\tilde{u}_\theta' + \tilde{u}_r'\tilde{\Phi}'\right]
\end{aligned}
$$

$$D_\theta = \left(\frac{JG}{r}\right)^{3/4}\left(\frac{S_1}{G}\right)^{1/2}\left[(2+3m)\tilde{u}_r\tilde{\Phi}' + \frac{3}{4}\tilde{u}_r'\tilde{\Phi} + 2(1+m)\tilde{u}_\theta'\tilde{\Phi}' - \frac{3}{8}\tilde{u}_\theta\tilde{\Phi}\right] \tag{23}$$

where $m=S_2/S_1$. From the equalibrium condition (eqn. 6), we have explicitely;

$$\begin{aligned}
&\frac{\partial\sigma_{rr}}{\partial r} + \frac{\sigma_{rr}-\sigma_{\theta\theta}}{r} + \frac{1}{r}\frac{\partial\sigma_{r\theta}}{\partial\theta} = 0\\
&\frac{\partial\sigma_{r\theta}}{\partial r} + \frac{2\sigma_{r\theta}}{r} + \frac{1}{r}\frac{\partial\sigma_{\theta\theta}}{\partial\theta} = 0\\
&\frac{\partial D_r}{\partial r} + \frac{D_r}{r} + \frac{1}{r}\frac{\partial D_\theta}{\partial\theta} = 0
\end{aligned} \tag{24}$$

Finally, the governing equations for the angular functions are obtained, by substituting eqn 23 into eqn 24, as;

$$\tilde{u}_r'' - \frac{3}{2}\frac{1-\nu}{1-2\nu}\tilde{u}_r - \frac{5-8\nu}{2(1-2\nu)}\tilde{u}_\theta' + \frac{9(1-m)}{32}\tilde{\Phi}^2 - \frac{1+2m}{4}\tilde{\Phi}'^2 + \frac{3}{4}\tilde{\Phi}\tilde{\Phi}'' = 0$$

$$\tilde{u}_\theta'' - \frac{3}{8}\frac{1-2\nu}{1-\nu}\tilde{u}_\theta + \frac{7-8\nu}{4(1-\nu)}\tilde{u}_r' + \frac{9(1+m)(1-2\nu)}{16(1-\nu)}\tilde{\Phi}\tilde{\Phi}' + \frac{(1+m)(1-2\nu)}{1-\nu}\tilde{\Phi}'\tilde{\Phi}'' = 0$$

$$\begin{aligned}
&16\tilde{\Phi}''\left[(2+3m)\tilde{u}_r + 2(1+m)\tilde{u}_\theta'\right] + 8\tilde{\Phi}'\left[4(1+m)\tilde{u}_\theta'' - \tilde{u}_\theta + 6(1+m)\tilde{u}_r'\right]\\
&\quad + \tilde{\Phi}\left[12\tilde{u}_r'' + 3(1+3m)\tilde{u}_r - 6(1-m)\tilde{u}_\theta'\right] = 0
\end{aligned} \tag{25}$$

To facilitate the numerical scheme, eqn. 25 can be rearranged into a matrix form;

$$\begin{bmatrix} 1 & 0 & \frac{3}{4}\tilde{\Phi} \\ 0 & 1 & \frac{(1+m)(1-2\nu)}{1-\nu}\tilde{\Phi}' \\ 12\tilde{\Phi} & 32(1+m)\tilde{\Phi}' & 16\left[(2+3m)\tilde{u}_r + 2(1+m)\tilde{u}_\theta'\right] \end{bmatrix} \begin{bmatrix} \tilde{u}_r'' \\ \tilde{u}_\theta'' \\ \tilde{\Phi}'' \end{bmatrix} =$$

$$= \begin{bmatrix} \frac{3}{2}\frac{1-\nu}{1-2\nu}\tilde{u}_r + \frac{5-8\nu}{2(1-2\nu)}\tilde{u}_\theta' - \frac{9(1-m)}{32}\tilde{\Phi}^2 + \frac{1+2m}{4}\tilde{\Phi}'^2 \\ \frac{3}{8}\frac{1-2\nu}{1-\nu}\tilde{u}_\theta - \frac{7-8\nu}{4(1-\nu)}\tilde{u}_r' - \frac{9(1+m)(1-2\nu)}{16(1-\nu)}\tilde{\Phi}\tilde{\Phi}' \\ 8\tilde{\Phi}'\left[\tilde{u}_\theta - 6(1+m)\tilde{u}_r'\right] - \tilde{\Phi}\left[3(1+3m)\tilde{u}_r - 6(1-m)\tilde{u}_\theta'\right] \end{bmatrix} \tag{25a}$$

Now consider the boundary conditions. At $\theta=0$, symmetry condition requires;

a. $\sigma_{r\theta} = 0$

b. $\dfrac{\partial \sigma_{\theta\theta}}{\partial \theta} = 0$

c. $\dfrac{\partial \sigma_{rr}}{\partial \theta} = 0$

and

d. $D_r = 0$

e. $\dfrac{\partial D_\theta}{\partial \theta} = 0$ (26)

These conditions can be satisfied, through symmetry argument, by requiring; at $\theta = 0$

$$\tilde{u}_\theta = 0$$
$$\tilde{u}_r' = 0$$
$$\tilde{\Phi} = 0 \qquad (27)$$

In addition, for a traction-free, impermeable crack, we must have on the crack surface (at $\theta = \pi$);

a. $\sigma_{\theta\theta} = 0$

b. $\sigma_{r\theta} = 0$

and

c. $D_\theta = 0$ (28)

The assumed forms of the solution (eqn. 16) warrante path-independence of the J-integral, validating eqn. 10 for all solutions. Consequently, only two of the eqns. 28 need to be enfoced. We choose (a) and (b), i.e. at $\theta = \pi$:

$$\tilde{u}_r' - \frac{1}{2}\tilde{u}_\theta + \frac{3}{4}\tilde{\Phi}\tilde{\Phi}' = 0$$
$$\frac{2-\nu}{1-2\nu}\tilde{u}_r + \frac{2(1-\nu)}{1-2\nu}\tilde{u}_\theta' + \frac{9m}{16}\tilde{\Phi}^2 + (1+m)\tilde{\Phi}'^2 = 0 \qquad (29)$$

Additionally, because the equations are homogeneous, a normalization is introduced such that at $\theta = 0$;

$$\tilde{u}_\theta' = -1 \qquad (30)$$

Eqnuations (27), (29) and (30) provide the complete set of boundary conditions.

6. NUMERICAL SOLUTIONS

Numerical solution to eqn. (25) with bondary conditions (eqns. 28, 31 and 32) is performed by means of a secant method for solving nonlinear systems of equations. Regard the problem as an initial value formulation subject to initial condition at $\theta = 0$,

$$\begin{aligned} \tilde{u}_r &= w_1^{(i)} \\ \tilde{\Phi}' &= w_2^{(i)} \end{aligned} \tag{31}$$

where $w_1^{(i)}$ and $w_2^{(i)}$ are two initial guesses. Deviation from the BC eqn. 30 is measured by the two remainders defined through;

$$\begin{aligned} R_1^{(i)} &= \tilde{u}_r' - \frac{1}{2}\tilde{u}_\theta + \frac{3}{4}\tilde{\Phi}\tilde{\Phi}'\Big|_{\theta=\pi} \\ R_2^{(i)} &= \frac{2-\nu}{1-2\nu}\tilde{u}_r + \frac{2(1-\nu)}{1-2\nu}\tilde{u}_\theta' + \frac{9m}{16}\tilde{\Phi}^2 + (1+m)\tilde{\Phi}'^2\Big|_{\theta=\pi} \end{aligned} \tag{32}$$

For numerical implementations, the following symbles have also been used;

$$\begin{bmatrix} y_1 \\ y_2 \\ y_3 \\ y_4 \\ y_5 \\ y_6 \end{bmatrix} = \begin{bmatrix} \tilde{u}_r \\ \tilde{u}_\theta \\ \tilde{\Phi} \\ \tilde{u}_r' \\ \tilde{u}_\theta' \\ \tilde{\Phi}' \end{bmatrix} \tag{33}$$

By means of a shooting scheme, the corresponding initial conditions are;

$$\begin{bmatrix} y_1 \\ y_2 \\ y_3 \\ y_4 \\ y_5 \\ y_6 \end{bmatrix}_{\theta=0} = \begin{bmatrix} 0.73275 \\ 0 \\ 0 \\ 0 \\ -1 \\ 0.92785 \end{bmatrix} \tag{34}$$

It is noted that the convergent solution renders the system of equations (25) singular. Consequently, a Taylor series expamsion form was impletemented to obtain the correct solution. The graphical representation of the results are displayed in Fig. 2.

With the angular distribution functions displayed in Fig. 2, the J-integral cab be explicitely evaluated, leading to;

$$J = K^2 + \ldots \tag{35}$$

It is further noted that the conventional crack tip elastic stress solution is obtained by using the following conditions;

$$\begin{bmatrix} y_1 \\ y_2 \\ y_3 \\ y_4 \\ y_5 \\ y_6 \end{bmatrix}_{\theta=0} = \begin{bmatrix} 2 \\ 0 \\ 0 \\ 0 \\ -1 \\ 0 \end{bmatrix} \tag{36}$$

8 IMPLICATION AND CONCLUDING REMARKS

Crack tip field solutions have been obtained for an impermeable crack in a linear elastic electrostrictive ferroelectric ceramic body subject to electric boundary conditions at remote locations. In the asymptotic form as the crack tip is approached, the stresses exhibit conventional sqare-root singularity ($\propto r^{-1/2}$) while the electric fields exhibit one-quarter-root singularity ($\propto r^{-1/4}$). Energy release rate in the conventional sense has also been derived and related to the stress and field intensity factors. It is suggested that the failure can occur due to filed induced stress intensifications.

Preliminary experiments have been conducted using a relaxor ferroelectric ceramic body. The observations indicated that the crack had indeed propagated under the imposed electric field alone. Using a narrow beam specimen, it is estimated that the field concentration factor at failure approaches _____. In comparison, when a specimen was subjected to mechanical loading, the fracture toughness measured at $K_{IC} \approx 0.9$ MPa $\sqrt{m}$.

Table I **Material Properties for .9PMN•.1PT**

Young's modulus, Y (GPa)	125
Shear Modulus, G (GPa)	46
Poisson's ratio, ν	0.35
Dielectric constant, K	5.25×10^4
Electrostrictive constants,	
Q_{11} (m^4/C^2)	0.0137
Q_{12} (m^4/C^2)	-0.00514
Electrostrictive coefficients,	
S_1 (m^4/C^2)	-3.7×10^{-3}
S_2 (m^4 / C^2,	-1.7×10^{-3}
S (.r , C^2)	-4.5310^{-5}
Fracture toughness, J_{IC} (J/m^2)	8

References

1. W.Y. Pan and L.E. Cross, "Piezoelectric and Electrostrictive Materials for Transducer Applications," ONR Report, Penn. State, 1990.

2. S.R. Winzer, N. Shankar and A.P. Ritter, "Designing Cofired Multilayered Electrostrictive Actuators for Reliability," *J. Am. Ceram. Soc.*, **73**, 2246–57 (1990).

3. J.G. Pepin and W. Boyland, "Electrode-Based Causes of Delaminations in Multilayer Ceramic Capacitors," *J. Am. Ceram. Soc.*, **72**, 2287–91 (1989).

4. R. M. McMeeking, "A J-Integral For the Analysis of Electrically Induced Mechanical Stress at Cracks In Elastic Dielectrics", Int. J. Engng. Sci. 28[7] pp 605-613, (1990).

5. R. M. McMeeking "Electrostrictive Stresses Near Crack-Like Flaws", J. Appl. Math. Phys. (ZAMP), 40, pp615-627, (1989)

6. Z.G. Suo, C.-M. Kuo, D.M. Barnett and J.R. Willia, "Fracture Mechanics for Piezoelectric Ceramics" *J. Mech. Phys. Solids*, (1991).

7.

Figure Captions

Fig. 1 Crack geometry in a dielectric material

Fig. 2 Angular distribution functions for a crack in a linear elastic electrostrictive material.

Fig. 3 Crack extension observed in PMN•PT under alternate electric field(~3MV/m).